MASTER

Investigation of the mechanisms of bacterial inactivation induced by a cold atmospheric pressure plasma jet for burn wound treatment

van Gils, Koen

Award date:
2012

Eindhoven University of Technology
Department of Applied Physics
Elementary Processes in Gas Discharges (EPG)

Master's Thesis

Investigation of the mechanisms of bacterial inactivation induced by a cold atmospheric pressure plasma jet for burn wound treatment

C.A.J. van Gils

August 2012 EPG 12-13

Supervisors:
Dipl.-Phys. S. Hofmann
dr. B. Boekema - Association of Dutch Burn Centres
dr. P.J. Bruggeman

Abstract

Biological applications of cold atmospheric pressure plasma sources such as disinfection of human tissue and medical equipment and more recently wound healing have gained increasing interest in recent years. The beneficial effects of plasma treatment are commonly thought to originate from symbiotic effects of the so-called 'plasma cocktail', consisting of plasma emitted electrons and ions, radicals, (V)UV, heat and electromagnetic fields.

This work focuses on the possibilities of cold atmospheric pressure plasma jet treatments of burn wounds, as bacterial infections occur frequently in burn wound patients. Atmospheric pressure plasmas may provide additional means to reduce the bacterial concentration on a burn wound while minimizing the damage inflicted on surrounding tissue. The research presented here is performed in collaboration with the Association of Dutch Burn Centres.

The biological part of this work focuses on the in vitro treatment of the bacterium Pseudomonas aeruginosa, but preliminary treatments of Staphylococcus aureus and human cells (keratinocytes and fibroblasts) are also presented. Keratinocytes and fibroblasts need to be submerged in liquid to avoid dehydration. Because of this, for the treatments of both bacteria and human cells to be comparable, the treatments of bacteria are performed in a liquid medium rather than on a surface. The atmospheric pressure plasma jet used for the biological treatments is characterized by measurements of power dissipation, gas temperature, absolute UV-flux as well as mass spectrometry measurements of emitted ions. The effects of plasma treatment of water are studied by performing liquid ion chromatography and hydrogen peroxide concentration measurements on treated samples. Additionally, an estimation is made of the fluid chemistry induced by the radical flux on the surface of the liquid by solution kinetics calculations.

The effects of each of the possible active components in the 'plasma cocktail' is analyzed and compared to similar experiments reported in literature. In the experiments presented in this work the effect of the plasma can be solely ascribed to plasma induced fluid chemistry, leading to the production of stable and transient chemical species. It is shown that HNO_2, $ONOO^-$ and H_2O_2 are present in significant quantities which could explain (with inclusion of symbiotic effects) the bacterial inactivation observed in this work. The reasons for neglecting the influences of the other components of the 'plasma cocktail' are extensively discussed and motivated by a large parameter study of both plasma and treatment conditions.

Table of Contents

Chapter 1

Introduction

Bacterial infections are a common problem in burn wound patients. As patients with severe burn wounds have a compromised immune system, they are much more susceptible to infections of opportunistic bacteria such as Pseudomonas aeruginosa and Staphylococcus aureus. These kind of infections can spread easily via for example contact with medical personnel or improperly designed sinks [1]. Avoiding infections in burn wounds leads to lower morbidity and mortality.

According to McManus et al. [2] Pseudomonas infections occurred in approximately 7% of all burn patients in his clinic. The mortality rate after infection was approximately 50%. The infection rate and mortality are both highly dependent on the total area of the burn wound however. These results clearly show the need to be able to prevent or effectively treat Pseudomonas infections.

In recent years the bactericidal effects of atmospheric pressure plasmas have gained increasing attention[3]. Possible applications of the bactericidal effects of these plasmas include dermatology[4], disinfection of heat sensitive medical devices such as endoscopes[5] and dentistry[6, 7]. Other applications include for example stimulated blood coagulation[8].

This work focuses on the characterization of an atmospheric pressure plasma jet and its efficacy in treatments of bacteria and cells applicable to burn wounds. The plasma source is characterized using measurements of power dissipation, gas temperature, absolute UV-flux as well as mass spectrometry measurements of emitted ions. Mainly treatments of the bacterium Pseudomonas aeruginosa are shown, but also preliminary treatments of Staphylococcus aureus and human cells (keratinocytes and fibroblasts) are discussed. An analysis is made of the various active plasma components and their contribution to the observed biological effects is quantified.

The biological experiments presented in this work have been performed in collaboration with the Association of Dutch Burn Centres, in their laboratory in Beverwijk. This cooperation allows a combination of expertise in plasma physics as well as microbiology. Providing a link between the biological experiments and the diagnostics is essential to acquire insight in the mechanisms behind the plasma induced bactericidal effects.

1.1 Plasma disinfection

In previous research, various reasons for the bactericidal effect of atmospheric pressure plasmas have been postulated. As the plasma is in contact with the atmosphere, interactions between the two can give rise to production of for example O, O_3, NO, NO_2 and OH. The (V)UV radiation emitted by the plasma is also stated to be a possible reason for bactericidal effectiveness, as well as interactions with ions generated by the plasma. In literature the combination of heat, electric fields, ions, radicals and UV generated by the plasma is frequently dubbed the 'plasma cocktail'[9, 10, 11]. By combining plasma diagnostics and treatment

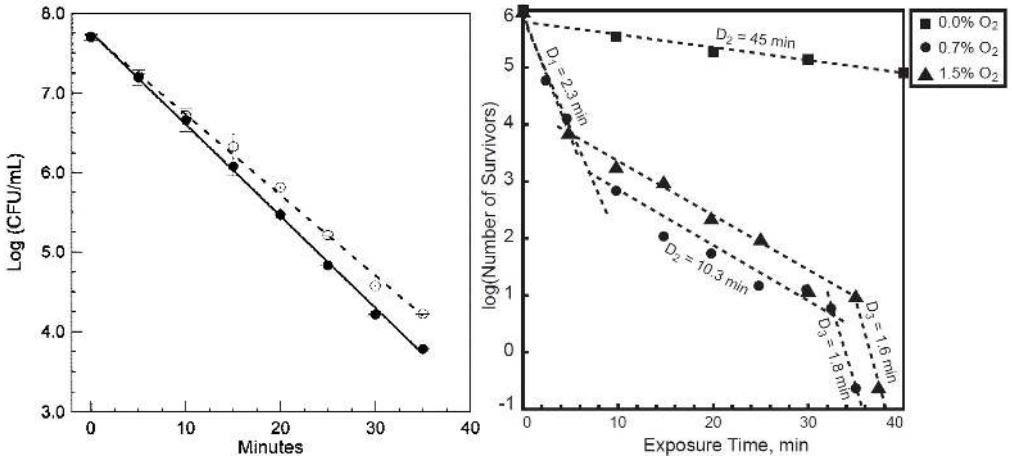

(a) Heat treatment, 92.3°C[12] (b) 5 Torr N_2/O_2 discharge afterglow[13]

Figure 1.1: Inactivation kinetics for B. subtilis spores exposed to a N_2/O_2 discharge afterglow compared to heating at 92.3°C.

of cells and bacteria an assessment is made of the influence of each of these components in achieving the observed bactericidal effects.

In literature these antimicrobial properties have in some cases incorrectly been called 'plasma sterilization'. The reason for this is that plasma inactivation kinetics are different than for example in an autoclave[1]. Ideally, a sterilization process shows an exponential decrease of the number (CFU[2]) or number density (CFU/ml) of viable micro-organisms as a function of treatment intensity. Treatment intensity can for example signify a treatment time, power, temperature or a concentration (when using chemicals). When plotted on a log scale, this leads to a linear dependency with one slope. Plasma inactivation kinetics generally show more than one slope, an example of which is seen in figure 1.1 where heating inactivation kinetics for Bacillus subtilis are compared to plasma treatment[12, 13]. Heating results in one slope, whereas the plasma treatment shows three different slopes which indicates multiple inactivation processes. This means that while in the case of for example an autoclave the number density can be extrapolated to a suitable value, this does not hold for plasma treatments[14].

Being able to extrapolate provides the possibility to define a sterility assurance level (SAL), which quantifies the occurrence of viable microorganisms on objects. The line in figure 1.1a can be extrapolated to a value of for example 10^{-6}, basically denoting the chance of finding a viable bacterium in one ml of solution. The sterility assurance level in this case is 10^{-6}. Similar plots can be made in which the density of bacteria on objects rather than per milliliter is on the vertical axis. In this case a SAL of 10^{-6} means that approximately one out of every 10^6 treated objects is expected to contain a viable microorganism. A SAL of 10^{-6} is usually recommended for products in contact with breached human skin, whereas 10^{-4} is recommended for products that are not or for heat sensitive products[15].

While plasma sterilization is impossible to guarantee, plasmas are still promising in reducing the number of pathogens. A more suitable classification of plasma treatments would be that it acts like an antiseptic when used on humans or as a disinfectant when used on non-living objects. Both terms imply the same effect, namely a clear reduction of the amount of viable microorganisms. In treatment of human tissue the lack of sterilization properties is not an issue, as reducing the amount of pathogens significantly may already

[1]An instrument used to sterilize equipment by using high pressure saturated steam at 121°C.

[2]Colony-forming unit. A viable bacterium (i.e. one that is able to replicate) is called a colony forming unit.

(a) Before treatment (b) After 7 treatments (c) After 11 treatments

Figure 1.2: Venous ulcer on a 61-year-old patient for a daily treatment of two minutes using the *MicroPlaSter Alpha* argon atmospheric pressure plasma source[4].

Figure 1.3: Treatment of an eyelid phlegmon using a 3mm diameter air plasma plume for 5s per treatment. Before (left) and after 6 treatment sessions (right)[16].

provide enough relief for the body's immune system to take over and suppress any residual pathogens.

Figure 1.2 shows the results of treatment of a venous ulcer on the leg of a 61-year-old patient using an argon atmospheric pressure plasma. Before treatment the wound was completely open and Klebsiella oxytoca and Enterobacter cloacae were found. After 7 treatment sessions the wound already seemed to react to treatment and after 11 sessions a significant change was observed; the wound was closing and the wound swabs were clean[4].

Another example of atmospheric pressure plasmas in health care is shown in figure 1.3. The left picture shows a case of an eyelid phlegmon (expansion of a local infection in the eye or eyelid) which is treated six times with an atmospheric air plasma for 5 seconds per treatment. After treatments the eyelids were free of pathogens and six days after the last treatment the patient was discharged[16].

Atmospheric pressure plasmas do not only provide bactericidal effects, they can also stimulate cell growth and aid in blood coagulation. An example of the latter effect is shown in figure 1.4 where a cut human spleen is treated with a dielectric barrier discharge for 30 seconds. The tissue temperature remains approximately at room temperature, even after extended treatment times. An untreated cut is shown for comparison. In the treated cut the bleeding stopped and a moist wound remains[8].

1.2 Motivation of this work

Atmospheric pressure plasma sources used in biological treatments are not well characterized. The flux of for example radicals, ions and UV are not always known. Possible induced chemistry is hard to measure due to its transient nature and in some cases the plasma dissipated power is not even measured. A more fundamental understanding of the plasma induced effects and its contributing components is necessary to determine possible beneficial or perhaps harmful effects.

This work focuses on providing a systematic analysis of the various components of the plasma treatment by combining measurements, calculations and treatments. By doing this a more complete picture of the underlying mechanisms is achieved.

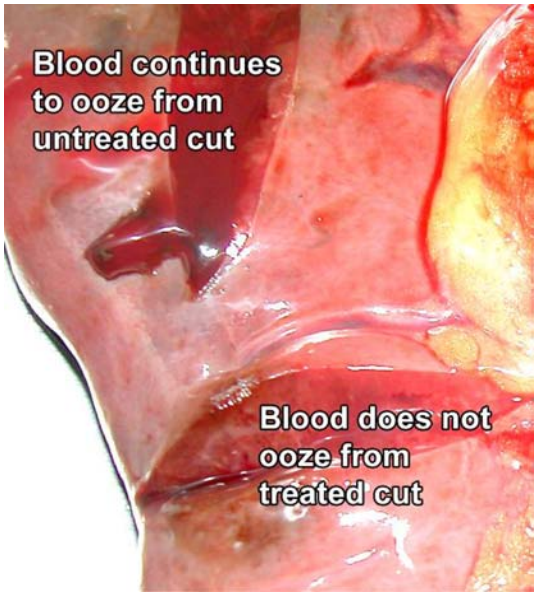

Figure 1.4: Coagulation of blood oozing from a cut in a human spleen after 30s of DBD treatment[8].

1.3 Outline of this thesis

Firstly the various atmospheric pressure plasma sources used in plasma treatments in literature are discussed in chapter 2, after which basic biology applicable to burn wounds is reviewed in chapter 3. The experimental setup including the plasma source itself and the various diagnostics are introduced in chapter 4, and the acquired measurement results are presented in chapter 5. After this the results of treatments of two types of bacteria and two types of human cells are shown in chapter 6. Finally by using the measurements and treatment results combined with calculations and a literature review, the possible mechanisms of atmospheric pressure plasma disinfection are discussed in chapter 7.

Chapter 2

Cold atmospheric pressure plasma sources

This chapter will first briefly review some of the physics related to atmospheric pressure plasma sources, after which various different atmospheric pressure plasma sources currently being used in the field of plasma medicine will be introduced. Firstly the dielectric barrier discharge and plasma needle will be discussed, followed by the plasma jet. While the plasma sources are different, the strongly non-equilibrium character is shared by all. The result is a low gas temperature (close to room temperature) but high reactivity which allows for treatment of heat sensitive materials such as for example plastics or human tissue.

2.1 Radio frequency discharges

For a DC discharge, the voltage required to achieve breakdown between two plate electrodes is defined by [17]

$$V_b = \frac{Bpd}{\ln Apd - \ln\left[\ln\left(1 + 1/\gamma_{se}\right)\right]}, \tag{2.1}$$

where p is the pressure in Torr, d is the electrode spacing in cm and γ_{se} is the material dependent secondary electron emission coefficient. A and B are both experimentally determined constants. Using equation 2.1, so-called Paschen curves can be plotted which show the breakdown voltage as a function of pd. However, for RF discharges there is no simple expression for the breakdown voltage as the mechanisms are more complex. There is however experimental data of these breakdown voltages, allowing a comparison of DC and RF breakdown processes.

Figure 2.1 shows an example of Paschen curves of argon and helium for DC and RF (13.56 MHz) discharges. At for example 1 atmosphere (760 Torr) and an electrode spacing of 1mm, there is approximately an order of magnitude difference in the breakdown voltage. Furthermore, Park et al.[18] show that at frequencies higher than approximately 10 MHz, the breakdown voltage does not significantly decrease anymore at atmospheric pressure. This shows why RF is preferred over DC at atmospheric pressure; to obtain breakdown using RF, a much lower voltage is required. This in turn leads to lower discharge powers and therefore a lower gas temperature. These characteristics of RF plasmas are especially important for treatment of human tissue, where lower voltages and higher frequencies are preferred. This is because the touch perception and pain threshold for electric currents decreases with increasing frequency. For example at 50 Hz the minimum current for touch perception is 0.2 to 0.4 mA, whereas at 1 MHz it is 25 to 40 mA[19]. A disadvantage of RF compared to DC discharges is the need for impedance matching circuits in the latter case.

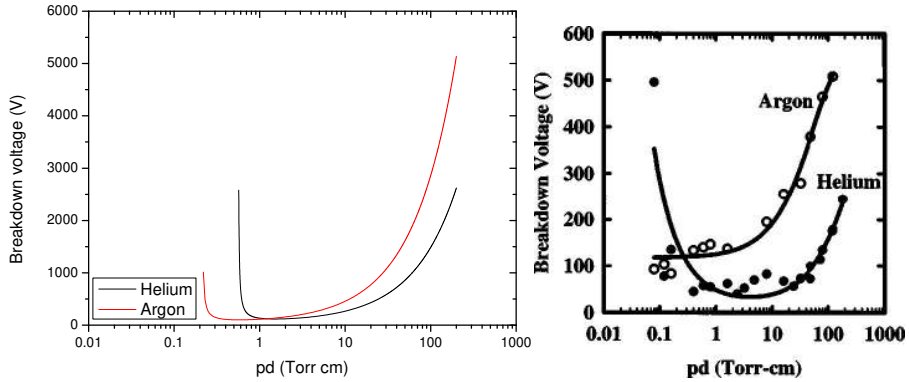

(a) DC, data from [17]

(b) RF (13.56MHz)[20]

Figure 2.1: Paschen curves of helium and argon for DC and RF discharges.

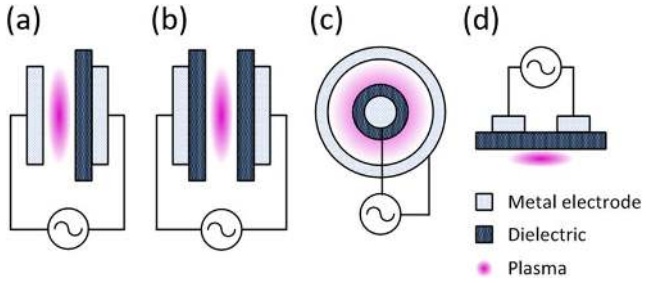

Figure 2.2: Various DBD configurations such as (a),(b) parallel plate (c) coaxial and (d) coplanar.[21]

2.2 Dielectric barrier discharge

A dielectric barrier discharge (DBD) typically consists of two electrodes of which at least one is covered with a dielectric layer. One of the electrodes is powered while the other is grounded. The grounded electrode can for example also be the sample to be treated. Usually the distance between the two electrodes is several millimeters, the current is of the order of milliamperes and the ionization degree is low. A DBD can have various configurations, some of which are shown in figure 2.2. An important property of DBDs is that they can only be operated using AC or pulsed DC because of the dielectric layer, which limits the current.

A DBD can be operated in a filamentary mode and a diffuse mode, depending on for example the materials used, the distance between the electrodes, the voltage and the gas composition. When forming filaments, there is a self limiting effect of the current due to charge accumulation on the dielectric layer. This results in short filament lifetimes. While a diffuse discharge is convenient for homogeneous treatment of large surfaces, in practice it is hard to achieve a purely diffuse mode, especially for larger surfaces.

2.3 Plasma needle

An alternative plasma source is the plasma needle, developed by Stoffels et al.[22]. It consists of a metal needle electrode which is driven by an RF amplifier in combination with a matching circuit. Helium is used as a carrier gas and is supplied through a dielectric tube surrounding the needle. An example of a plasma generated with this plasma needle is shown in figure 2.3. The photographs show a clear difference in morphology between

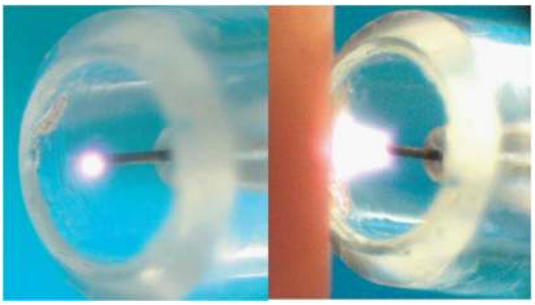

Figure 2.3: Plasma needle as used by Stoffels et al.[22] in non-touching condition (left) and touching dry skin (right).

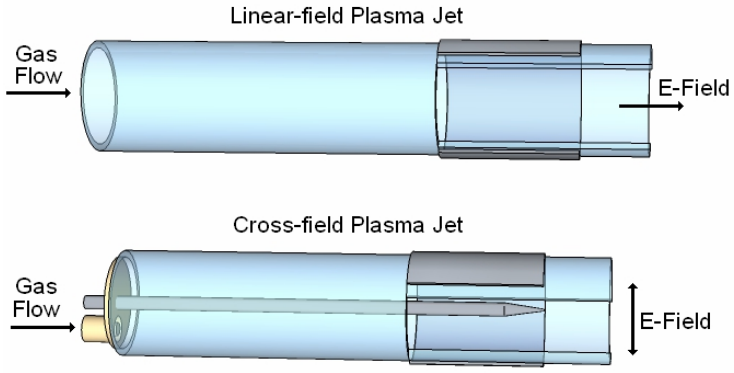

Figure 2.4: Schematic representation of linear and cross-field plasma jets.[24]

touching (right) and not touching (left) a surface. In this case the surface is dry skin, so it has a limited conductivity.

2.4 Plasma jet

Plasma jets generally have a channel through which a carrier gas (usually argon or helium) is blown. One or multiple electrodes can be incorporated and the electrodes can be driven by pulsed high voltage DC, radio frequency (RF) and microwave (MW) signals, depending on the configuration. The electrode can for example be a needle or one or multiple rings around the cylindrical channel.

An important difference between a plasma jet with a needle electrode and a plasma needle is that as the channel has a smaller diameter the flow in a plasma jet forces the plasma out and away from the needle, creating an extended plasma plume.

Two fundamentally different electric field configurations exist in plasma jets; so-called linear and cross-field jets. In linear plasma jets, the electric field is parallel to the gas flow direction, whereas in cross-field jets the electric field is perpendicular. A schematic representation of the different configurations is shown in figure 2.4. Linear plasma jets are found to facilitate electron and ion transport and production downstream, thereby increasing active plasma chemistry in the far downstream region while the cross-field jet typically causes a recombining afterglow plasma rich of reactive species[23].

In this work we will investigate both the cross-field and linear field jet. The source is described in detail in section 4.1.

Chapter 3

Biology of burn wounds

This chapter explains the composition of the human skin and shows the basic components and mechanisms of wound healing and more specifically burn wound healing. The efficiency of conventional treatments of burn wound infections are reviewed and the two most dominant bacteria in burn wounds, Pseudomonas aeruginosa and Staphylococcus aureus are introduced. Finally the properties of important cells in wound healing, namely keratinocytes and fibroblasts are discussed. This chapter motivates why we investigated the effects of plasma treatment on the above mentioned human cells and bacteria and some previous related plasma treatment results are reviewed.

3.1 Human skin

The human skin is built up of three layers, the epidermis, dermis and subcutis. A cross section of the skin is shown in figure 3.1. The epidermis is the outermost layer of the skin which itself consists of several layers. It has a thickness of about 0.05 to 0.1 mm and consists mainly of keratinocytes. The formation of these cells starts in the basal layer and progresses outward through the spinous and granular layer over a course of about 30 days. As a result the human skin is constantly being 'renewed'. During this process the keratinocytes flatten and become cornified in the stratum corneum. At this point the keratinocytes are called corneocytes. They have lost their nuclei and cytoplasmic organelles (membrane enclosed parts of the cell with specific functions) and are highly insoluble.

The dermal-epidermal junction provides a connection between the dermis and the epidermis and contributes to cell migration. The dermis is approximately 0.5 to 5 mm thick and consists mostly of collagen and water. It contains eccrine (sweat) glands as well as hair follicles, sebaceous glands (which secrete oily matter), arrector pili (causing hairs to stand on end, 'goosebumps') and nerves (not shown). It is also very well supplied with blood, which does not cross the dermal-epidermal junction.

The subcutis is the lowermost layer of the skin. It is made up of among others fat, hair follicle roots, fibroblasts and macrophages.

3.2 General wound healing

Normally, wound healing consists of three phases, which partly overlap. The phases are inflammation, re-epithelialization and matrix remodelling. This section will briefly explain these different phases and their contribution to the healing process. An overview of various cells present during the different stages of wound healing are shown in figure 3.2.

When skin tissue is wounded, platelets degranulate[1], the blood coagulates and a fibrin

[1]Degranulation is the process of releasing cytotoxins from granules, small secretory particles in cells.

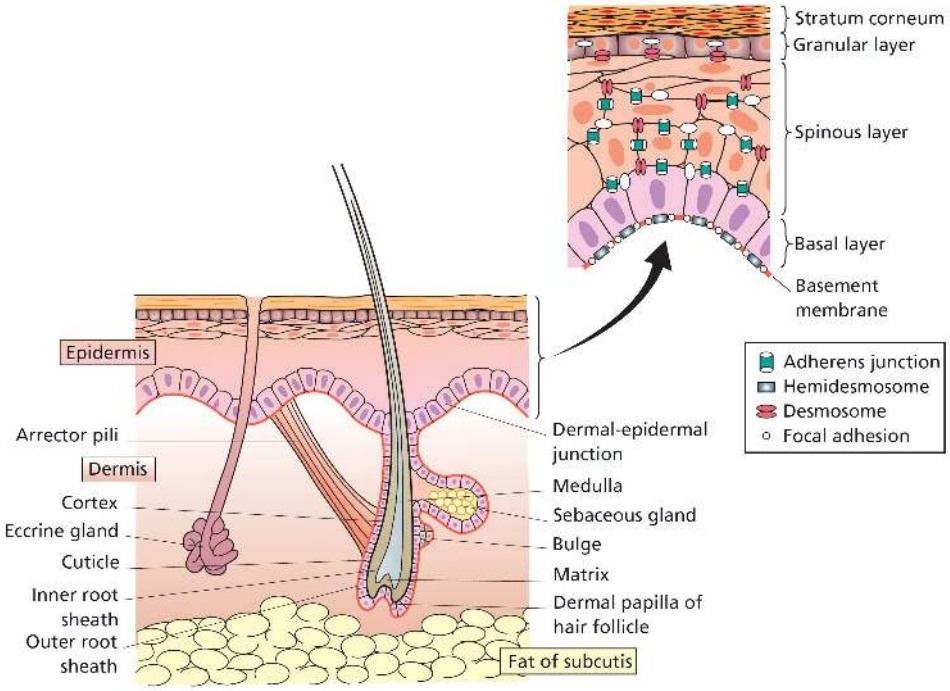

Figure 3.1: Schematic cross section of the human skin[25]

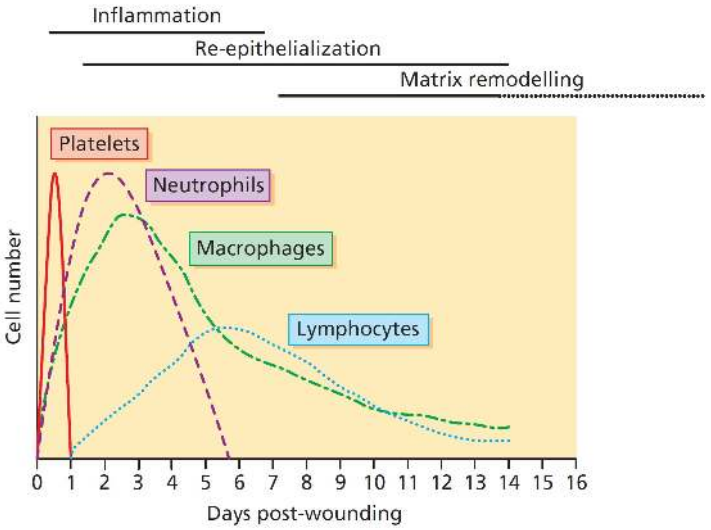

Figure 3.2: Cells present in a wound during the first two weeks of wound healing[25]

plug forms. Inflammatory mediators are released which lead to a permeabilization of the cells near the edge of the wound. This allows for a rapid exchange of intracellular and extracellular ions. The mediators also cause vasodilation (dilation of vessel walls) which results in an increased blood flow to the damaged tissue. Because of this, neutrophils enter the wound and start cleaning it of bacteria and other foreign objects. During this phase, neutrophils are the predominant inflammatory cells. The invading bacteria are killed by phagocytosis and the release of reactive oxygen species (ROS). Fibroblasts begin to lay down what is called a provisional matrix of granulation tissue. This matrix serves as a guide for the incoming migrating cells. After several days the neutrophils are destroyed by apoptotic cell death (programmed cell death) or phagocytosis by macrophages. At this point lymphocytes become the main killers of pathogens.

Re-epithelialization occurs approximately 24 hours after wound formation. Keratinocytes migrate from the edge of the wound or from hair follicles or sebaceous glands where they form a new epidermis. Due to a change in the ratio of magnesium and calcium ions as a result of keratinocyte damage, other keratinocytes adopt what is dubbed a migratory phenotype[26]. These keratinocytes elongate to aid cell movement and eventually dissect the previously formed fibrin clot. The generation of electric fields in wounds has also been measured[27] and its effects on keratinocyte migration have been studied[28]. Electric fields were able to induce directionality in cell migration and in combination with growth factors[29] an increase in migration was observed.

The last phase of skin healing is matrix remodelling in which fibroblasts enter and proliferate in the provisional wound matrix. These fibroblasts originate predominantly from deeper layers of the dermis and the underlying fat, rather than from the edges of the dermis. They can also originate from bone marrow in the form of fibrocytes[30] and surrounding tissue. The fibroblasts produce collagen which is organized in bundles, cross-linked and placed along tension lines, resulting in the eventual scar. This final phase takes longest to complete; it can last up to a year or longer. More information on wound healing can be found for example in chapter 14 of *Rook's Textbook of Dermatology*[25] or in review papers (e.g. Singer and Clark[31]).

3.3 Burn wound healing

A burn wound is different in terms of healing because of its different nature, the consequences of which are explained in this section. Three types of burn wounds exist; first degree burns in which there is only damage to the epidermis, second degree burns in which also the dermis is damaged and third degree burns where the damage reaches all the way down to the subcutis. In practice, wounds are classified in four categories, in increasing severity. The formation of blisters (mostly between the epidermis and dermis) is the first category, followed by expected healing within 2 to 3 weeks without surgery, healing not expected within this period (surgery necessary) and damage of the complete dermis (sometimes down to the bone tissue)[25]. The distinction between the second and third category is not always immediately clear as a wound can change over the course of the first few days, switching from a second to a third category wound. In contrast to disruptive or incisional wounds, burn injury results in extensive damage to the blood vessels thus causing a restriction in blood flow.

According to Shakespeare[32], three different zones can be identified in a burn wound. The first zone shows signs of blood vessel coagulation which leads to irreversible skin death. Around this zone the blood flow is restricted and on the edge of the injured tissue, there is an area exhibiting hyperaemia (increased blood flow). Figure 3.3 shows a schematic representation of the three different zones. As a result of the blood vessel coagulation in the central part of a burn wound, there is no haemorrhage so that there is no inflow of blood in the wound shortly after injury which leads to a limited creation of a fibrin plug and no defined location and tissue volume for a provisional matrix.

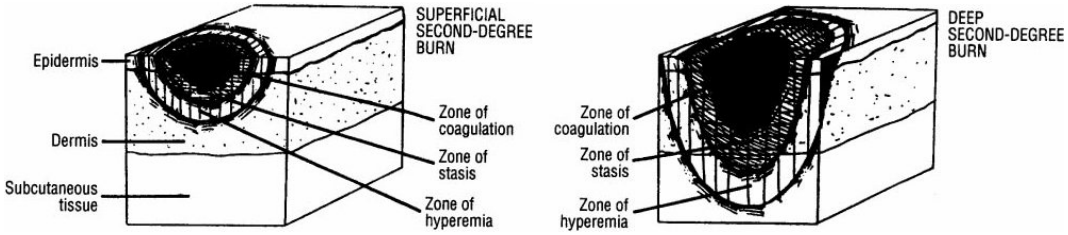

(a) Superficial second-degree wound (b) Deep second-degree wound

Figure 3.3: Schematic of two different burn wounds indicating the three identifiable zones of a burn injury[33].

The depth of the burn wound is a large influencing factor in the healing process and it determines the necessary treatment. This is mostly due to the fact that epithelial cells in a full thickness wound (reaching the subcutis) are not available from the basement membrane or hair follicles of the skin and as a result have to be provided by the edge of the wound. This greatly reduces the efficiency of the healing process and can even become practically unmeasurably slow. These full thickness wounds as a result need to be treated by applying split thickness skin grafts, which contain the epidermis and a part of the dermis. Grafts can for example be used from the patient's own body, from a cadaver, from a pig or of synthetic origin.

Another distinction between ordinary wounds and burn wounds is the increased susceptibility to wound infections, especially when large areas of the skin are affected. A moist wound bed in combination with necrotic tissue and reduced blood flow due to thrombosis of blood vessels easily leads to colonization as it forms an excellent medium for bacterial growth. Burn patients are also regularly affected by smoke inhalation injury, further increasing the chance of infection[34]. Generally, a good indication of a burn wound infection is attained by taking samples of the wound and determining the bacterial concentration. A concentration of 10^4[35] or 10^5[33] CFU/g of tissue is generally considered to indicate a burn wound infection.

3.4 Conventional treatment of burn wound infections

Conventionally, bacterial infections of wounds are treated with topical[2] antimicrobials such as silver sulfadiazine, silver nitrate solution, mafenide acetate or other methods such as *Acticoat* which contain nanocrystaline silver. The effectiveness of these kind of silver dressings is shown in figure 3.4. In this investigation, 10 µl of solution containing the bacteria was added to 1 cm squares of dressing pretreated with 800 µl of distilled water, making it an in vitro experiment. These results show that the most effective dressings achieve a reduction of approximately 10^6 CFU/ml over a period of 24 hours.

Intravenous treatment can also be performed by administering for example penicillins, cephalosporins or aminoglycosides. However, resistance to antibiotics can occur in as few as fourteen days in some institutions[37].

3.5 Gram staining

Gram staining is a technique that is used to differentiate bacteria based on their cell wall properties. Crystal violet is added to the bacteria, after which iodine is added to retain the stain in specific cells. Gram-positive bacteria retain the applied stain after washing with

[2]Topical drugs are applied on the surface of the body such as skin or mucous membranes.

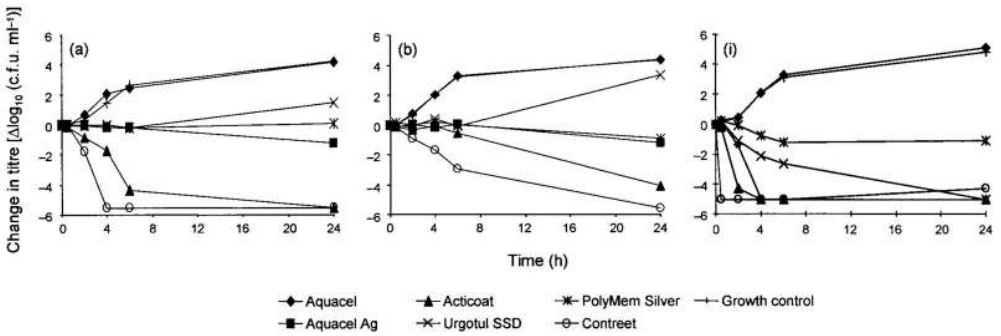

Figure 3.4: Bactericidal effect of silver wounds dressings in vitro as a function of time on (a) methicillin-resistant Staphylococcus aureus, (b) methicilin-sensitive Staphylococcus aureus and (i) Pseudomonas aeruginosa. Adapted from [36].

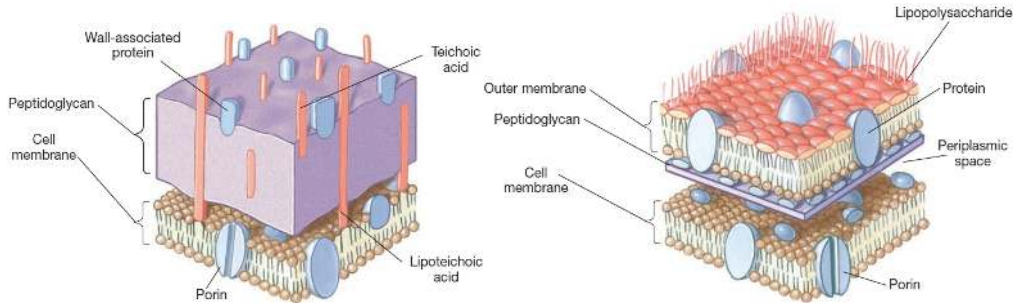

(a) Gram-positive wall (b) Gram-negative wall

Figure 3.5: Gram-positive and Gram-negative cell walls.[38]

ethanol and water whereas Gram-negative bacteria do not. These differences arise from the different cell wall structures. Gram-positive bacteria have a relatively thick peptidoglycan layer which allows it to retain stains better, whereas Gram-negative bacteria have a thinner cell wall but a more complex structure. The cell structure of Gram-positive and Gram-negative bacteria is shown in figure 3.5. To be able to clearly see the difference between Gram-negative and Gram-positive bacteria, a counterstain of safranin is applied after washing, further emphasizing the difference in color.

Pseudomonas aeruginosa is a Gram-negative bacterium while Staphylococcus aureus is a Gram-positive bacterium. Because of this difference in cell wall structure, the effect of plasma treatment of these two bacteria is expected to be different. This difference in susceptibility to plasma treatment has previously been discussed in literature. Gram-negative bacteria are generally more susceptible to argon plasma treatment by a high power *MicroPlaSter* β atmospheric pressure plasma torch. This increased sensitivity is possibly due to a thinner cell wall structure and a more irregular surface, leading to larger electrostatic effects and higher permeability of reactive molecules. Staphyloccocus aureus however is found to be approximately as susceptible as Pseudomonas aeruginosa to plasma treatment[39], indicating that Gram classification alone is not sufficient to determine the sensitivity of bacteria to plasma treatment. As a result the difference in bactericidal effect of the plasma treatments performed in this work is not expected to be large.

3.6 Pseudomonas aeruginosa

As mentioned before, Pseudomonas aeruginosa is a Gram-negative opportunistic pathogen. It is intrinsically resistant to antibiotics and disinfectants and because of this it is very prominent. The bacteria can show either a biofilm or planktonic cell phenotype. A planktonic cell phenotype grows in a liquid culture medium in microcolonies whereas the biofilm phenotype can attach to an inert surface and, by producing large amounts of exopolysaccharides, form a slime layer, also called a biofilm. The formation of a biofilm protects the bacteria against the immune system and can cause uncontrolled inflammation in the host through the production of immune complexes. Also, the bacteria are shielded by it and therefore less susceptible to topical treatments.

Unless otherwise specified, the Pseudomonas strain used in this work is PAO1. The PAO1 strain contains 6.3 million base pairs and has been completely sequenced[40]. Because of this, it is very well known and there is a lot of experience in working with this strain.

Yang et al. [41] used a 30 W argon plasma at 6.2 Pa pressure with a gas flow of 20 cm^3/min to treat medical PET samples contaminated with Pseudomonas aeruginosa. The samples were placed at three different positions, the discharge zone (0 to 40 cm from source), the afterglow zone (40 to 60 cm from source) and the remote zone (60 to 80 cm from source). The results of the treatment are shown in figure 3.6. (a) shows the untreated rod-shaped Pseudomonas bacteria, the other figures show the results of treatments in the discharge, afterglow and remote zone respectively. Especially bacteria treated using the discharge zone show extensive cell wall damage and consequent deactivation of bacteria. While in the other pictures the results of plasma treatment are less apparent, a clear reduction of bacterial concentration was still found.

The effect of an atmospheric pressure plasma jet on Pseudomonas aeruginosa was studied by among others Matthes et al.[42] and Daeschlein et al.[43]. In Matthes' study, the bacteria were treated on agar plates using a *kINPen* plasma source, both using pure argon, pure helium, pure air and mixing with oxygen. The diameter of the area cleared of bacteria is measured as a function of gas composition and treatment time. Also the log reduction of the bacterial load was determined. A maximum log reduction of approximately 1.5 was achieved using argon mixed with oxygen at an initial 10^5 CFU treated for 2 minutes. Daeschlein shows a log reduction of 4, also using the *kINPen*, after a treatment of 6 minutes. In this case, the starting amount of bacteria on the agar plate was approximately $2.5 \cdot 10^2$ CFU. The difference in these results shows a dependency on the amount of bacteria present before treatment.

Laroussi et al. [44] treated the Pseudomonas bacterium on nitrocellulose filter membrane and in LB solution using a DBD helium plasma mixed with air. The highest bactericidal effect was obtained on the filter after 15 minutes treatment time, attaining a log reduction of 5. Treatment in LB resulted in a maximum log reduction of 1 after the same amount of time.

The bactericidal efficacy of a helium nitrogen plasma jet on Pseudomonas biofilms on polystyrene microplates was studied by Abramzon et al.[45], which resulted in a 4 log reduction in bacterial density after 60 minutes of treatment. As expected, because of the protective nature of the biofilm, the bacteria are less affected by plasma treatment.

3.7 Staphylococcus aureus

A common Gram-positive bacterium found in burn wounds is Staphylococcus aureus. It is carried by approximately 30% of the population. Especially hospitalized patients are susceptible to Staphylococcus aureus colonization. A well known variant is the Methicillin-resistant Staphylococcus aureus (MRSA).

Atmospheric pressure plasma treatments of MRSA have been performed by Lee et al. [46]. A 1kW microwave 100 slm argon plasma source was used to treat the bacterium on

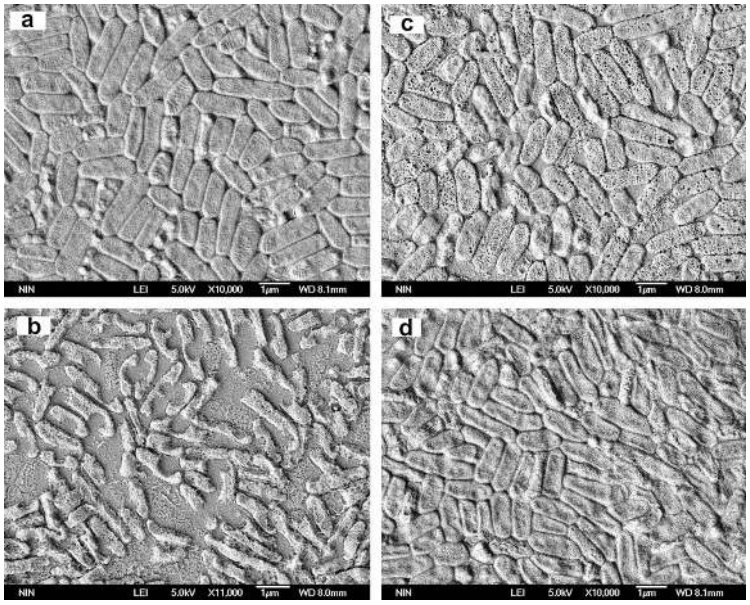

Figure 3.6: Pseudomonas aeruginosa bacteria on medical PET treated with a 30 W low pressure plasma at the discharge zone (b), the afterglow zone (c) and the remote zone (d). (a) is an untreated control sample.[41]

glass slides. Figure 3.7 shows SEM images of the bacteria before and after treatment. In the picture before plasma treatment, the spherical structure of the bacteria can clearly be seen. In this case, any of the shown treatment durations result in almost complete cell destruction.

Aside from looking at Pseudomonas aeruginosa, Matthes et al.[42] also investigated the effects on Staphylococcus aureus. A maximum of 2 log reduction was achieved for an argon plasma mixed with oxygen treated for 2 minutes. The same 10^5 CFU were present before treatment. Daeschlein et al.[43] found a reduction from 10^2 to 1 CFU after 6 minutes of treatment.

Biofilms of Staphylococcus were treated by Cotter et al.[47], showing a 5 log reduction after 90 minutes of treatment, again showing the protective effects of the biofilm.

3.8 Keratinocytes

The most prevalent cell in the human skin is the keratinocyte. Approximately 95% of all the cells in the human skin are keratinocytes. Their main function is environmental shielding from for example pathogens, UV and heat but also preventing water loss.

Any plasma treatment of skin should have only a limited detrimental effect on keratinocytes as they are important in wound healing, as shown in section 3.2. As human cells lack a (peptidoglycan) cell wall and have a weaker cell membrane than bacteria, this makes them more susceptible to external stress. However, due to the difference in size (bacteria are approximately 1 µm in length whereas keratinocytes are typically an order of magnitude bigger) they have a more favorable cell wall surface to cell volume ratio.

3.9 Fibroblasts

As stated before, one of the most important cells in the healing process of human skin are fibroblasts. They lay down a framework for wound healing by producing among others

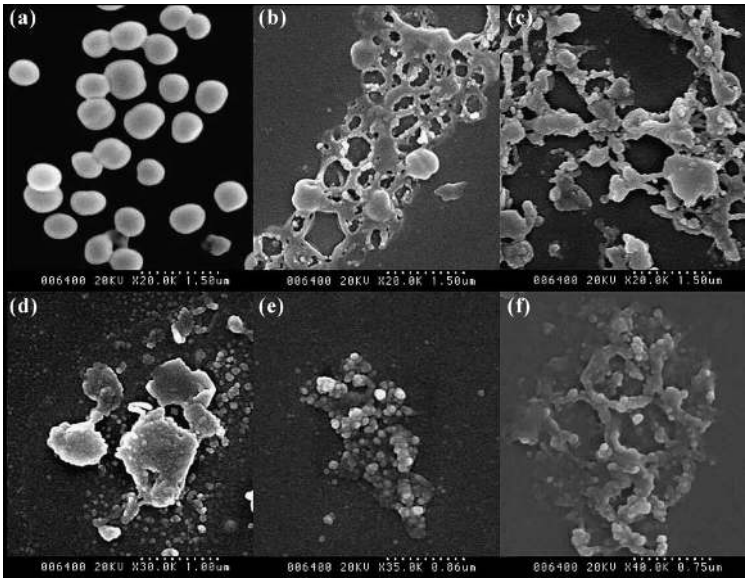

Figure 3.7: MRSA bacteria on glass slides treated with a 1kW atmospheric pressure microwave plasma for 1 (b), 2(c), 3(d), 4(e) and 5(f) seconds. (a) shows an untreated control sample.[46]

collagens and elastic fibers. An important property of fibroblasts is their ability to migrate and thereby assist wound healing.

The effect of a helium atmospheric pressure plasma needle on fibroblast proliferation was investigated by Tipa et al.[48]. Fibroblasts were cultured on a substrate in a liquid medium, after which a scratch in the fibroblast layer was made to obtain a wound model. Some samples were treated with the helium plasma while submersed in a thin fluid layer (composition not stated in paper) and the proliferation was compared to control samples. Plasma treated samples showed an increase in the rate of closure of the 'wound' and a more even distribution of cells on the substrate, as is seen in figure 3.8. This shows that apart from being bactericidal, atmospheric pressure plasma treatments can have beneficial effects on human cells as well, provided that the right treatment conditions and liquid media are found.

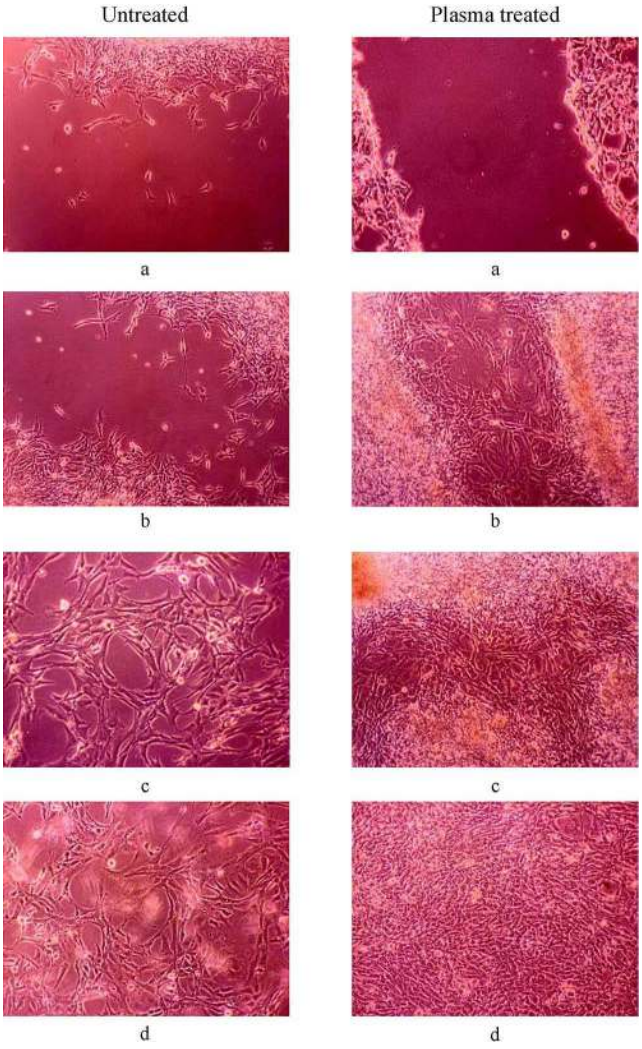

Figure 3.8: Proliferation of plasma treated and control (non-treated) fibroblast cultures after applying a scratch. (a) directly after applying scratch, (b) after 1 day of incubation, (c) after 2 days of incubation and (d) after 3 days of incubation. Adapted from [48].

Chapter 4

Experimental setup and diagnostics

This chapter introduces the plasma source and the various diagnostic methods used in this work. The used diagnostics include power measurements, spatially resolved optical emission spectroscopy, absolute UV-flux measurements, molecular beam mass spectrometry, pH measurements, liquid ion chromatography and hydrogen peroxide concentration measurements. Finally the preparation and treatment procedures of cells and bacteria as well as biological diagnostics such as optical density measurements and cell viability measurements are presented.

4.1 Plasma source

The plasma source used for the measurements presented in this report is an atmospheric pressure plasma jet that consists of a plastic enclosure. A carrier gas, usually helium or argon possibly mixed with air, is passed through a quartz glass tube containing a needle shaped metal electrode. The needle is connected via a matching circuit to a radio frequency power amplifier driven at 13.56 MHz by a wave generator. The matching circuit consists of a coil of 41 1/2 windings. This rudimentary circuit design (compared to an L-section or pi-section) is used to be able to easily and accurately measure power dissipation as there are no branches of capacitors to ground. As a result the current losses due to stray resistances are minimized and the entire current passes through the plasma source. A secondary electrode is connected to ground. Two different secondary electrode geometries are used in this work; a plate electrode in front of the tube and a ring electrode placed around the tube. A schematic of the setup with the ring electrode is shown in figure 4.1. The two different electrode geometries are introduced in figure 4.2. When using the plate electrode, the distance between the plate electrode and the needle can be varied to achieve different plasma conditions.

The gas flow is controlled by *Brooks 5850E* mass flow controllers, the signal is generated by *Agilent 33220A* function generators and the signal is amplified by an *Amplifier Research 75AP250* or *Amplifier Research 75A250* power amplifier. One mass flow controller can achieve a maximum flow of 1.5 slm of argon while the other controller is limited to 200sccm of air. For pulsed signals two *Agilent* function generators are used simultaneously. One function generator is set to frequency-shift keying (FSK) and is triggered by the second function generator which sends out TTL pulses at 20 kHz. Frequency-shift keying is essentially a digital version of frequency modulation; it changes the frequency between two set values, for example from 1 µHz to 13.56 MHz, effectively switching from a DC signal to the desired RF signal. FSK in this setup yields better defined pulse signals than for example amplitude modulation (AM). Not only the pulsing frequency but also the duty cycle can be set. In this

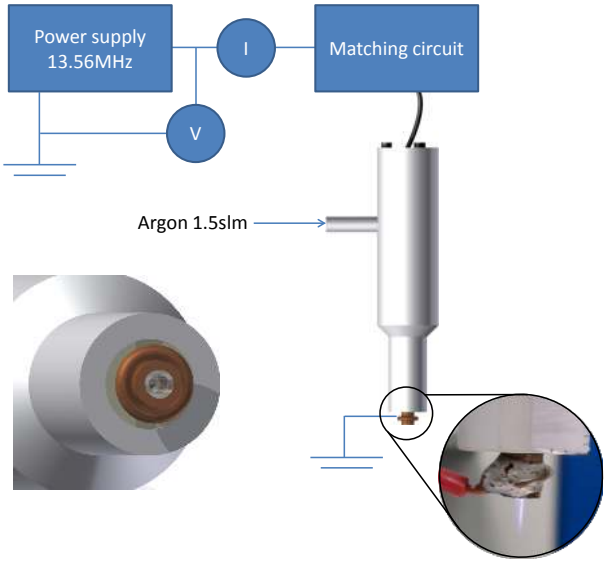

Figure 4.1: Schematic representation of the setup equipped with the ring electrode showing the power supply, voltage and current probes, matching circuit, plasma source and a photograph of the plasma source operating in argon at a power of 1.3 W.

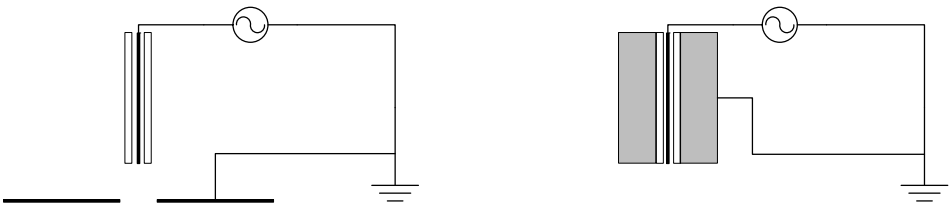

(a) Plate electrode schematic

(b) Ring electrode schematic

Figure 4.2: Schematic geometry of the two different electrode configurations used. The RF source, the powered needle, the quartz glass tube and the plate or ring electrode are shown.

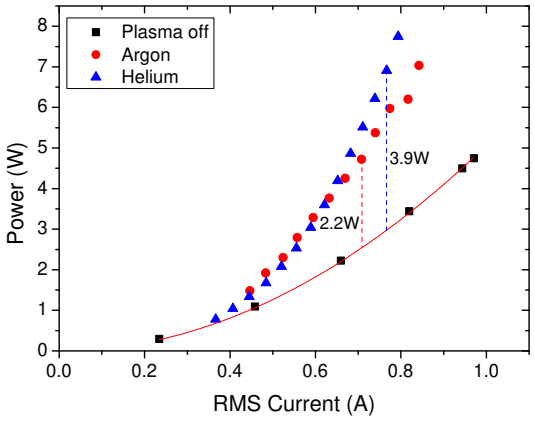

Figure 4.3: Examples of power measurements with and without plasma for the plate electrode geometry. The shown fit is the function $P_{off} = 5.06 \cdot I_{RMS}^2$. The difference between the plasma off and plasma on power at the same RMS current (dashed lines) is the plasma dissipated power.

work, the duty cycle always refers to the percentage of the time the pulse is applied. So a duty cycle of for example 20% means that the plasma is on 20% of the time.

4.2 Power measurements

Power dissipation is measured by measuring the voltage (100x *Tektronix P5100*) and current (*Pearson 2877* current probe). The voltage and current is measured between the power supply and the matching circuit as shown in figure 4.1, to avoid a large influence of the capacitance of the voltage probe on the matching. To correct for the relative time delay in the probe cables, a vacuum capacitor is connected to the power supply (replacing the matching circuit and the plasma source in figure 4.1) and the deviation from a 90 degree expected phase shift between voltage and current is measured. In this case the measured delay time (or τ_{shift}) is approximately 2.9 ns.

To measure the total power dissipation, the voltage and current signals are linearly interpolated and corrected for the time delay. Interpolation is needed to allow for more accurate corrections of the time delay as the raw data has a 1 ns time resolution. After this the product of the measured voltage and current is integrated using trapezoidal interpolation and divided by the elapsed time;

$$P_{total} = \frac{1}{T} \int_0^T U(t) I(t + \tau_{shift}) dt. \tag{4.1}$$

The power is measured both with and without gas flow (i.e. with and without plasma production). The power dissipation without plasma production is a quadratic function of the RMS current, an example of which is shown in figure 4.3. The coefficient depends on the electrode type and electrode spacing (in the case of the plate electrode) used and may also change if the plasma source is in proximity to other objects. It is therefore vital to always measure the power dissipation without plasma production at the same settings as the actual plasma power measurements. To obtain the power dissipated in the plasma the power dissipation without plasma production is subtracted from the measured total power dissipation at the same RMS current;

$$P_{diss}(I_{RMS}) = P_{on}(I_{RMS}) - P_{off}(I_{RMS}). \tag{4.2}$$

This is possible because the power dissipated in the coil was found to be constant at a constant RMS current regardless of whether or not a gas flow is supplied (thus with or without plasma production) by Hofmann et al.[49]. The cause of the higher power dissipation in helium at the same RMS current is explained in section 5.1.

In the pulsed RF measurements, the pulse width (and thus duty cycle) is measured and the power dissipation during the pulse is multiplied with the duty cycle to obtain the time averaged power dissipation.

The power measurement method discussed above is compared with measurements performed with an *Amplifier Research PM2002* power meter equipped with *PH2000* dual diode power heads, which in this case is considered to be the benchmark. The power meter uses a bidirectional coupler to separate forward and reflected power and attenuate the signal. A double diode power head measures the attenuated power. A schematic of a double diode power head is shown in figure 4.4. It contains two diodes, two capacitors and one 50 Ω resistor. The following derivation considers a single diode power sensor, which only consists of one capacitor and one diode. The diode rectifies the current, which is then given by

$$I = I_s \left(e^{(eV/k_B T n)} - 1 \right), \tag{4.3}$$

where I_s is the saturation current, e is the elementary charge, V is the voltage measured by the voltage meter , k_B is the Boltzmann constant, T is the temperature and n is a quality factor, usually between 1 and 2. For low voltages, a Taylor expansion can be performed, and after separating DC and RF components

$$I \approx I_s \left(\frac{e}{k_B T n} V_{DC} + \frac{1}{2} \left(\frac{e}{k_B T n} \right)^2 V_{DC}^2 + \ldots + \frac{e}{\sqrt{2} k_B T n} V_{RF} + \frac{1}{4} \left(\frac{e}{k_B T n} \right)^2 V_{RF}^2 + \ldots \right). \tag{4.4}$$

Neglecting the first order RF component (as its average is zero) and all higher order components:

$$I_{DC} \approx I_s \left(\frac{e}{k_B T n} V_{DC} + \frac{1}{4} \left(\frac{e}{k_B T n} \right)^2 V_{RF}^2 \right) = 0. \tag{4.5}$$

The DC current is indeed zero because of the high impedance of the voltage meter. At this point, using the 50 Ω resistance value, the power dissipation can be written as

$$-V_{DC} = \frac{25e}{k_B T n} P_{RF}. \tag{4.6}$$

As stated before, the above derivation is valid for a single diode power sensor, the addition of another diode circuit branch results in a more accurate measurement of especially higher harmonics. In order to be able to neglect the higher order components in equation 4.4, V_{RF} has to be small. This is typically achieved by using an attenuator. The attenuation of the diode power meter used in this work is -50 dB. More information on diode power sensors is available in for example *Radio frequency & microwave power measurement*[50].

In figure 4.5 the plasma dissipated power is measured using both methods for two different Amplifier Research amplifiers, named AR1 and AR2. AR1 (*Amplifier Research 75AP250*) is used in Eindhoven whereas AR2 (*Amplifier Research 75A250*) is used in Beverwijk. Both methods are in good agreement, showing a maximum standard deviation between amplifiers and between measurement methods of 0.5 W at approximately 8 W of plasma dissipated power and 0.1 W at at approximately 1.3 W of plasma dissipated power. Measuring the power using voltage and current measurements has the added advantages of being more compact, less expensive and it also provides insight in voltage and current behavior and phase shifts.

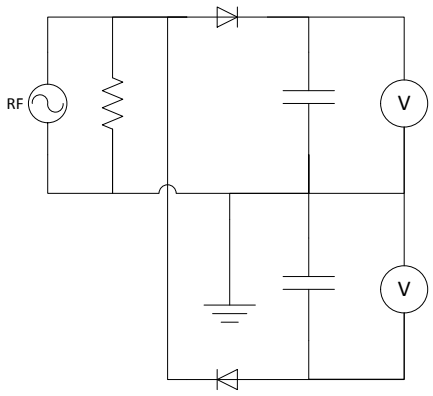

Figure 4.4: Simplified schematic of a double diode power sensor.

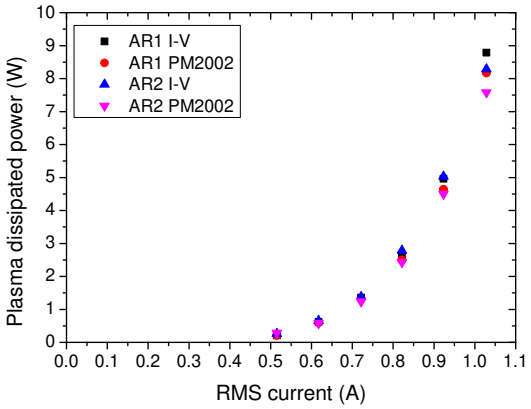

Figure 4.5: Plasma dissipated power as a function of RMS current for both *Amplifier Research* amplifiers measured using both the current-voltage data and the *Amplifier Research PM2002* for a helium plasma with a flow of 1slm.

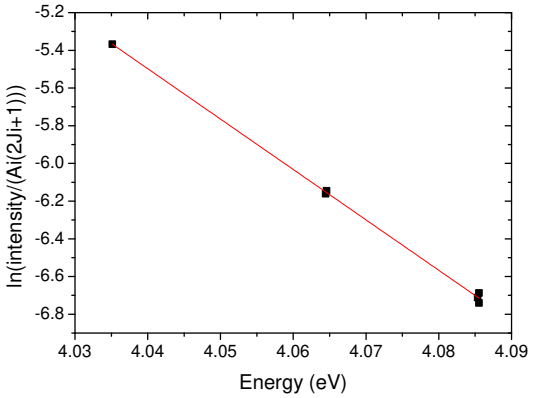

Figure 4.6: Example of a Boltzmann plot of a 309nm OH(A-X) transition in an argon plasma. The slope of the linear fit is (-26.74±0.44) eV^{-1}, resulting in a rotational temperature of (434±7) K.

4.3 Spatially resolved optical emission spectroscopy

To be able to measure the gas temperature inside the plasma, spatially resolved optical emission spectroscopy measurements are performed using a *Jobin-Yvon* monochromator in combination with a two lens configuration to image the plasma jet on the entrance slit of the monochromator. The resulting image shows the spectrum as a function of position. This allows for axial as well as radial temperature profile measurements by changing the orientation of the plasma source. In the case of an argon plasma, the relative intensities of the peaks of the 309 nm OH (A-X) transition are measured. The reason for choosing the OH (A-X) transition is that this is found to produce an accurate gas temperature measurement in argon[49]. The rotational temperature is obtained using so-called Boltzmann plots. The intensity of a rotational line with label i in a given vibrational band is given by

$$I_i \propto A_i \left(2J_i + 1\right) e^{-\frac{E_i}{k_B T_{rot}}}, \tag{4.7}$$

where

$$E_i = B_v J_i \left(J_i + 1\right). \tag{4.8}$$

Here, A_i is an Einstein emission coefficient, J_i is a rotational number and E_i is the rotational energy. $(2J_i + 1)$ corrects for the degeneracy of the rotational states and B_v is the rotational constant. By measuring the relative intensities and using known values for A_i, J_i and E_i, the rotational temperature is obtained by calculating the slope of the normalized intensity as a function of the rotational energy:

$$\frac{d}{dE_i} \ln\left(\frac{I_i}{A_i \left(2J_i + 1\right)}\right) = -\frac{1}{k_B T_{rot}}. \tag{4.9}$$

A plot is made of $\ln\left(\frac{I_i}{A_i(2J_i+1)}\right)$ as a function of E_i, which is called a Boltzmann plot. The data is fitted linearly and from the resulting slope the rotational temperature is calculated. An example of a Boltzmann plot, the calculated slope and the resulting calculated rotational temperature is shown in figure 4.6.

The error bars shown in the acquired temperature profiles presented in section 5.2 are calculated from the uncertainty of the linear fit. As a result, in a Boltzmann plot containing only a few closely spaced measurement points, the error resulting from this method can be large.

The question remains whether or not the rotational temperature of the plasma is equal to the gas temperature. This validity of this equality depends on the timescale of rotational

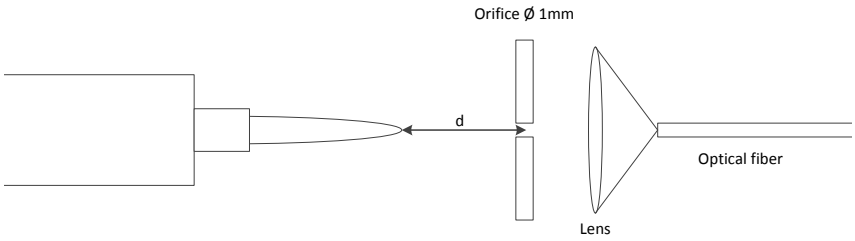

Figure 4.7: Schematic representation of the measurement setup used to measure the UV-flux emitted by the plasma. The distance between the tip of the plasma plume and the orifice is indicated by d.

states which needs to be faster than the radiative lifetime[51]. Generally this is only valid for atmospheric pressure discharges and the lower rotational numbers. For OH (A), it is known that the production process can lead to specific rotational excitation. This introduces the need for thermalization of the rotational states to allow the rotational temperature to give an accurate representation of the gas temperature. The process of thermalization is easier at high pressure, lower rotational numbers and if the collisional quenching is not too high as this reduces the effective lifetime of the excited states[52].

In addition to measuring the gas temperature inside the plasma, the gas temperature downstream is measured using a thermocouple. By aligning the thermocouple coaxially to the plasma source, a temperature profile is measured. It has to be noted however that in between the data gathered by optical emission spectroscopy and thermocouple measurements there is a range in which no measurement can be performed as the plasma has a tendency to 'stretch' itself out towards the thermocouple when in close proximity, altering the plasma parameters.

4.4 UV-flux measurements

In order to get an estimation of the possible biological effects of UV radiation emitted from the plasma jet during treatment, the emission spectrum is measured using an *AvaSpec 3648* fiber-optic spectrometer. The optical fiber is connected to a lens which is coaxially aligned with the plasma. Between the plasma jet and the lens a ceramic disc with an orifice of 1 mm is placed. The orifice makes sure that the diameter of the plasma plume does not influence the total amount of collected light. A schematic overview of the setup is seen in figure 4.7.

To check if the distance between the plasma tip and the orifice (d in figure 4.7) is important, the spectra of an argon plasma are recorded in two series. One series uses a constant distance between source and orifice while in the other series the position of the plasma source is adjusted over a range of approximately 4 cm so that the distance of the plasma tip to the orifice is constant, as the length of the plasma increases with increasing power. The resulting spectra are corrected for integration time and integrated over the total measurable UV range of the spectrometer (200 nm to 400 nm). The resulting UV intensities are plotted as a function of plasma power dissipation in figure 4.8. It shows that both changing the position of the plasma source ('Variable position') and keeping it fixed ('Fixed position') lead to practically the same values and as such the position of the plasma source can be kept constant, which is beneficial for the reproducibility of the measurements and leads to a much more efficient gathering of measurement data. It is clear that in this range the plasma plume is not a point source.

The spectrometer is calibrated by using a deuterium lamp with a known spectral irradiance (in $\mathrm{Wm^{-2}nm^{-1}}$) at a fixed distance in the range of 200 to 400 nm. This allows for

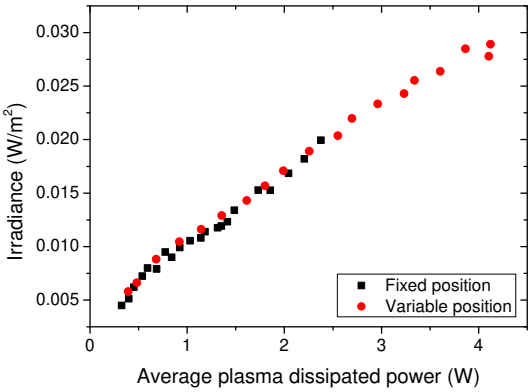

Figure 4.8: Integrated spectral irradiance over the total measurable UV range (200 nm to 400 nm) of an argon plasma using the ring electrode as a function of the average power dissipated in the plasma. 'Fixed' and 'Variable' denote either a fixed or variable position of the plasma source relative to the orifice.

absolute measurements of the irradiance generated by the plasma jet.

For the additional measurements shown in this report, the amount of UVA, UVB and UVC is calculated by integrating the obtained spectrum from 315-400 nm, 280-315 nm and 200-280 nm respectively. The UVC range measured is not the total UVC range (which ranges from 100-280 nm) due to the lack of spectrometer sensitivity below 200 nm. This is not expected to pose a problem as UV of a wavelength shorter than 200 nm is considered to be vacuum UV, which is absorbed strongly by air and water, as discussed in more detail in chapter 7.

4.5 Mass spectrometry

To gain insight in the production of ions, a mass spectrometer is used. A mass spectrometer separates incoming atoms and molecules by mass to charge ratio m/q. For this to be possible the neutral atoms and molecules first have to be ionized, after which they are passed through a quadrupole and finally impact on a detector. The ionizer in this case is a filament which produces electrons at a defined energy and emission current. The ionized particles enter the quadrupole which consists of four parallel rods of which each two opposing rods are supplied with a certain voltage, consisting of a DC component and a radio frequency component, as is seen in figure 4.9.

The following derivations can be found in various books on mass spectrometry, such as De Hoffmann and Stroobant[54]. When passing through this quadrupole, the ions will be affected by a force induced by the resulting electric fields:

$$F_x = m\frac{d^2x}{dt^2} = -ze\frac{\partial \Phi}{\partial x} \tag{4.10}$$

$$F_y = m\frac{d^2y}{dt^2} = -ze\frac{\partial \Phi}{\partial y}, \tag{4.11}$$

where m is the mass and ze is the ion charge. The potential Φ as a function of position is given by

$$\Phi(x,y) = \frac{\Phi_0\left(x^2-y^2\right)}{r_0^2} = \frac{\left(x^2-y^2\right)\left(U - V_{RF}\cos(\omega t)\right)}{r_0^2}, \tag{4.12}$$

where U is the DC component of the potential and V_{RF} is the RF amplitude of the potential. ω is the frequency of the applied RF wave and r_0 is the radius of the formed circle between

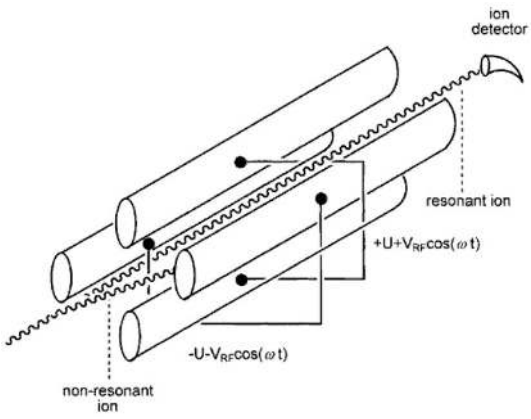

Figure 4.9: Schematic representation of a quadrupole[53]. Actual ion trajectories are more complicated than shown in this figure.

the quadrupole rods. Differentiating and rearranging produces

$$\frac{d^2x}{dt^2} + \frac{2ze}{mr_0^2}\left(U - V\cos\left(\omega t\right)\right)x = 0 \tag{4.13}$$

$$\frac{d^2y}{dt^2} - \frac{2ze}{mr_0^2}\left(U - V\cos\left(\omega t\right)\right)y = 0 \tag{4.14}$$

for the x and y equations of motion. The format of these equations was established in 1868 by physicist Mathieu in the form [55]

$$\frac{d^2u}{d\xi^2} + \left(a_u - 2q_u\cos\left(2\xi\right)\right)u = 0, \tag{4.15}$$

where $\xi = \frac{\omega t}{2}$. This differential equation has solutions that may be expressed as[56]

$$u = c_1 e^{\mu\xi}\sum_{n=-\infty}^{\infty} C_{2n}e^{2in\xi} + c_2 e^{-\mu\xi}\sum_{n=-\infty}^{\infty} C_{2n}e^{-2in\xi}. \tag{4.16}$$

In this equation c_1 and c_2 are integration constants and C_{2n} and μ depend on q and a, not on the initial conditions. The latter two are given by

$$a_u = a_x = -a_y = \frac{8zeU}{m\omega^2 r_0^2} \tag{4.17}$$

$$q_u = q_x = -q_y = \frac{4zeV}{m\omega^2 r_0^2}. \tag{4.18}$$

The criterion for a certain ion to be able to pass through the quadrupole is that both the x and y positions are within the confines of the rods. A way to visualize this is by assigning stability regions as a function of a_u and q_u for both the x and y axes, as is seen in figure 4.10a. These regions may overlap at multiple positions, indicated in the figure by A through D. The most commonly utilized region in mass spectrometers is A as it is the largest area in which both the x and y trajectories are stable. This area is shown enlarged in the bottom right of the figure. An example of a stable ion trajectory in the x-y plane (the z-axis being the bore of the quadrupole) is shown in figure 4.10b.

After exiting the quadrupole the resulting ions are detected via secondary electron emission in an electron multiplier.

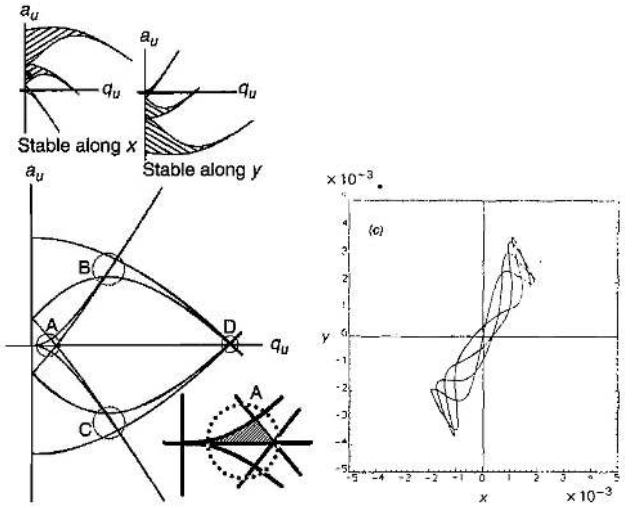

(a) Stability regions[54] (b) Stable ion trajectory in the x-y plane[56]

Figure 4.10: Stability regions along the x and y axes as a function of a_u and q_u and an example of a stable ion trajectory in the x-y plane.

As the mass spectrometer operates at low pressure to reduce the amount of collisions of the ions, a transition has to be made from atmospheric pressure to vacuum. This is achieved by using a small diameter orifice to sample the plasma, after which three successive pumping stages separated by skimmers[1] reduce the pressure to approximately $5 \cdot 10^{-7}$ mbar at the position of the mass spectrometer.

The sharp gradient in pressure causes an increase in flow velocity, and the flow becomes sonic if the pressure ratio [57]

$$\frac{P_o}{P_b} > G, \tag{4.19}$$

where

$$G \equiv \left((\gamma+1)/2\right)^{\gamma/(\gamma-1)}, \gamma = \frac{c_p}{c_v}. \tag{4.20}$$

The value of γ is 1.67 for monatomic gases and 1.4 for dry air. This leads to values of 2.1 and 1.9 for G respectively. When the requirement on the pressure ratios is met, the pressure in the flow becomes independent of the background pressure in the vessel and is given by P_0/G. Information coming from downstream travels at the speed of sound and thus the flow does not 'feel' any of the downstream boundary conditions. This means that the pressure in the flow is higher than the background pressure and an expansion of the gas flow will occur. In a supersonic flow the flow velocity increases as the flow area increases. As a result, the velocity in the expansion will be much higher than the speed of sound. As the properties in the supersonic part of the expansion are independent of external conditions, this region is often called the zone of silence. However, at some point the gas will overexpand and the pressure will decrease to a value below the background pressure, which results in the formation of shock waves.

An expansion as discussed above is called a molecular beam expansion or a free jet expansion and a schematic overview of such an expansion is shown in figure 4.11. It shows the before mentioned zone of silence as well as Mach disk and barrel shock waves. In the case of the mass spectrometry setup this molecular beam expansion is used to sample within the zone of silence, where there are few collisions between particles. From the pressure ratio of

[1] Truncated hollow cones with a circular opening.

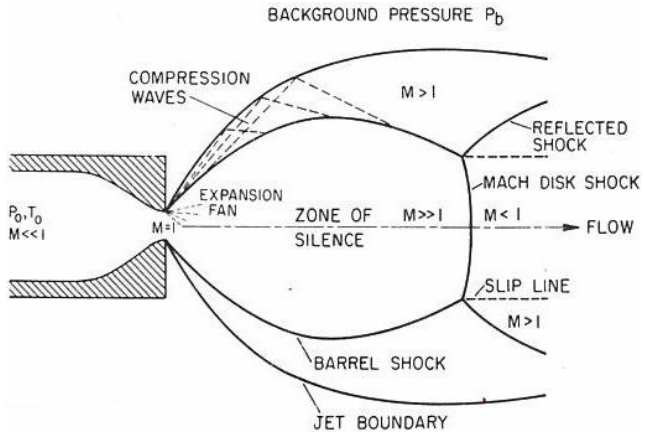

Figure 4.11: Schematic of a molecular beam expansion[57].

the atmosphere and the first pumping stage, the Mach disk location is empirically calculated to be [57]

$$\left(\frac{x_M}{d}\right) = 0.67\sqrt{\frac{P_0}{P_b}} = 0.67\sqrt{\frac{10^3}{10^{-3}}} \approx 670. \tag{4.21}$$

This means that for an orifice of for example 30 μm diameter, the position of the Mach disk will be approximately 2cm inside the vessel. Naturally the presence of skimmers inside the vessel complicate the mechanics involved in the expansion.

A cross section of the mass spectrometry setup is shown in figure 4.12. The plasma jet is shown in its normal operating position (the height may be varied). The vertical position of the orifice can be adjusted to sample within the zone of silence. A beam block is implemented to be able to block the molecular beam from reaching the mass spectrometer, allowing for background gas analysis. Both platinum and *Macor* (ceramic) orifices are used. The metal orifice has the disadvantage of drawing current, whereas measuring ions generated by the plasma using the ceramic orifice is less straightforward due to charging of the orifice and subsequent repelling of incoming ions. The pressures in the first (between the orifice and the first skimmer), second (between the two skimmers) and third (between the second skimmer and the mass spectrometer) stage, indicated by P1, P2 and P3 are typically of the order of 10^{-3}, 10^{-6} and 10^{-7} mbar respectively. This is however dependent on the used orifice and whether or not the beam block is closed.

The three stages separated by skimmers are each pumped by one *Pfeiffer HiPace 300* turbopump, which in turn are connected to two *BOC Edwards XDS10* mechanical pumps. The pressure in the first stage is measured using an *Edwards APG-L-NW16* gauge (atmosphere to 10^{-4} mbar), while the second and third stage pressures are measured using an *Edwards AIM-S-NW25* gauge (10^{-4} to 10^{-8} mbar). In order to be able to measure ions generated by the plasma, a positive or negative potential is applied to the skimmers using two *Delta Elektronica* DC power supplies. A potential of ±10 V is applied on the first skimmer and a potential of ±40 V is applied on the second skimmer. This potential results in a net force on the plasma generated ions, accelerating them to the mass spectrometer inside the supersonic expansion.

4.6 Ion chromatography

Ion chromatography is basically a conductivity measurement and it relies on the difference in interaction of various cations and anions within a separation column to make a distinction

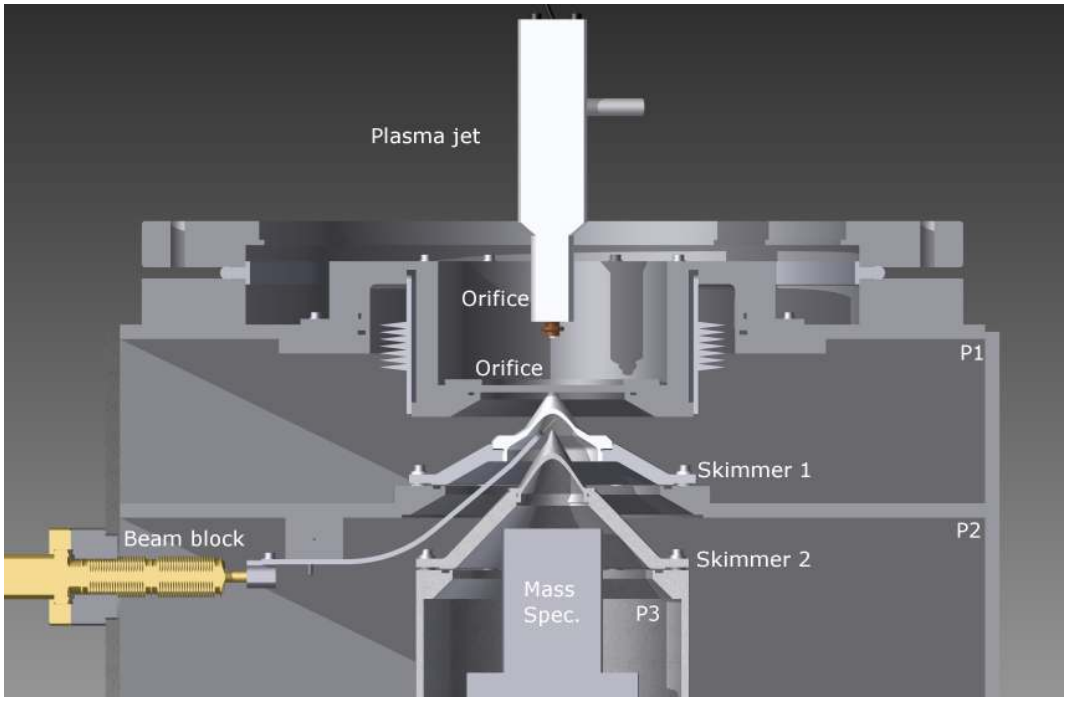

Figure 4.12: Cross section of the mass spectrometry setup in combination with the plasma jet fitted with a ring electrode. The pressures at P1, P2 and P3 are typically of the order of 10^{-3}, 10^{-6} and 10^{-7} mbar respectively, for an orifice of 28 µm diameter.

between different cations and anions. A liquid sample is added to a flow of eluent[2] after which it passes through the separation column and the conductivity of the fluid exiting the column is measured and plotted as a function of time. The result is called a chromatogram. Because different components have different interactions, the time it takes for the components to travel the length of the column is different. This allows for an identification of various anions and cations that might be present.

An example of an ion chromatogram is shown in figure 4.13. The first peak in the chromatogram is caused by the arrival of eluent at the conductivity sensor. After that two more peaks are visible, which are delayed by a time t_{s1} and t_{s2}. These two peaks represent two different ions and their area is a measure of the concentration.

The total retention time, t_{ms1} and t_{ms2} of a component in the column depends on the so-called capacity factor k, given by

$$k = D\left(\frac{V_s}{V_m}\right) \tag{4.22}$$

where V_s and V_m denote the volume of the stationary (i.e. bound to the separation column) and mobile (i.e. dissolved in eluent) phase respectively and D is the ratio of the concentration in the stationary and mobile phase:

$$D = \frac{[A]_s}{[A]_m}. \tag{4.23}$$

D is called the Nernst distribution coefficient. The total retention time of an analyte is given by

$$t_{ms} = kt_m + t_m \tag{4.24}$$

[2]Eluent is a solvent used to aid in the migration of analytes through the separation column.

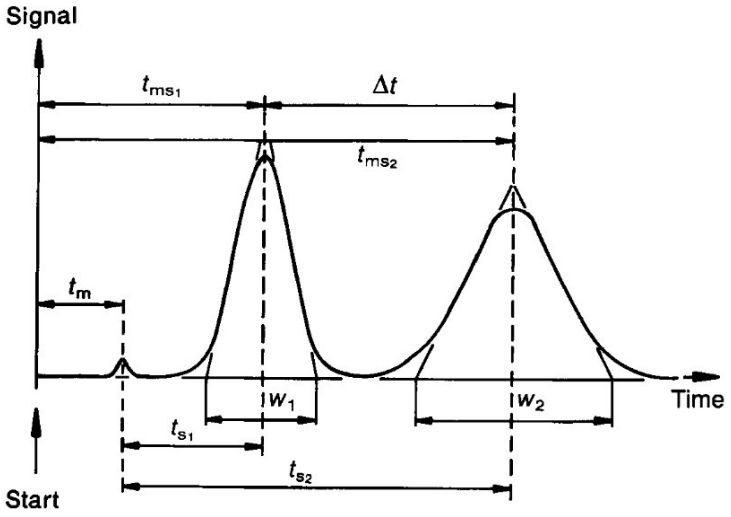

Figure 4.13: Example of an ion chromatogram.[58]

where t_m is the retention time of the eluent. The selectivity or relative retention is given by

$$\alpha = \frac{t_{s2}}{t_{s1}} = \frac{t_{ms2} - t_m}{t_{ms1} - t_m}. \tag{4.25}$$

The separation of two peaks can be expressed in terms of the resolution,

$$R_s = \frac{t_{ms2} - t_{ms1}}{2\,(\sigma_1 + \sigma_2)}, \tag{4.26}$$

where σ_1 and σ_2 are the standard deviations of the peaks. If the peaks are Gaussian, a resolution of R=2.0 is sufficient to clearly distinguish two peaks and at a minimum value of 0.5 two components can still be detected as separate peaks. The used eluent and separation column determine the capacity factor and the selectivity for the various ions as well as the obtainable resolution. Broadening of the peaks is caused by various effects. For example, different molecules of the same component can follow different paths through the column, leading to a spread in retention time.

By using samples containing known concentrations of for example chloride, nitrite and nitrate the area under the peaks can be converted to a concentration. In this work ion chromatography is used to determine the concentrations of chloride, nitrite and nitrate in distilled water which has been treated with the plasma jet.

The system used for these measurements is a *Dionex ICS-90* in combination with an autosampler. It is an isocratic system, meaning that the composition of the eluent remains the same throughout the measurement. The eluent is a mixture of sodium carbonate and sodium hydrogen carbonate and the separation column is made of packed resin. The method of ion separation is ion-exchange, making the retention time in the column dependent on Coulombic interaction with ion-exchange sites. After exiting the column, a suppressor is used to minimize the background conductivity of the eluent and thus enhancing detection of sample ions. Because of this suppression however, carbonate-, sodium and hydrogen carbonate ions can not be measured. The conductivity of the resulting solution is measured using a thermally controlled, digital conductivity meter, allowing a detection range of up to $10^5\mu$S over a fixed distance. After integrating the peaks and comparing the resulting area to calibration samples, a concentration in mg/l is obtained. This concentration is converted into mM as all other chemical concentration in this report are also in mM. Because of the sensitivity of the chromatography setup, only distilled water can be used. Significant amounts of for example chloride (saline contains approximately 0.15 mole of NaCl per liter)

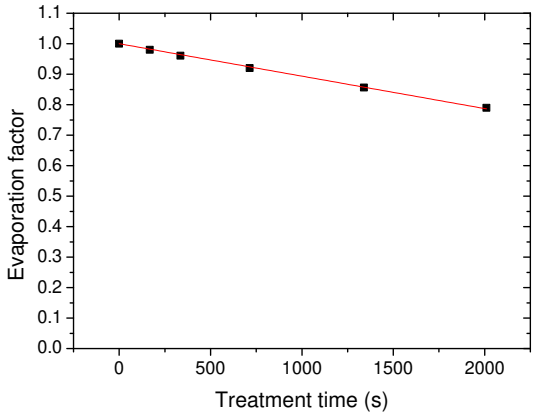

Figure 4.14: Example of evaporation factor $c_{\text{evap}}(t)$ for 3.35 ml of initial water volume as a function of treatment time for a 1.3 W ring electrode argon plasma. The shown linear fit is fixed at an initial value of 1 and its slope is approximately -1.1·10^{-4} s^{-1}.

would make measurements of nitrate and nitrite levels impossible without altering the ion chromatography system, which was used from the group TPM (Transport in Permeable Media). This was therefore not a viable option. Still, the measurements provide an insight into the plasma induced chemistry in the liquid phase.

The treatment is performed in well plates containing 12 wells with a maximum volume of 6.5 ml. A volume of 3.35ml is treated to allow for multiple chromatography runs. The treatment time is proportionally increased, making 33 minutes and 30 seconds of treatment equal to 1 minute of treatment of 100 µl which is the volume used in the biological treatments. In order to correct for increased concentrations due to evaporation of the water as a result of plasma treatment, the evaporation is determined by measuring the mass of the well plate including water before and after treatment. A time dependent evaporation factor $c_{\text{evap}}(t) = V(t)/V(t_0)$ is calculated, where $V(t)$ is the measured volume at time t and $V(t_0)$ is the initial volume. The concentrations obtained using the ion chromatography system are corrected by multiplying the found concentration with this factor. An example of an evaporation factor as a function of treatment time of a volume of 3.35 ml using an argon ring electrode plasma with a plasma power dissipation of 1.3 W is shown in figure 4.14.

4.7 Hydrogen peroxide measurements

The hydrogen peroxide concentration in distilled water after plasma treatment is determined by measuring the absorption of light emitted by a blue LED at 450 nm by a mixture of plasma treated water and ammonium metavanadate solution at a ratio of 1:1. The reaction of H_2O_2 and metavanadate in an acidic medium results in the formation of a peroxovanadium cation which produces a red-orange color with a maximum absorbance at 450 nm. By comparing the absorption to a reference mixture of non-treated distilled water and metavanadate solution, the concentration of H_2O_2 can be calculated. The transmission of the light through a substance is given by the Beer-Lambert law:

$$T = \frac{I}{I_0} = 10^{-\alpha l} = 10^{-\varepsilon l c}, \tag{4.27}$$

where I is the measured intensity, I_0 is the reference intensity, α is the absorption coefficient, l is the optical path length, ε is the molar absorptivity and c is the concentration of absorbing species. The molar absorptivity of H_2O_2 using this method is 283 $mol^{-1}Lcm^{-1}$[59] and the optical path length used in the absorption setup is 27 mm. The concentration is calculated

Figure 4.15: Example of an agar plate covered with bacteria (opaque) with a 12mm diameter area cleared of bacteria in the center.

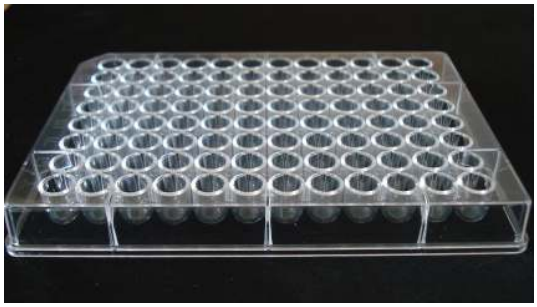

Figure 4.16: Example of a 96-well microtiter plate. A well has a typical diameter of 6.7 mm. Source: con-rem.com.

using

$$c = -\frac{\log\left(\frac{I}{I_0}\right)}{\varepsilon l}. \tag{4.28}$$

The measured concentrations are displayed in mmolL^{-1} because of their low values and are corrected for evaporation, which is again linear as a function of time, using the same method discussed in section 4.6. The treatment volume was 3.8 ml and the resulting slope of the evaporation factor was found to be -0.9·10^{-4} s^{-1}, which is similar to the slope of -1.1·10^{-4} s^{-1} found in the ion chromatography diagnostics discussed in the previous section.

4.8 Biological treatment methods and characterization

For the treatment of samples at Beverwijk, an identical plasma jet is used as discussed in section 4.1 . This allows for a comparison between treatment results in Beverwijk and diagnostics performed in Eindhoven. For treating bacteria, 96-well microtiter plates as well as agar plates are used. A 96-well microtiter plate consists of 96 wells with a well volume of approximately 360 µl. An agar plate is a petri dish with a layer of agar, a jelly like substance which contains Luria Broth (LB) to provide nutrients for the bacteria to grow. LB contains among others peptides, vitamins and minerals. In the case of a well plate the broth is added in liquid form. An example of an agar plate covered with bacteria (opaque) in which a 12 mm diameter area is cleared of bacteria is shown in figure 4.15. An example of a 96-well microtiter plate which is used in this study is shown in figure 4.16.

Pseudomonas aeruginosa is cultured in Luria Broth after which it is diluted and the

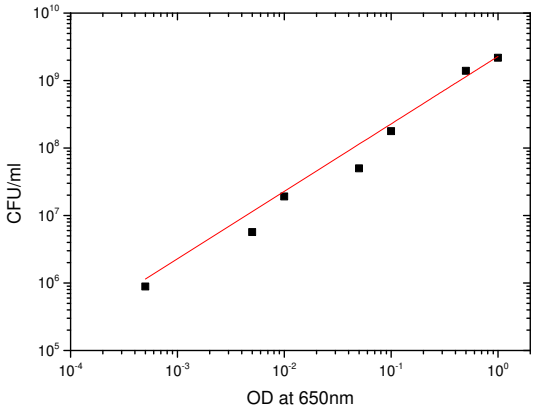

Figure 4.17: Bacterial concentration as a function of measured optical density at 650nm. The shown linear fit intersects at at zero and has a slope of approximately $2.3{\cdot}10^9$ CFU/ml.

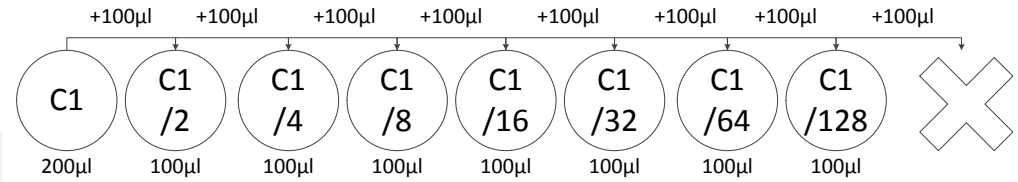

Figure 4.18: Schematic representation of a two-fold serial dilution. Every well except the leftmost contains 100 µl of solution without bacteria. The first well contains 200 µl of solution containing bacteria of which 100 µl is transferred to the next well, etcetera. In the end every well contains 100 µl of solution and the left-over 100 µl is discarded.

optical density at 650nm is measured and corrected for the optical density of the medium and fluid container itself, making it a relative optical density measurement. This method is calibrated by measuring the optical density of a sample, after which it is diluted to a suitable value, plated on agar plates and incubated for 24 hours. Afterwards the amount of colonies is counted which results in an accurate value for the initial bacterial concentration. An OD value of 1 is found to correspond to approximately $2 \cdot 10^9$ CFU/ml and it scales approximately linearly with bacterial concentration as is seen in figure 4.17. After the optical density measurement a further dilution is performed to achieve the desired concentrations for treatment. A serial dilution and consecutive plating on agar is used to verify the bacterial density acquired by optical density measurements.

The 96-well plates are filled with a total of 100 µl of solution to ensure a constant fluid level and treatment volume. A dilution is performed per column of 8 wells by serial dilution. As an example a two-fold serial dilution method is discussed. In this process the first well contains 200 µl of the highest desired bacterial concentration whereas the 7 other wells contain 100 µl of solution without bacteria. From the top well, 100 µl is pipetted in the next well, mixed thoroughly and from the resulting diluted solution (200 µl), 100 µl is transferred to the next well, etcetera. In the end the left-over 100 µl is discarded. This process is shown schematically in figure 4.18. The resulting concentration in the wells is shown as a function of the concentration in the first well. The bacteria are treated in distilled water, saline (approximately 9 g/l of NaCl), phosphate buffered saline (PBS, 0.2 g/l KCl, 0.2 g/l KH_2PO_4, 8 g/l and 2.16 g/l Na_2HPO_4-$7H_2O$), sodium acetate solution and luria broth.

Lastly, the effect of plasma treatment on keratinocytes and fibroblasts is determined by measuring the amount of lactate dehydrogenase (LDH) in the liquid after treatment. LDH

is an enzyme which is present in many organisms, including humans. When (partial) lysis[3] occurs, LDH is released into the liquid. A *Promega CytoTox 96* kit is used to measure LDH content in the liquid by conversion of INT tetrazolium salt into red formazan. The optical density recorded of treated cell solutions is compared to total chemical lysis to obtain a fraction of total cell lysis due to plasma treatment.

While the method explained in the previous paragraph focuses on cell death, it is also possible to determine cell viability by using a so-called tetrazolium dye MTT[4] assay. This assay depends on the ability of the still viable cells in the sample to metabolize tetrazolium salt (MTT, which is water-soluble) into insoluble formazan[60]. This process occurs due to reduction of the salt via dehydrogenases and reductases[61]. The treated cells are incubated with MTT for two hours, after which DMSO[5] is used to dissolve the formed formazan. Lastly the optical density is measured at 560 nm, which is directly related to the amount of viable cells in the sample (more dissolved formazan results in a higher optical density). By comparing treated samples with untreated control samples a normalized cell viability value is obtained.

[3]Compromise of cell integrity resulting in a release of cell content.
[4]3-4,5 dimethylthiazol-2,5 diphenyl tetrazolium bromide
[5]Dimethyl sulfoxide

Chapter 5

Diagnostic results

This chapter shows obtained measurement results of plasma dissipated power and gas temperature, absolute UV emission, ion fluxes, as well as plasma induced nitrite, nitrate and hydrogen peroxide concentrations in plasma treated water. The measurement methods and the used setup were previously introduced in chapter 4. Some of these measurements are performed for a variety of settings whereas other measurements are only performed using settings mostly used in the treatment of biological samples presented in chapter 6.

Figure 5.1 shows an argon plasma jet using a ring electrode at various plasma power dissipations. The length of the plasma jet is seen to increase when increasing the amount of power dissipation, and a transition from a diffuse looking to a more filamentary plasma state is visible between 1.4 and 2.1 W.

5.1 Power measurements

Using the power measurement method discussed in section 4.2, the power dissipated in the plasma is determined for various conditions and for both the plate and ring electrode geometries. Note that as stated before, the voltage and current are measured between the power supply and matching circuit. As a result, all waveforms shown in this chapter show the behavior of the system consisting of both the matching circuit and the plasma source.

In figure 5.2, the voltage and current waveforms are shown for the ring and plate electrode geometries for both argon and helium at a constant current of approximately 0.56 A RMS. The waveforms are corrected for the phase shift caused by the voltage- and current probes. The current is shown in blue for both argon and helium. Both current waveforms are presented in such a way that they overlap. A clear difference in phase shift between the helium and argon plasma can be seen; the plate electrode shows a more capacitive (i.e.

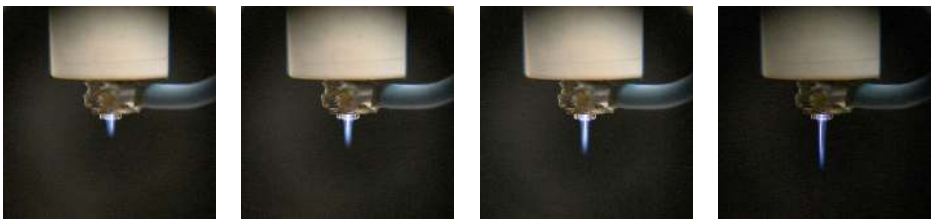

(a) 0.4 W (b) 1.1 W (c) 1.4 W (d) 2.1 W

Figure 5.1: Photos of an argon plasma generated using the ring electrode at various plasma dissipated powers. A duty cycle of 20% and a mass flow of 1.5 slm was used. At a power dissipation of 2.1 W a shorter exposure time was used to avoid saturation of the camera.

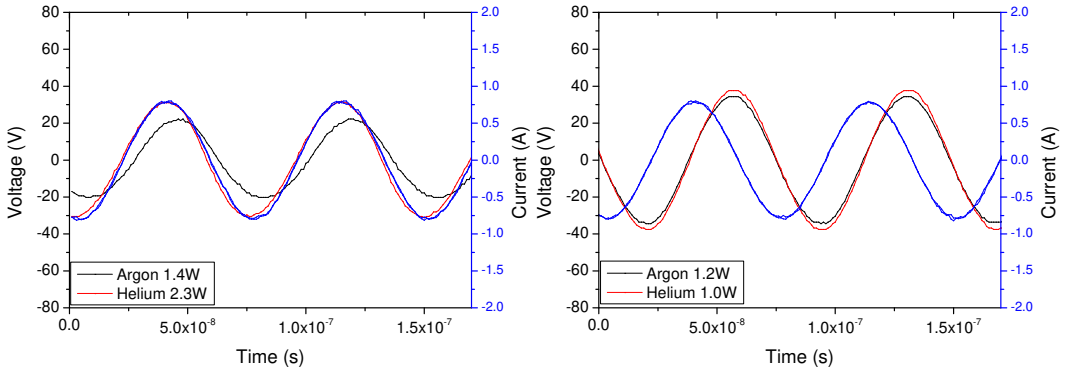

(a) Ring electrode, 20% duty cycle

(b) Plate electrode, continuous

Figure 5.2: Voltage and current waveforms for the ring and plate electrode operating on both helium and argon at a current of ∼0.56A RMS. The current is shown in blue for both argon and helium. The argon and helium voltage waveforms are shown in black and red respectively. The power shown in the legend is the resulting time averaged plasma dissipated power.

approximately 90 degree phase shift) behavior than the ring electrode. Especially when using helium, the system is prone to a resistive behavior (approximately 0 degree phase shift). The differences between the ring electrode and plate electrode are mainly due to the fact that the geometry changes the electric field configuration (cross-field versus linear field). This geometry difference leads to a different impedance of the plasma, which in turn changes the observed phase shift. The difference between helium and argon in the case of the ring electrode geometry is explained at a later point in this section.

The plasma dissipated power as a function of RMS current for both the plate and ring electrode geometry for a flow of 1.5 slm of both argon and helium with varying percentages of added air is shown in figure 5.3. Using the ring electrode to produce an argon plasma, the average plasma dissipated power shows an almost step-like behavior for all added percentages of air in which the dissipated power suddenly increases. The current at which this step occurs depends on the percentage of added air. At approximately 800mA all percentages of added air result in the same power dissipation for the same current. The plate electrode in the case of argon shows an approximately linear behavior. Helium on the other hand shows an almost linear relationship between plasma dissipated power and RMS current in the case of a ring electrode geometry, whereas the plate electrode leads to a more quadratic-like behavior.

For two RMS current values the voltage and current waveforms are shown for 0% and 3% of added air in figure 5.4. When looking at the waveforms it can be concluded that the sudden increase in power dissipation is due to a shift from a capacitive behavior to a resistive and eventually even inductive behavior which is caused by a change in impedance of the plasma. Note that the phase and impedance of both the matching circuit and the plasma itself are measured. The plasma itself does not become inductive. A possible explanation for this effect is that at low powers the argon plasma is only located around the tip of the needle where the electric field is sufficient to ignite the plasma, whereas at higher powers a larger part of the channel is filled with plasma. This leads to a change in capacity of the plasma and therefore a more dominant inductive effect originating from the coil in the matching circuit. The same effect has been observed before by for example Yanguas-Gil et al.[62], Benedikt et al.[63] and Focke[64]. When using helium the plasma visually fills the entire channel. This also explains the resistive behavior of helium in figure 5.2a; whereas argon shifts to a resistive behavior only at relatively high currents, a helium jet already shows this behavior at the lowest discharge currents. The linear behavior of argon versus the quadratic-like

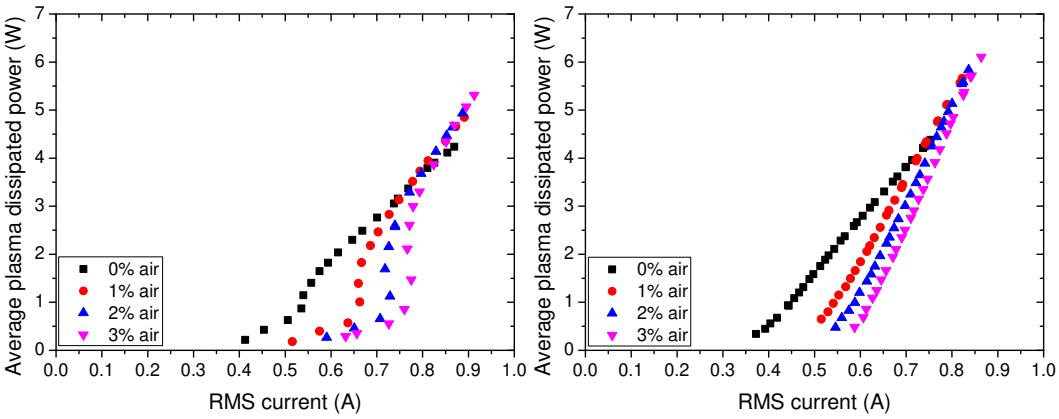

(a) Ring electrode argon, 20% duty cycle

(b) Ring electrode helium, 20% duty cycle

(c) Plate electrode argon, continuous

(d) Plate electrode helium, continuous

Figure 5.3: Average plasma dissipated power as a function of RMS current for the two different electrode geometries, two different carrier gases (at 1.5slm) and different percentages of added air.

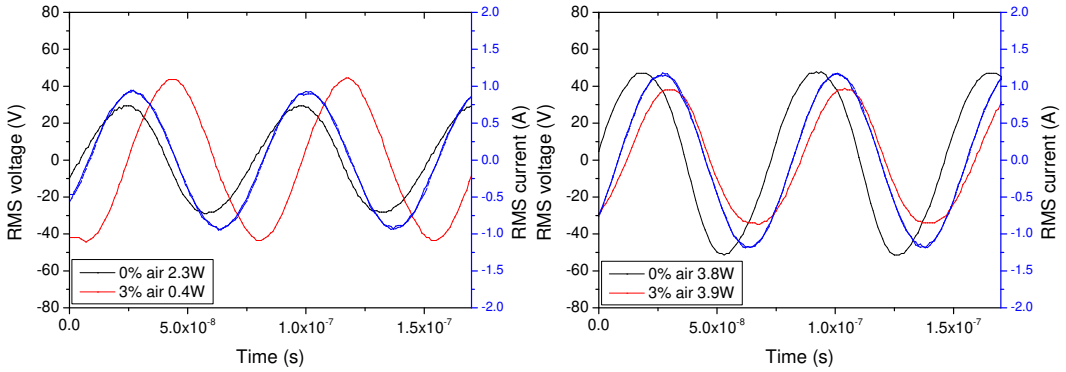

(a) ∼0.65A RMS (b) ∼0.80A RMS

Figure 5.4: Voltage and current waveforms of a 1.5 slm argon plasma generated using the ring electrode at two different RMS current values and a duty cycle of 20%. The current is shown in blue for both 0% and 3% of added air.

behavior of helium using the plate electrode geometry as shown in figure 4.3 and 5.3 is due to a difference in plasma volume as previously observed by Hofmann et al.[49]. Whereas an argon plasma generated using the plate electrode shows an approximately constant plasma volume, in helium the plasma volume increases as a function of discharge current. As a result the power density dissipated in the plasma is approximately constant for both cases but needs to increase faster than linear for helium.

Further investigation into the effect of RMS discharge current on the phase shift difference between voltage and current is shown in figure 5.5, where the phase shift is shown as a function of RMS current for the ring electrode geometry. Again, the phase shift measured is corrected for the phase shift induced by the measurement probes. In the case of an argon plasma a threshold current is observed, which is dependent on the percentage of added air, at which there is a sharp gradient in the phase shift angle. At low currents the system reacts capacitively, whereas at a high current the system changes into an inductive state. While the decreasing trend in phase shift is also visible in the case of a helium plasma, the gradient is smaller, leading to a more gradual increase in plasma dissipated power, as is also demonstrated in figure 5.3b.

When using the plate electrode the phase shift between voltage and current changes considerably less, ranging from approximately 90 degrees at low currents to 80 degrees at high currents. The behavior is similar in both argon and helium and is shown in figure 5.6.

It can be concluded that when helium is used as a carrier gas the increase in power dissipation is mostly due to an increase of voltage and current, whereas in the case of argon the changing phase shift also contributes to the increasing power dissipation.

5.2 Gas temperature measurements

Figure 5.7a and 5.7b show the dependency of the gas temperature downstream of the plasma on gas flow rates and duty cycles for an argon plasma generated using the plate electrode obtained with a thermocouple. Increasing the gas flow, as well as decreasing the duty cycle (resulting in shorter pulses) lowers the gas temperature. In figure 5.7c and 5.7d, the same effects of increasing the gas flow and decreasing the duty cycle are shown for helium. The same effect is observed. The main difference between argon and helium however is the absolute temperature; the difference between the temperatures shown in these graphs is more than 100 K.

Gas temperature profiles downstream of the plasma plume at various time averaged

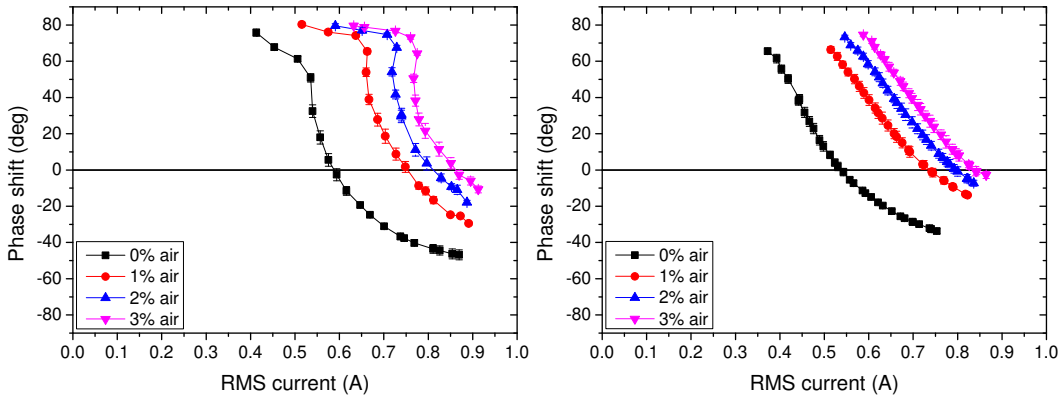

(a) Argon (b) Helium

Figure 5.5: Phase shift between voltage and current for a ring electrode helium and argon plasma as a function of RMS current for various percentages air added to a 1.5 slm gas flow. Phase shifts are corrected for additional phase shift due to measurement probes. Error bars show standard deviation over 138 RF periods.

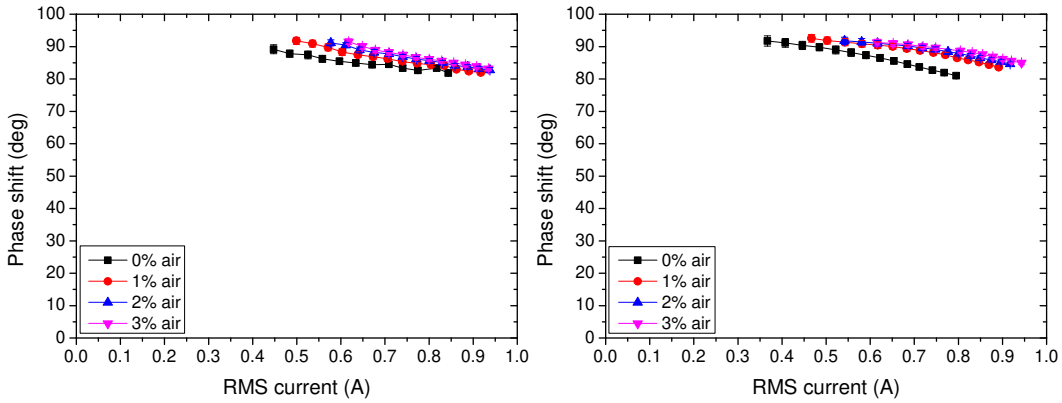

(a) Argon (b) Helium

Figure 5.6: Phase shift between voltage and current for a plate electrode helium and argon plasma as a function of RMS current for various percentages air added to a 1.5 slm gas flow. Phase shifts are corrected for additional phase shift due to measurement probes. Error bars show standard deviation over 138 RF periods.

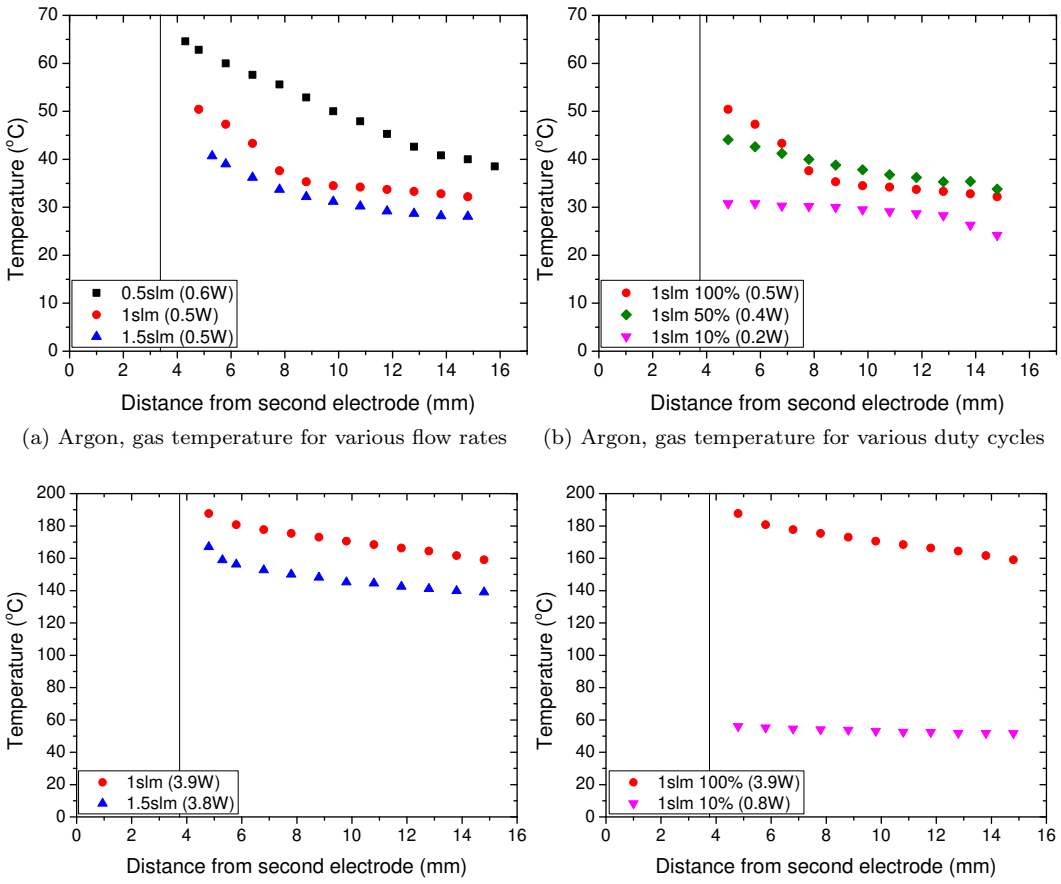

(a) Argon, gas temperature for various flow rates

(b) Argon, gas temperature for various duty cycles

(c) Helium, gas temperature for various flow rates

(d) Helium, gas temperature for various duty cycles

Figure 5.7: Temperature profile measured using a thermocouple as a function of the distance from the second electrode using the plate electrode. The approximate position of the visible plasma tip is indicated with a black line. Note the difference in scale between the helium and argon results.

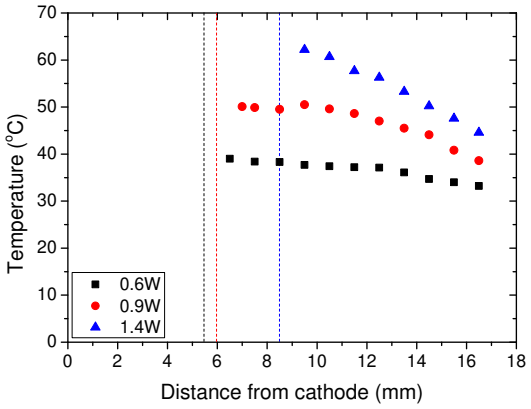

Figure 5.8: Temperature profiles measured using a thermocouple as a function of the distance from the cathode using an argon ring electrode plasma. A flow of 1.5 slm and duty cycle of 20% was used. The approximate position of the visible plasma tip is indicated with dashed lines in the corresponding colors.

plasma dissipated powers of a 1.5 slm argon plasma generated using the ring electrode are shown in figure 5.8. A 20% duty cycle was used. Because as a result of increasing the power, the plasma plume length also increases, the first measurement point of the three different series are at various distances from the cathode. Increasing the power dissipation increases the gas temperature close to the tip of the plasma plume, but when the distance from the tip of the plume is increased, the differences in temperature are smaller.

To get an estimate of the effect of gas flow on gas temperature, a power balance of the plasma can be used, assuming all of the plasma dissipated power is converted into heat which is transported by the gas flow. This means that radial thermal losses are neglected and all temperatures obtained using the calculation should be treated as upper limits. The dissipated power can be used to calculate the temperature difference by

$$P_{diss} = \frac{\Delta m}{\Delta t} c \Delta T \rightarrow \Delta T = \frac{P_{diss} \Delta t}{c \Delta m}. \tag{5.1}$$

Using the heat capacity $c = 520$ Jkg^{-1}K^{-1} of argon, a plasma dissipated power of $P_{diss} = 0.5$W and a varying flow of $\Delta m/\Delta t$ in kg/s, an estimate can be made of the change in gas temperature as a function of gas flow. A flow of 0.5, 1 and 1.5 slm at a plasma dissipated power of 0.5 W leads to values of ΔT of approximately 69, 35 and 23 K respectively. Pulsing the plasma leads to an approximately proportional decrease in time averaged plasma dissipated power, which in turn decreases gas heating, as this scales linearly. Increasing the power at a fixed flow of 1.5 slm of argon leads to values of 28 K for 0.6 W, 41 K for 0.9 W and 64 K for 1.4 W.

Helium on the other hand has a much larger heat capacity of $c = 5193$ Jkg^{-1}K^{-1} but it needs higher plasma dissipated powers to operate. This consequently leads to higher gas temperatures. For a plasma dissipated power of 3.9 W and a gas flow of 1.5 slm the maximum temperature difference is calculated to be 178K, while for a gas flow of 1 and 0.5 slm the ΔT values are 267 and 533 K respectively. Using pulsed RF signals again reduces the gas temperature. A 10% duty cycle results in a time averaged plasma dissipated power of 0.8 W, which at a flow of 1 slm yields a gas temperature difference between incoming and outgoing gas flow (ΔT) of 55 K.

When comparing the calculated maximum temperature differences and assuming the gas is initially at room temperature, a comparison is possible between the measurements and the calculations. The calculations show a good agreement with the measured values shown in figures 5.7 and 5.8, the overestimation however does increase at higher temperatures. This leads to a bigger discrepancy in the case of helium.

Another important difference between helium and argon is their thermal conductivities, which are $15{\cdot}10^{-2}$ $\mathrm{Wm^{-1}K^{-1}}$ and $18{\cdot}10^{-3}$ $\mathrm{Wm^{-1}K^{-1}}$ respectively. Using Fourier's law

$$\vec{q} = -k\nabla T, \tag{5.2}$$

where $\vec{q}$ is the local heat flux in $\mathrm{Wm^{-2}}$, k is the thermal conductivity in $\mathrm{Wm^{-1}K^{-1}}$ and ∇T is the temperature gradient in $\mathrm{Km^{-1}}$. It is clear that a low thermal conductivity results in a larger temperature gradient than a high thermal conductivity, provided the local heat flux is the same. As a result, an argon plasma will generally have a steeper temperature decline in the effluent than a helium plasma. This effect is easily noticed when physically comparing the effluent with both gas types; a comparable helium plasma feels hotter to the touch. This is an important reason why argon is preferred over helium as a carrier gas in clinical applications of plasma treatment. A second reason is that due to the higher heat capacity of helium more energy is stored in the gas.

It has to be kept in mind that these calculations assume that all of the plasma dissipated power is used to increase the gas temperature. In helium most of the dissipated power is used for heating but for argon this is not the case. As a result the actual gas temperatures in argon are generally significantly lower. Also, the radial losses are neglected which is in practice also an important loss factor.

Combined optical emission spectroscopy and thermocouple measurements using the ring electrode are shown in figure 5.9. Both axial and radial temperature profiles are shown for a constant power dissipation (∼0.6 W) for two different percentages of added air, 0% and 0.5%. Also a radial comparison between the two percentages is shown. The radial profiles do not change significantly over a distance of approximately 3 mm. Adding 0.5% air at constant power increases the temperature in the plasma from approximately 350 K to 400 K. The dip in the central part of the radial profile was later confirmed to be a measurement anomaly, not an actual physical phenomenon.

Temperature profiles of plasma conditions used in treatment of biological samples are shown in figure 5.10. Because of the higher plasma dissipated power, the measured gas temperature are consequently higher than those shown in figure 5.9. Also a clear difference is seen in the distance over which the gas temperature is constant: without adding air the gas temperature profile remains at the same temperature over a longer distance, this is directly related to the visual length of the plasma plume. The difference in temperature in the case of 1%, 2% and 3% of added air is small, while the gas temperature of the plasma without air addition is seen to be higher. A power dissipation of 3.8 W leads to a maximum temperature difference of 174 K in pure argon using equation 5.1. Assuming an inflow temperature of 20°C, a temperature of 194°C is expected in the effluent. The values obtained by this calculation are slightly lower than those presented in the figure, indicating that optical emission spectroscopy measurements show an overestimate of the gas temperature, as shown before by Hofmann et al.[49]. An explanation for the fact that adding air in figure 5.9 results in an increase in temperature whereas in figure 5.10 it results in a decrease in temperature might be caused by a different operating regime due to a significantly different power dissipation.

While an Abel inversion can provide additional insight in the exact radial gas temperature distribution, in this case an Abel inversion is not possible due to the asymmetry of the discharge.

5.3 Absolute UV-flux measurements

The absolute UV-flux emitted by the plasma source is measured for both the plate and ring secondary electrode geometries and various discharge powers. The integrated irradiance (or radiant flux density) in $\mathrm{W/m^2}$ is calculated for the UVA (315-400 nm), UVB (280-315 nm) and part of the UVC range (200-280 nm). An overview spectrum from 200 to 400 nm is presented in which spectra of various concentrations of added air at constant plasma

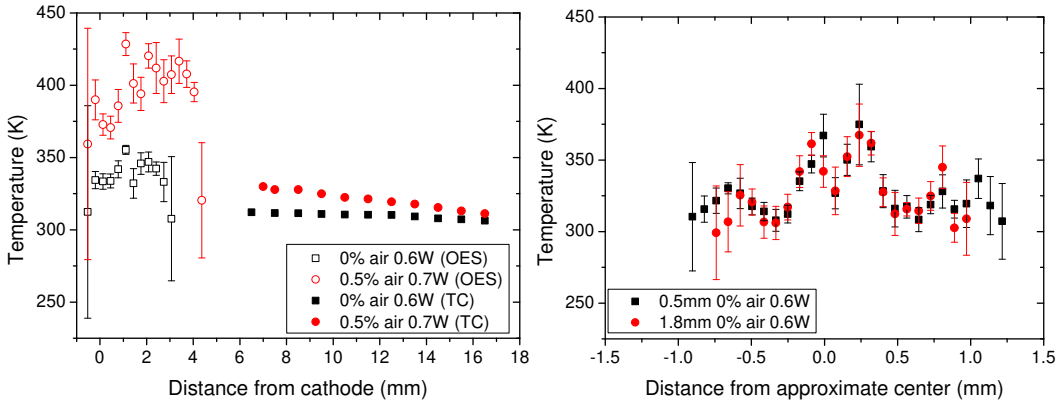

(a) Axial OES (outline symbols) and thermocouple measurements (filled symbols).

(b) Radial OES measurements with 0% added air.

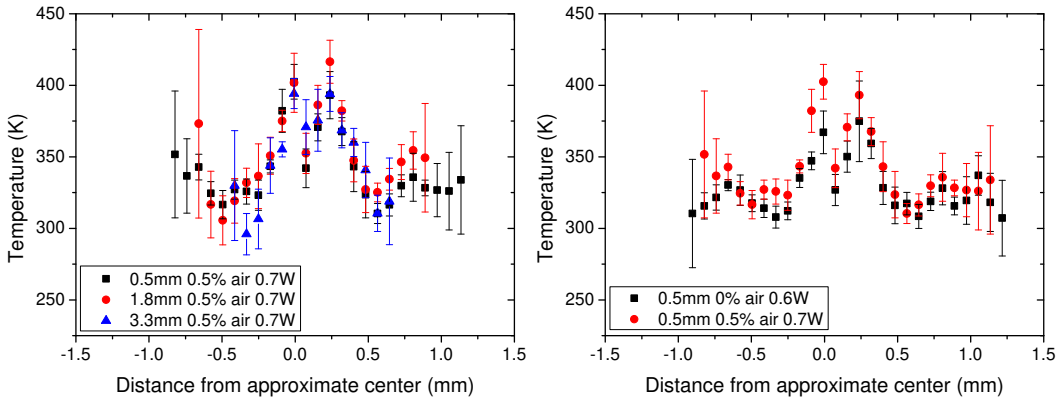

(c) Radial OES measurements with 0.5% added air.

(d) Comparison of radial OES measurements for both 0% and 0.5% air.

Figure 5.9: Axial and radial gas temperature profiles measured using optical emission spectroscopy in a 1.5 slm argon plasma using the ring electrode at a duty cycle of 20% combined with thermocouple measurements downstream. The legend in the radial profiles shows the distance from the cathode.

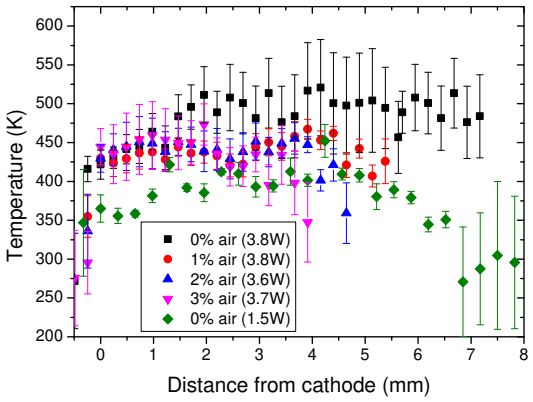

Figure 5.10: Axial gas temperature profiles measured using optical emission spectroscopy in a 1.5 slm argon plasma using the ring electrode at a duty cycle of 20%.

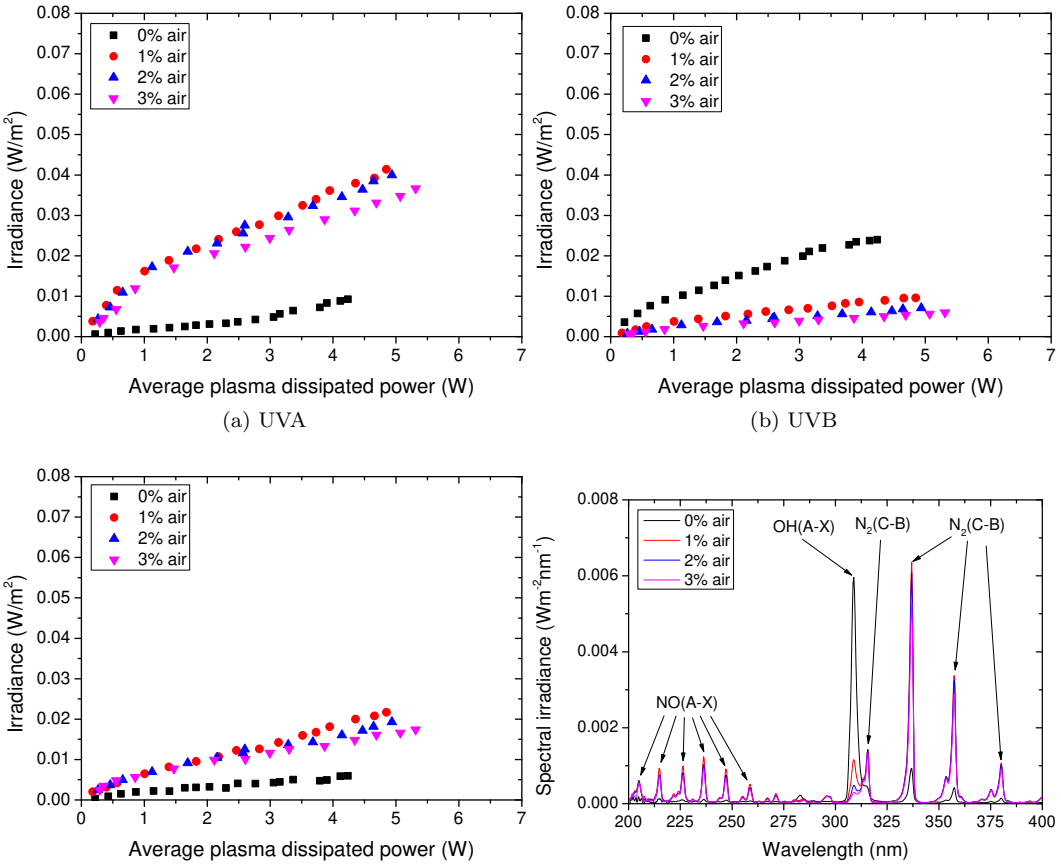

(a) UVA (b) UVB

(c) UVC (200-280 nm) (d) UV spectrum at ∼3.7 W

Figure 5.11: UVA, UVB, UVC and UV-range spectra as a function of average plasma dissipated power for various percentages of added air for 1.5 slm argon using the ring electrode at a 20% duty cycle.

power dissipations are shown. The transitions responsible for the most prominent lines are indicated in the graphs.

The absolute UV emission of a ring electrode 1.5 slm argon discharge as a function of plasma dissipated power is shown for various percentages of added air in figure 5.11. Adding air results in a higher emission in the UVA and UVC range for all powers, while a reduction in UVB occurs. When adding 3% or more of air, all measured values are lower. All UV ranges increase as a function of average plasma dissipated power. It is clearly seen that the decrease in UVB after adding air is due to a decreasing OH (A-X) (309nm) emission whereas the increase in UVA and UVC is caused by an increase in intensity of N_2 (C-B) and NO (A-X) respectively.

Figure 5.12 shows the irradiance of UVA, UVB and UVC in a 1.5 slm ring electrode argon plasma as a function of percentage of added air at a constant plasma power dissipation of 3.7 W. As stated before the influence of a decrease in OH (A-X) intensity by adding air results in a lower UVB power density, whereas the increase in N_2 (C-B) and NO (A-X) result in higher UVA and UVC power densities. The optimum of UVA and UVC power density is seen to be at approximately 1% of added air.

Figures 5.13, 5.14 and 5.15 show the same plots as in figure 5.11 for a ring electrode plasma operating on helium, a plate electrode plasma operating on argon and a plate electrode plasma operating on helium respectively. Operating the ring electrode plasma jet on

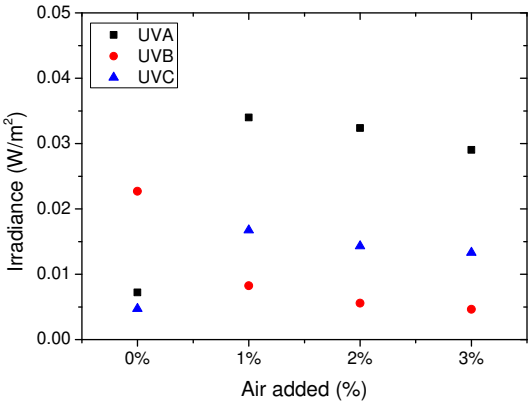

Figure 5.12: UVA, UVB and UVC measurements as a function of added air percentage for a constant average power dissipation of 3.7 W for 1.5 slm argon using the ring electrode at a 20% duty cycle.

helium results in the same trends in UVA and UVC power densities as using argon, but the overall values are lower. Also, where there is a sharp decrease in UVB by adding air to an argon plasma, this is not the case for helium due to the formation of a peak of N_2(C-B) at 296 nm. Also, contrary to the case of an argon discharge, both the ring electrode and plate electrode geometry show a vibrational band at 391 nm when the plasma is operating in helium, resulting from the N_2^+ (B-X) transition. The reason for this difference is that in helium N_2^+(B) is formed by Penning ionization

$$\mathrm{He_m} + \mathrm{N_2} \rightarrow \mathrm{N_2^+\,(B)} + \mathrm{e} + \mathrm{He}, \tag{5.3}$$

or charge exchange

$$\mathrm{He^+} + \mathrm{N_2} \rightarrow \mathrm{N_2^+\,(B)} + \mathrm{He}. \tag{5.4}$$

In argon on the other hand, the predominant mechanism is

$$\mathrm{Ar_m} + \mathrm{N_2} \rightarrow \mathrm{N_2\,(C)} + \mathrm{Ar}. \tag{5.5}$$

which leads to dominant emission of N_2(C-B).

Overall the highest UV intensity is generated using the plate electrode configuration with an argon carrier gas, as shown in figure 5.14. This leads to values of approximately 0.1 W/m^2 of total UV power density.

5.4 Mass spectrometry

Measurements of ions originating from the plasma were performed by shutting down the ionization source of the mass spectrometer. By applying a positive or negative potential to the skimmers, negative or positive ions can be measured respectively. A ring electrode plasma was used at a flow of 1.4 slm of argon and potential of ±10 V and ±40 V was applied to the first and second skimmer respectively. A platinum orifice with a diameter of 28 µm was used. As measuring positive and negative ions require different operational settings for the mass spectrometer, the amount of counts are not directly comparable. As such only the relative intensities within a spectrum should be taken into account when analyzing the spectra, not the absolute intensities.

When the plasma touches the orifice a vast amount of different positive ions are measured, as is shown in figure 5.16a. Ions such as atomic oxygen, OH^+, NO^+ and cluster ions such as $NO^+(H_2O)_n$, $H_2O^+(H_2O)_n$, $HNO^+(H_2O)_n$ and $H_3O^+(H_2O)_n$ are visible. These

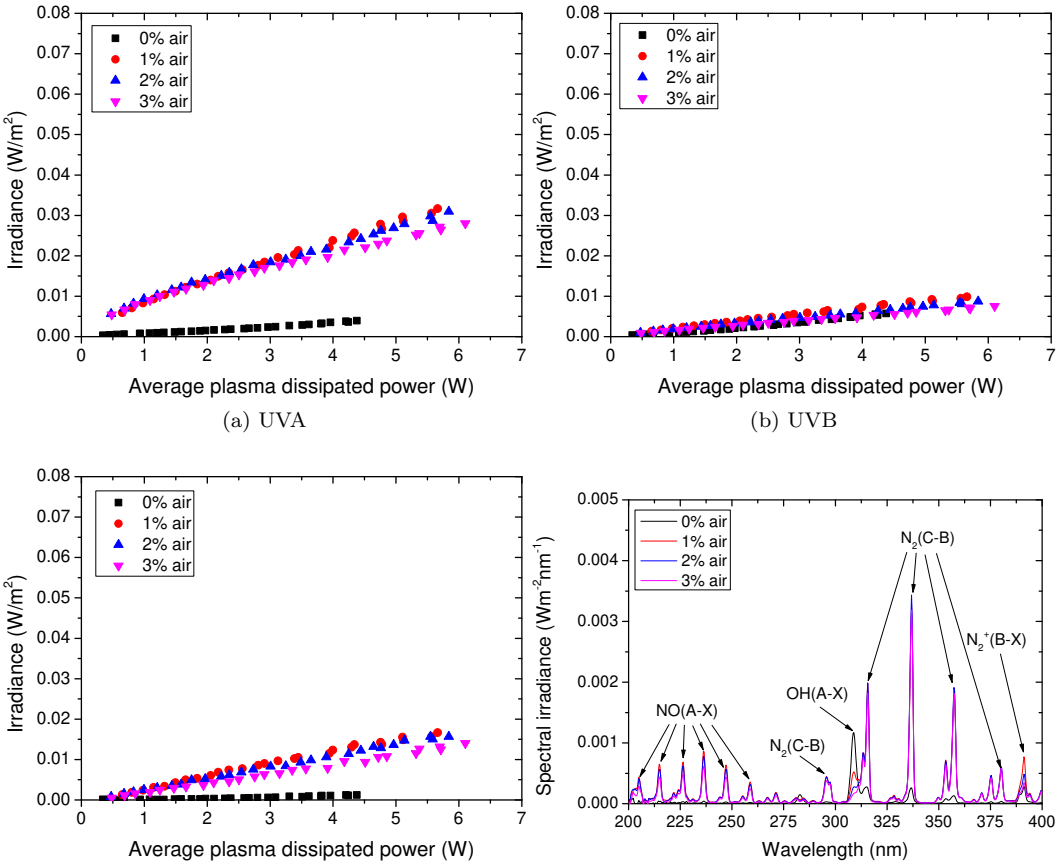

(a) UVA (b) UVB

(c) UVC (200-280 nm) (d) UV spectrum at ∼3.9 W

Figure 5.13: UVA, UVB, UVC and UV-range spectra as a function of average plasma dissipated power for various percentages of added air for 1.5 slm helium using the ring electrode at a 20% duty cycle.

clusters are clearly distinguished because of the periodicity of the peaks, showing 18 amu difference between peaks (the mass of water). Note that the most dominant peak, Ar^+, is not completely shown in the graph. Its maximum is $2.7 \cdot 10^5$ counts. The graph is scaled this way to allow for the less dominant peaks to be easily viewed as well. Apart from Ar^+, Ar^{2+} is visible, as well as Ar_2^+, ArH^+ and Ar_2H^+.

Ar_2^+ is formed by a reaction of an argon ion with two argon atoms via [65]

$$Ar^+ + 2Ar \rightarrow Ar_2^+ + Ar, \tag{5.6}$$

which is a fast process at atmospheric pressure. Note that because of this, Ar_2^+ rather than Ar^+ is expected to be the dominant ion in the discharge. The fact that it is not measured as such is possibly due to the production of Ar^+ very close to or inside the orifice.

For the formation of ArH^+, [66]

$$Ar^+ + H_2O \rightarrow ArH^+ + OH \tag{5.7}$$

which occurs simultaneously with

$$Ar^+ + H_2O \rightarrow H_2O^+ + Ar. \tag{5.8}$$

NO_2 is formed by either of the following reactions [67]:

$$O^- + NO \rightarrow NO_2 + e^- \tag{5.9}$$

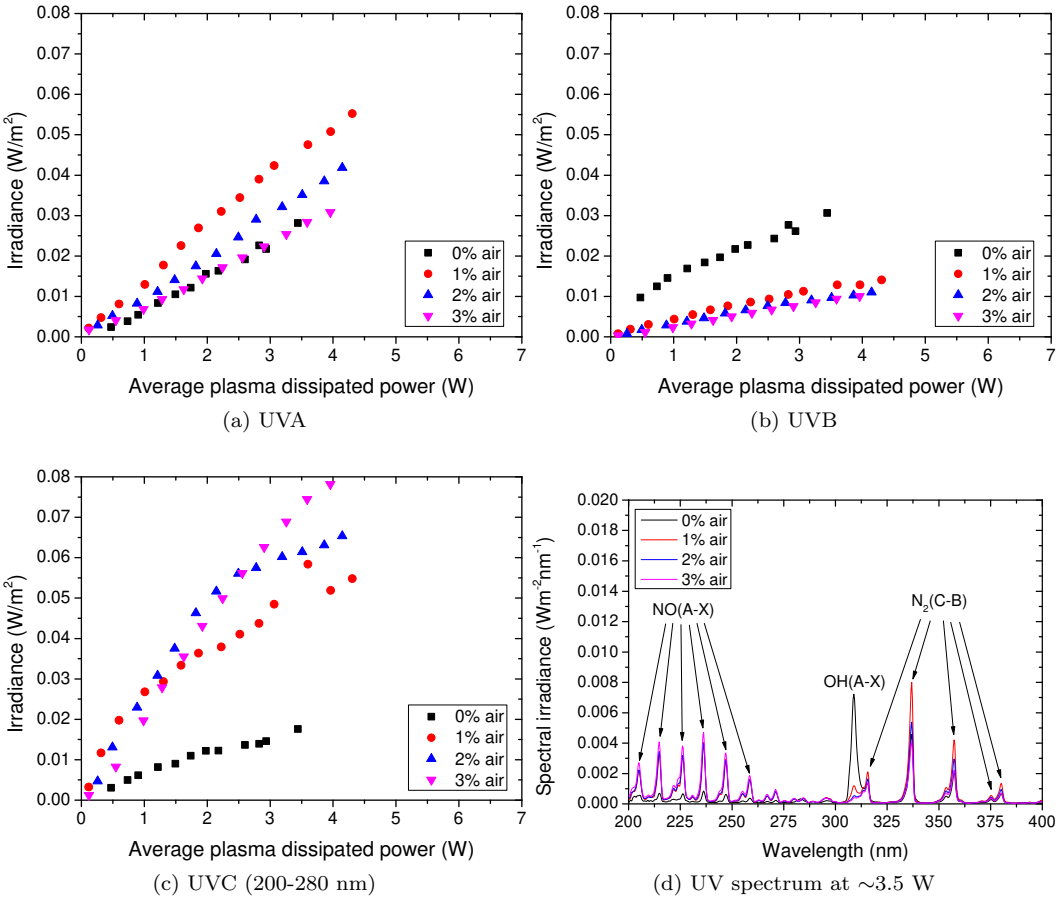

(a) UVA (b) UVB

(c) UVC (200-280 nm) (d) UV spectrum at ∼3.5 W

Figure 5.14: UVA, UVB, UVC and UV-range spectra as a function of average plasma dissipated power for various percentages of added air for 1.5slm argon using the plate electrode at a 100% duty cycle.

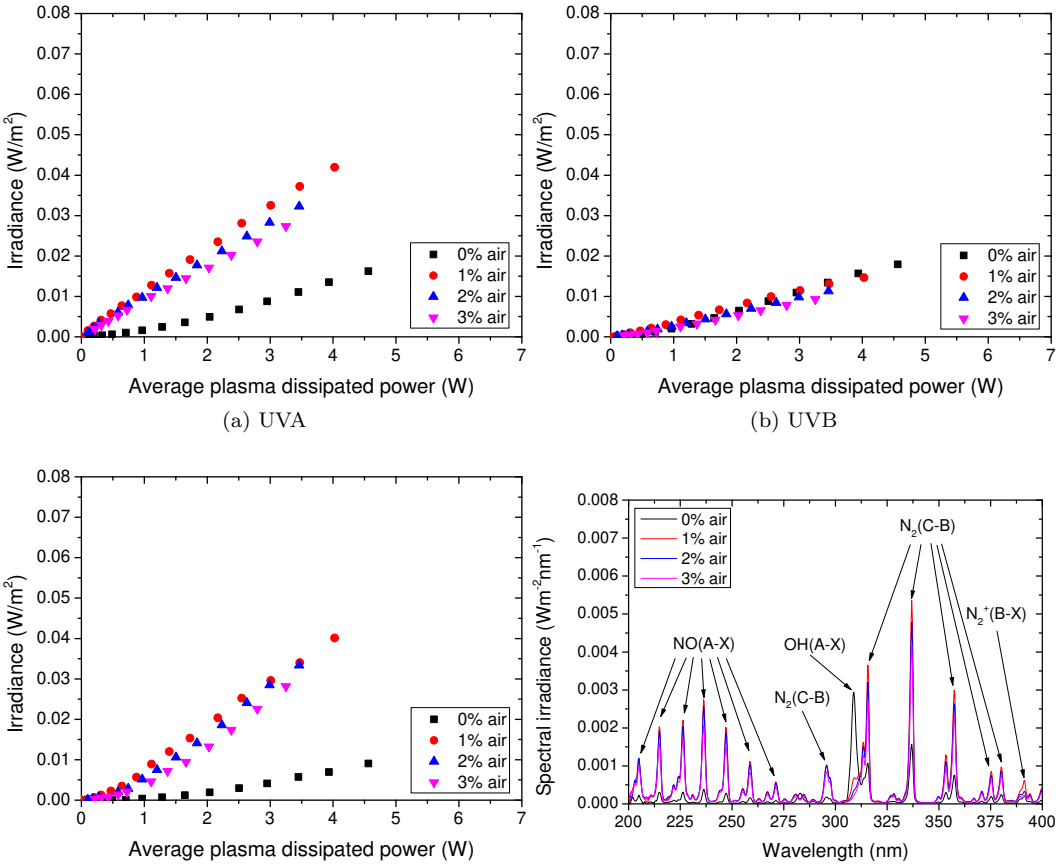

(a) UVA (b) UVB

(c) UVC (200-280 nm) (d) UV spectrum at ∼3.5 W

Figure 5.15: UVA, UVB, UVC and UV-range spectra as a function of average plasma dissipated power for various percentages of added air for 1.5slm helium using the plate electrode at a 100% duty cycle.

$$O_2^- + N \rightarrow NO_2 + e^- \tag{5.10}$$

$$O^- + NO^+ + Ar \rightarrow NO_2 + Ar \tag{5.11}$$

$$NO + O_3 \rightarrow NO_2 + O_2 \tag{5.12}$$

after which HNO_3 can be formed by [68]

$$OH + NO_2 + M \rightarrow HNO_3 + M, \tag{5.13}$$

which can be ionized to form HNO_3^+.

The platinum orifice acts as an additional electrode as it is grounded via the vacuum vessel of the mass spectrometer setup. As a result the morphology of the plasma changes to a more filamentary state when touching the orifice. Because of this, even though the total plasma dissipated power is kept constant, the power density will be different when touching compared to not touching the orifice. This can in turn lead to additional differences between touching and non touching conditions, which do not directly arise from the difference of sampling within the plasma or in the effluent. Because of this effect the results shown of the plasma touching the orifice are not representative for the bio treatments shown in this work. A possible solution for this problem is using much higher gas flows (e.g. approximately 4 or 5 slm), in which case the plasma is optically more diffuse and there is no visible contracted discharge channel to the orifice.

When not touching the orifice (approximately 5mm between the orifice and the tip of the plasma plume) on the other hand, only H_2O^+ and H_3O^+ and their respective clusters of up to 6 water molecules are visible, as is seen in figure 5.16b. Where Ar^+, ArH^+, Ar_2^+ and Ar_2H^+ show the highest amount of counts when touching the orifice, none of them are visible when the plasma plume is not touching the orifice. The fact that only clusters are visible can be explained by the fact that any ions reaching the detector will have traveled a much larger distance through the argon/humid air atmosphere, which increases the chances of accumulating water molecules due to charge exchange which leads to ions with a lower ionization potential. The reason for cluster formation is that the initially created ions are transformed to the most stable ions (i.e. lowest ionization energy) by charge exchange, for example:

$$Ar^+ + H_2O \rightarrow H_2O^+ + Ar, \tag{5.14}$$

followed by

$$H_2O^+ + H_2O \rightarrow H_3O^+ + OH, \tag{5.15}$$

finally resulting in

$$H_3O^+ + H_2O + M \rightarrow H_3O^+(H_2O) + M. \tag{5.16}$$

The fact that there are also clusters in the measurements in which the plasma is touching the orifice may be partly explained by the fact that when the measurements were performed, there was a large amount of water in the vacuum vessel. Also, due to the use of plastic gas tubes water is always present in the gas flow. The situation in which the plasma is touching the orifice is not representative of for the treatment conditions as in these treatments the plasma is not touching a surface. After the preliminary measurements presented in this section were performed, self adhesive heater mats were installed to be able to regularly bake the vacuum system and reduce the water content. In mass spectrometry measurements performed by Bruggeman et al.[69] on a water helium atmospheric pressure discharge H_3O^+ was also found, but there was no H_2O^+. The reason for this is the fast charge exchange (reaction 5.15) which will quickly convert it to H_3O^+ and its clusters. As these clusters are both found in the measurements presented in this work, this would mean that the production of this cluster ions happens at least partly in the orifice or first stage of the mass spectrometer at reduced pressure. This is because after the initial pressure reduction, charge exchange producing H_3O^+ is very unlikely due to the much lower collision rate. Clustering could however still occur due to a reduction in the temperature of the supersonic expansion. Further research is necessary to explain all of the the observed effects.

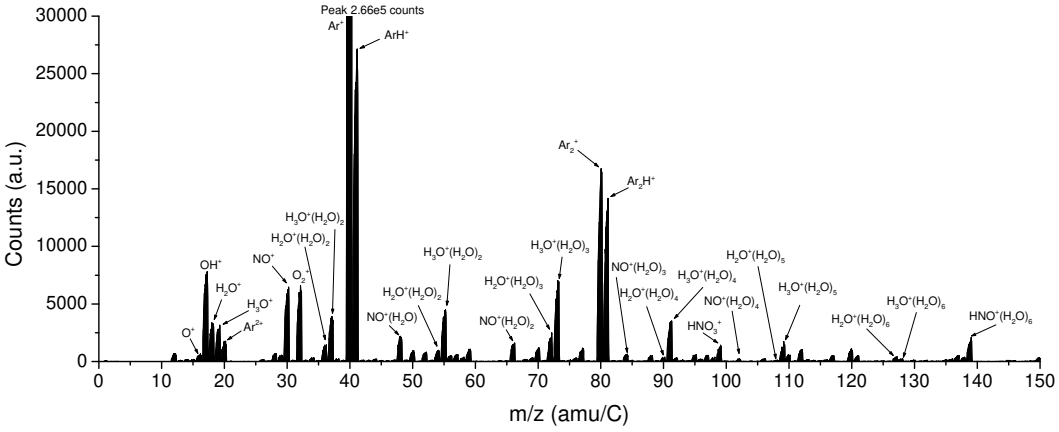

(a) Positive ions touching

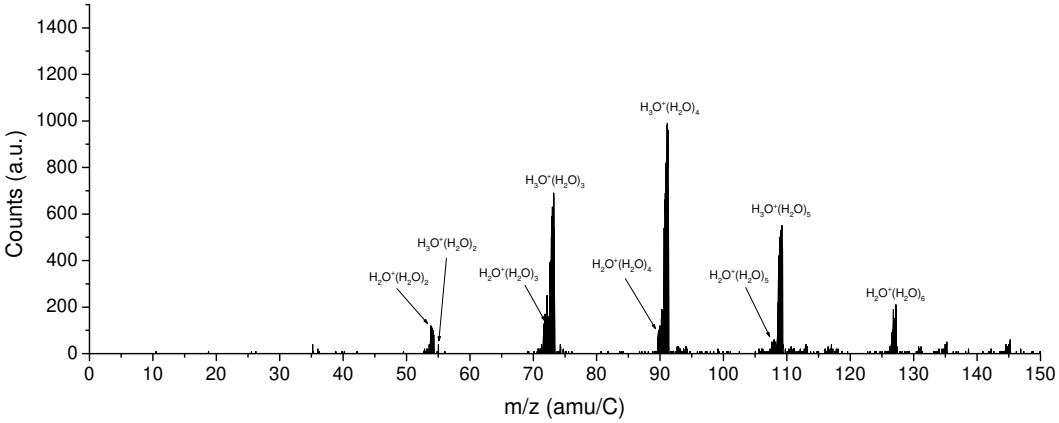

(b) Positive ions not touching

Figure 5.16: Positive ions measured using the platinum orifice at 1.4W of plasma dissipated power in a ring electrode argon plasma. When touching the orifice the plasma changes morphology to a highly filamentary geometry due to an electrical connection to ground.

Figure 5.17a shows measurements of negative ions when the plasma is touching the orifice. In this case the most dominant ion is O^-, which is formed by

$$O_2 + e^- \rightarrow O^- + O, \tag{5.17}$$

followed by a peak that is caused by either CN^- or $C_2H_2^-$. OH^- is also present, which is formed by

$$H_2O + e^- \rightarrow OH^- + H, \tag{5.18}$$

as well as its cluster $OH^-(H_2O)$. Small amounts of ArO^-, ArH_2^-, $H_2O_2^-$ as well as NO_2^- can also be seen. Lastly, there also seem to be contaminants present in the form of C^-, C_2^-, C_2H^- and $CN^-/C_2H_2^-$.

As was the case for positive ions when not touching the orifice, the negative ions also show only cluster formation when sampling in the effluent as seen in figure 5.17b. In this case the most dominant clusters are $H_2O^-(H_2O)_n$ via

$$e^- + H_2O + M \rightarrow H_2O^- + M \tag{5.19}$$

and $HO_2^-(H_2O)_n$. While the neutral molecule of the latter is easily formed by

$$H_2O_2 + e^- \rightarrow H + HO_2 + e^-, \tag{5.20}$$

no ionization of this molecule is expected from literature as it is observed to dissociate. Ions of the same mass have been observed before in oxygen-acetylene flames[70], where the possibility of it being CH_5O^- in stead is suggested. Again possible contaminants are seen in the form of $CO_4^-(H_2O)_n$. Carbon containing ions are also reported by Bruggeman et al. at low discharge powers[69]. An interesting thing to note is that even though the amount of counts is comparable to those shown in figure 5.16b, the latter shows more well-defined defined peaks and a much lower noise level. Positive ion counts are zero in between peaks whereas in the case of negative ions there is always a certain baseline level of approximately 20 to 30 counts.

Because of the filamentary nature of the plasma when touching the orifice, the orifice is etched, increasing its diameter from a circular 28 µm to an elliptical shape with diameters of 173 and 109 µm after several days of measuring. As a result the molecular beam expansion changes and the pressure in the first and second stage increases dramatically, requiring a replacement orifice to be installed. This effect is likely caused by the high current densities resulting from the limited thickness of the orifice, which in practice acts as an electrode when the plasma is in contact with the orifice.

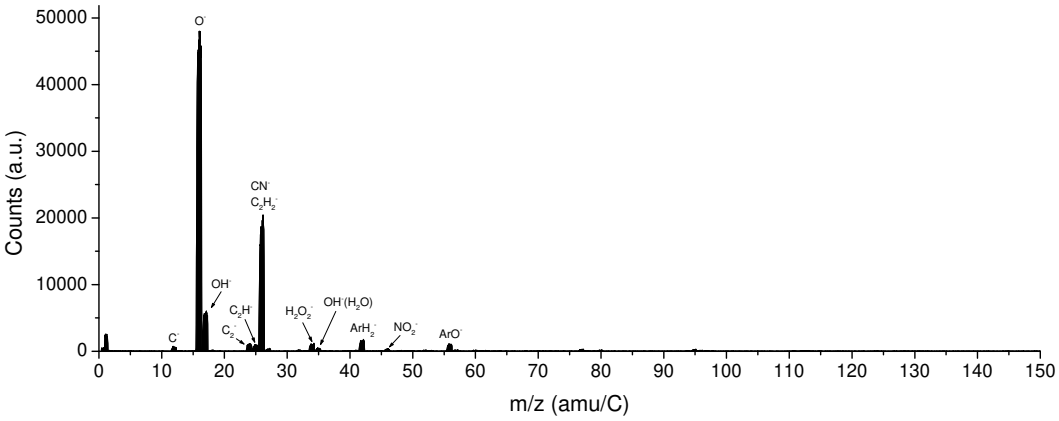

(a) Negative ions touching

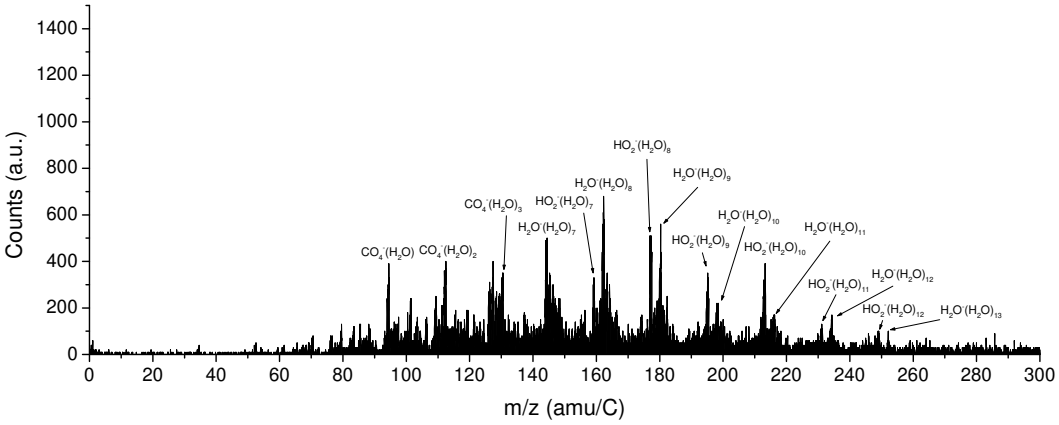

(b) Negative ions not touching

Figure 5.17: Negative ions measured using the platinum orifice at 1.4 W of plasma dissipated power in a ring electrode argon plasma. When touching the orifice the plasma changes morphology to a highly filamentary geometry due to an electrical connection to ground.

5.5 Ion chromatography

As an addition to the mass spectrometry measurements, the introduction of chemistry in the treated liquid is analyzed by measuring the concentrations of nitrite and nitrate for various conditions and various treatment times using a 1.5 slm argon plasma generated using the ring electrode geometry. All presented concentrations are corrected for evaporation of the water during plasma treatment.

Nitrite (NO_2^-) and nitrate (NO_3^-) concentrations are measured as a function of air percentage at constant power and constant function generator voltage in figure 5.18a and 5.18b respectively. The treatments were performed in 3.35 ml of distilled water with a volume proportional treatment time (with respect to the 100 µl liquid volume used in bacteria and cell treatments). By adding air, the power dissipation for fixed function generator voltage decreases due to a change in impedance and therefore a less efficient power transfer. Even though the plasma power dissipation is lower, nitrite generation is still higher for higher added air percentages. The same measurements are performed at a constant plasma power dissipation of approximately 3.8 W. A maximum nitrate generation is achieved using a 1% air admixture at constant (3.8 W) plasma power. The prepared samples were measured again five days after treatment, which shows that over time the nitrate concentrations increase whereas the nitrite concentrations decrease, even passing below the detection limit. The total concentration of nitrate and nitrite however does not remain constant. This effect is further discussed in chapter 7.

Figure 5.18c shows the behavior of nitrite and nitrate concentrations as a function of treatment time. Nitrite concentrations increase at first, but decrease after approximately 20 seconds of treatment time. Nitrate levels however continuously increase, in a seemingly linear relation. The same behavior is five days after treatment, but the maximum in nitrite concentration has shifted to approximately 5 seconds of treatment time. Again nitrate concentrations are higher after five days and nitrite concentrations are lower.

As expected, an increase in plasma dissipated power results in higher nitrate values and lower nitrite values, as seen in figure 5.18d.

It should be noted that even though the water was thought to be distilled, there was still a residual concentration of 0.01 mM of chloride present in the samples, which remained constant over all treatment settings and treatment durations.

5.6 Hydrogen peroxide measurements

A volume of approximately 3.8 ml of distilled water was treated using a 1.3 W argon plasma generated using the ring electrode for various time durations. The effect of treatment on the H_2O_2 concentration is shown in figure 5.19, where the concentration is shown as a function of volume proportional treatment time corresponding again to a 100 µl volume. Before treatment, the hydrogen peroxide concentration is assumed zero and it increases nonlinearly up to a value of 0.62 mM after 63 s of proportional treatment time. This corresponds to a 40 minute treatment time of a volume of 3.8 ml. The measured values are corrected for evaporation of the liquid.

A possible explanation for the nonlinear behavior is an increase in humidity close to the surface of the liquid over time due to evaporation, leading to an increased production of OH. A linear evaporation of the liquid is observed, as mentioned in section 4.7. It is known from previous research performed in helium discharges that the production of hydrogen peroxide approximately scales quadratically with water concentration in the gas flow as

$$\frac{d\left[H_2O_2\right]}{dt} \propto \left[H_2O\right]^2, \tag{5.21}$$

as the OH production scales approximately linearly with water content at low water concentrations [71]. As a result a small increase in water concentration can lead to a significant

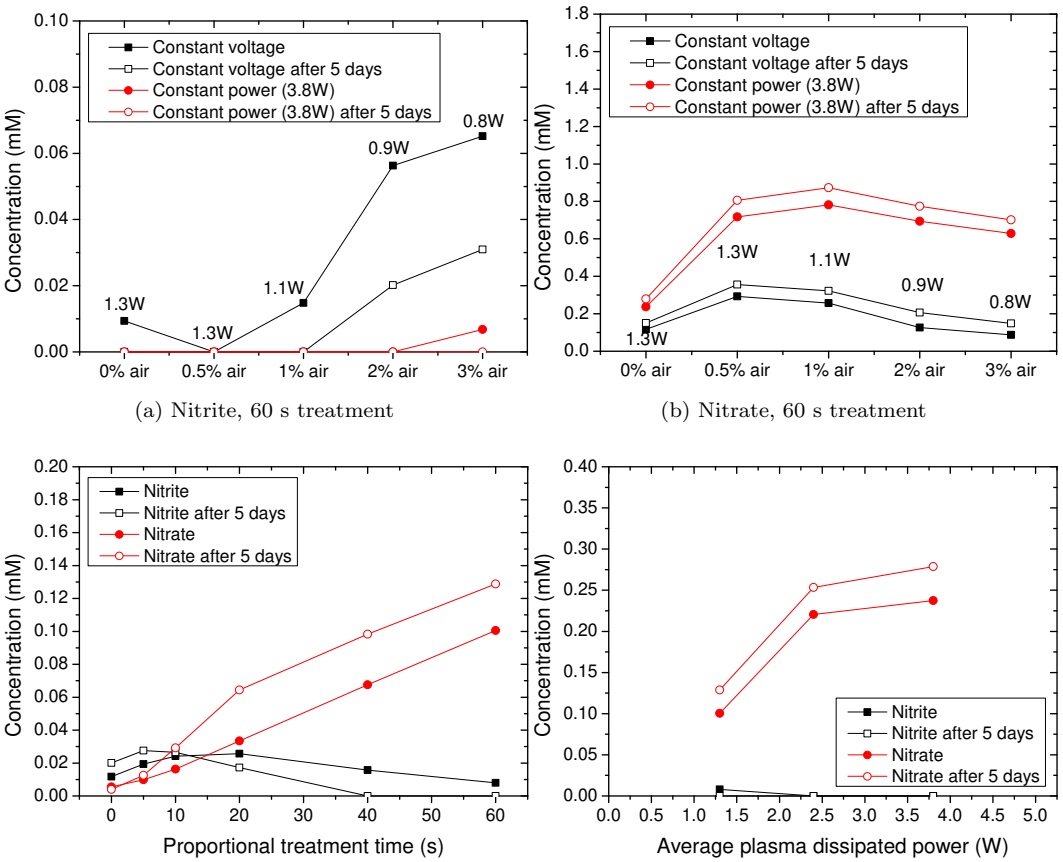

(a) Nitrite, 60 s treatment

(b) Nitrate, 60 s treatment

(c) Nitrite and nitrate as a function of time at 1.3 W

(d) Nitrite and nitrate as a function of plasma power, 60 s treatment

Figure 5.18: Ion chromatography measurements showing the concentrations of nitrate and nitrite in distilled water as a function of added air percentage, volume proportional treatment time and plasma dissipated power. Treatments performed using a ring electrode 1.5 slm argon plasma.

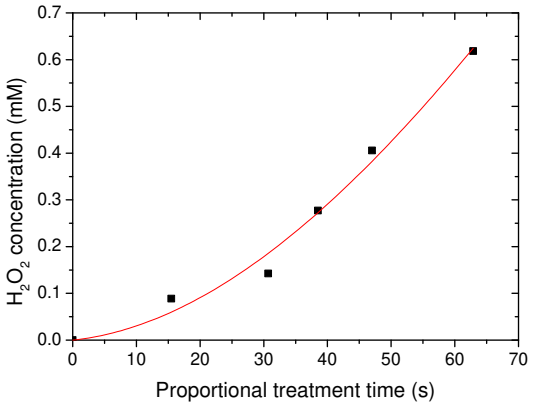

Figure 5.19: Measurement of H_2O_2 concentration as a function of volume proportional treatment time using a 1.3W ring electrode argon plasma. A quadratic fit of the function $[H_2O_2](t) = -4.68 \cdot 10^{-7}t^3 + 0.165 \cdot 10^{-3}t^2 + 1.44 \cdot 10^{-3}t$ mM is shown in red.

increase in H_2O_2 production. When assuming a linear increase in water concentration above the surface of the liquid from an initial value $[H_2O]_0$,

$$[H_2O](t) = Ct + [H_2O]_0, \tag{5.22}$$

where C is a constant, an estimate of the concentration of H_2O_2 is (assuming no peroxide in the liquid before treatment)

$$[H_2O_2](t) \approx C_1t^3 + C_2t^2 + C_3[H_2O]_0t, \tag{5.23}$$

where C_1, C_2 and C_3 are proportionality constants. Using the measurement data and fixing the intercept at a concentration of 0 mM, a third order fit of the function

$$[H_2O_2](t) = -4.68 \cdot 10^{-7}t^3 + 0.165 \cdot 10^{-3}t^2 + 1.44 \cdot 10^{-3}t \tag{5.24}$$

(in mM) is found, which is shown in red in figure 5.19.

5.7 pH change of solutions as a result of plasma treatment

The pH value of the different solutions was measured as a function of treatment time using a *VWR Symphony SB70P* pH meter. Due to the size of the pH sensor, the minimum volume required for pH measurements is 2 ml. The treatment time is again corrected for this proportionally to volume by using a treatment time which is twenty times longer.

The results of these measurements are shown in figure 5.20a. In the case of 'Saline pH 7.78' the pH of saline was artificially raised to this value by adding NaOH. As expected the LB and PBS show only a slight change in pH over time because of their buffer capacity (see chapter 7 for more details). The same is true for the two different concentrations of sodium acetate solution, where a higher concentration shows less pH change due to an increased buffer capacity. Only saline and distilled water show a clear effect of plasma treatment, decreasing in pH to a value of approximately 4. In figure 5.20b, the results of adding air to the plasma at approximately the same power are shown, with the behavior of distilled water shown in figure 5.20a as a reference. A higher power results in a faster decrease in pH and adding air adds to this effect. Section 7.6 treats buffer solutions in more detail.

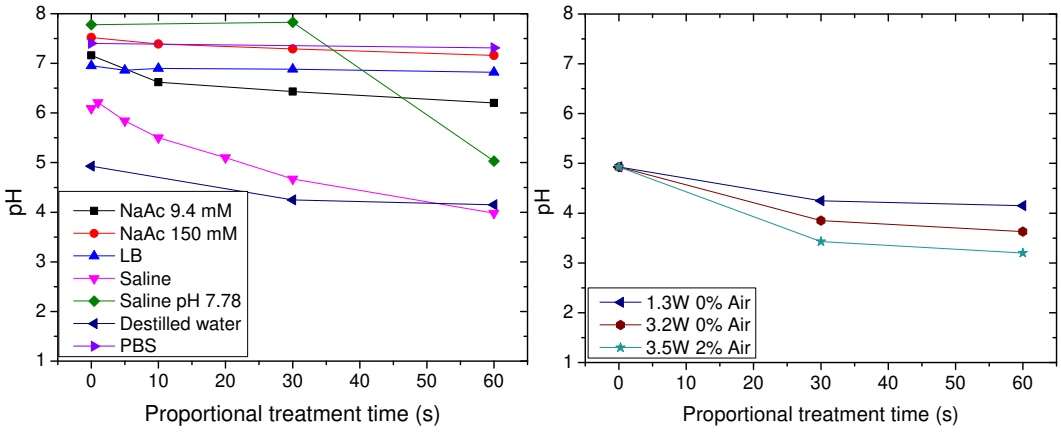

(a) Various liquids, 1.3W.

(b) Distilled water, 0% air and 2% air.

Figure 5.20: pH as a function of volume proportional treatment time for various solutions (2ml volume) treated with a 1.5slm Argon plasma using the ring electrode at a duty cycle of 20%. In one case the pH of saline is artificially raised by adding NaOH. Treatment time is corrected to be applicable to volumes of 100 µl.

Chapter 6

Treatment results

This chapter shows the results of treatments of biological samples performed at the laboratory of the Association of Dutch Burn Centres in Beverwijk. The majority of the treatments of bacteria have been performed on the bacterium Pseudomonas aeruginosa. The decision to mainly use one bacterium was made to be able to systematically investigate the effects on one bacterium using different plasma conditions before looking to other bacteria. Due to time constraints only preliminary results are shown for Staphylococcus aureus. This does however already allow for an initial comparison of the susceptibility of the two bacteria to plasma treatment. Preliminary treatments of keratinocytes and fibroblasts are shown in the last sections of this chapter.

Various different treatments of bacteria were performed which can be divided into two main categories; treatments on an agar surface and treatment in a solution. Treatments of human cells were in all cases performed in a solution as these cells require hydration. When treated in solution the bactericidal efficacy was in some cases estimated by optical density measurements (maximum deactivated concentration), in other cases the absolute bacterial concentration was calculated by serial dilution and colony counting on agar plates. The latter is a more accurate but more time consuming and labor intensive method.

The most used plasma was generated using a ring electrode with a plasma power dissipation of approximately 1.3W, as this leads to relatively low gas temperatures while still producing an effective plasma. The carrier gas was argon and the set duty cycle was 20%. When adding air, the power for all different percentages of added air, namely 0%, 1%, 2% and 3% is kept constant at approximately 3.8W. This value is chosen as in this case both the total dissipated power and the RMS current is similar for all percentages of added air (as is seen in figure 5.3), leading to a more stable region in which the plasma dissipated power is the same. As the plasma dissipated power is not measured instantaneously but calculated from current and voltage measurements, this ensures comparable treatment powers.

In the case of agar plate treatment also the plate electrode is used, either in continuous or pulsed mode. The decision was made to focus on the ring electrode rather than the plate electrode as this geometry was less susceptible to plasma changes due to contacting a surface.

The distance to the sample (or treatment distance) is defined as the distance between the tip of the plasma and the liquid surface. The used treatment distance is 8 mm unless stated otherwise.

6.1 Pseudomonas aeruginosa

This section focuses on the bacterium Pseudomonas aeruginosa, which was introduced in section 3.6.

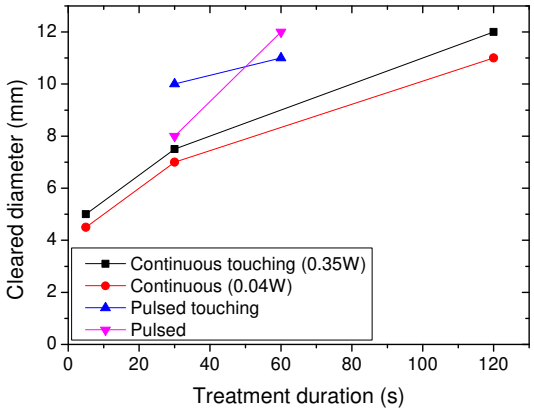

Figure 6.1: Cleared diameter of agar plate as a function of treatment time using the plate electrode.

6.1.1 Agar plate treatment

In the agar plate treatment, the plasma source using the plate electrode as a secondary electrode is positioned above the agar plate and plasma treatment is performed for different durations. After treatment the plates are incubated for 24 hours and the surface in which there was no growth is measured. An example of a treated agar plate is seen in figure 4.15, the area cleared of bacteria can clearly be distinguished from the opaque area surrounding it. The diameter of the cleared area as a function of treatment time for various conditions is shown in figure 6.1. In the case of the pulsed treatment, a 50% duty cycle is used and there were still some individual colonies visible inside the cleared area. When the plasma was not touching the agar plate the distance between the tip of the plasma plume and the surface of the plate was approximately 1 mm.

While this treatment method has the advantage of being somewhat comparable to an actual burn wound, using agar plates does not allow for testing of many parameters as this requires a large number of plates, making it very labor intensive. Also, the size of the cleared area seems to be diffusion and gas flow limited and as such might not be a good representation of the level of actual bactericidal effect. Any obtained deactivation curves are therefore expected to be dominated by diffusion and gas flow effects. Lastly, as human cells are treated in solution to avoid dehydration, treatment of bacteria in solution rather than on agar plates leads to more comparable results. Consequently, all further results in this chapter are obtained by treatment in a liquid medium.

6.1.2 Serial dilution treatments measured by optical density

In this section the optical density of treated 96-well plates is measured after 24 hours of incubation following plasma treatment using an ELISA plate reader. This produces a qualitative result; if there is no growth, the result will be an optical density of zero. If not all of the bacteria are deactivated, exponential growth will occur and the optical density will be much higher. It is therefore a binary result, either complete deactivation or not. A serial dilution is made to perform a scan of different initial concentrations. This means that the treatment is performed on various wells containing different concentrations of bacteria. By doing this the highest concentration in which all of the bacteria are deactivated can be determined by checking which well with the highest initial concentration of bacteria still has an optical density of zero after incubation.

Figure 6.2 shows the optical density of bacteria in LB as a function of initial bacterial concentration for various treatment times. The average plasma dissipated power is also indicated. As expected, a longer treatment time results in a higher deactivated initial

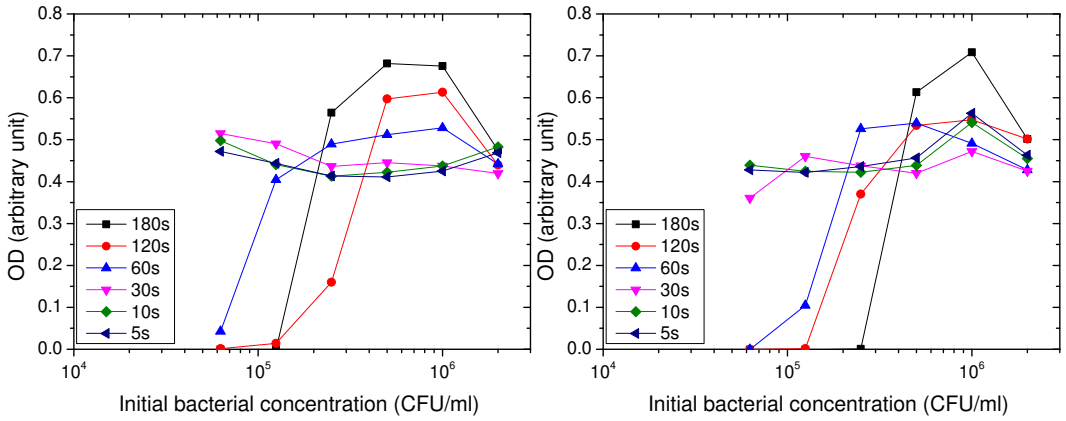

(a) Plate electrode continuous, 0.6 W (b) Ring electrode 20% duty cycle, 1.5W

Figure 6.2: Optical density measurements of bacteria in LB treated with 1.5 slm Argon plasma for 60 seconds for various treatment times.

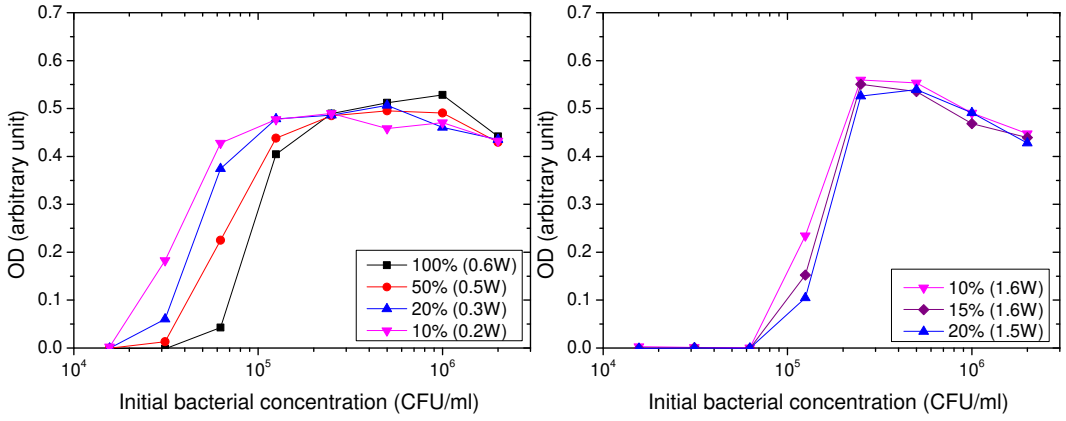

(a) Plate electrode (b) Ring electrode

Figure 6.3: Optical density measurements of bacteria in LB treated with 1.5 slm Argon plasma for 60 seconds for various duty cycles. The percentage indicates the set duty cycle.

concentration. Also, the ring electrode seems to be more effective as it deactivates the bacteria up to an initial concentration of $2.5 \cdot 10^5$ CFU/ml using a 180 s treatment time whereas the plate electrode deactivates up to approximately $1.25 \cdot 10^5$ CFU/ml. It should be noted however that the ring electrode has a higher plasma dissipated power (as can be seen in the legend).

The effect of pulsing the plasma source on bacteria in LB is shown in figure 6.3, for a treatment time of 60s. Again, a higher plasma dissipated power seems to result in more deactivation. Note that at a constant time averaged power dissipation, no significant difference is observed between the various duty cycles.

To check for any change of the LB solution by plasma treatment, the bacteria are added both before and after treatment of the medium. The results of this are shown in figure 6.4. Adding the bacteria shortly after treatment seems to have similar deactivating effects as directly treating the bacteria in the solution. This would suggest that plasma treatment of the solution results in a change of fluid composition and that bacteria are inactivated due to liquid chemistry.

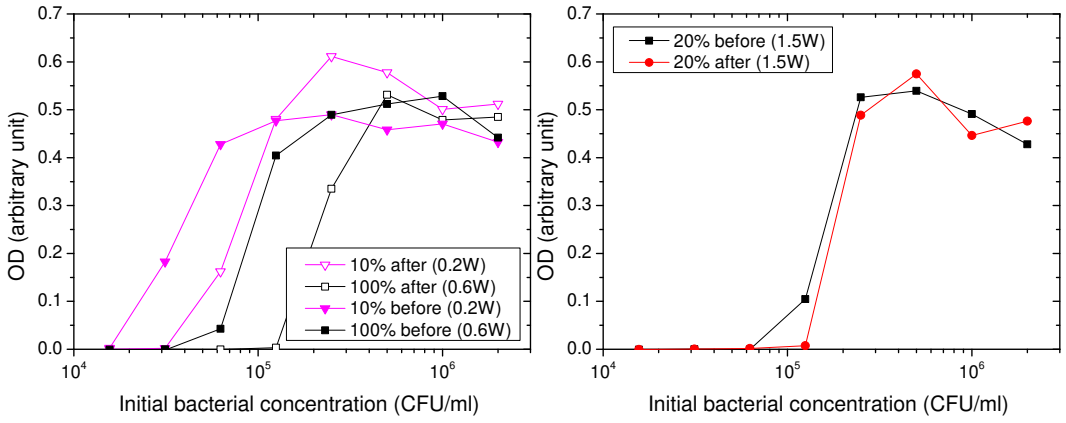

(a) Plate electrode (b) Ring electrode

Figure 6.4: Optical density measurements of bacteria in LB treated with 1.5 slm Argon plasma for 60 seconds. Bacteria are added either before or after plasma treatment. The percentage indicates the set duty cycle.

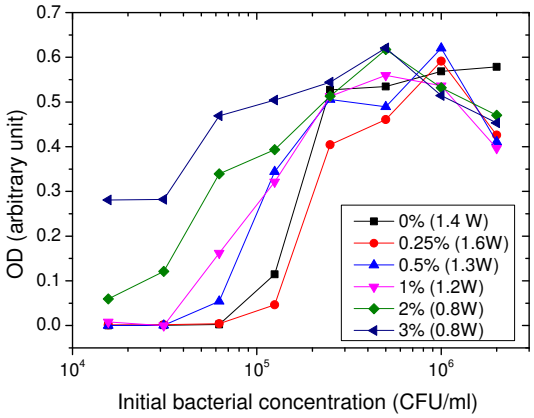

Figure 6.5: Optical density measurements of samples treated with 1.5 slm Argon plasma with a varied percentage of air using the ring electrode for 60 seconds with a duty cycle of 20%.

Also the effect of adding air to the gas flow was investigated with the ring electrode, the results of which are in figure 6.5. The percentages in the legend indicate the volume percentage of Air. Adding air seems to lower the plasma power dissipation for the same voltage setting which offers an explanation why a higher percentage of air in this case seems to result in a less effective deactivation. To obtain more reliable measurement results, the plasma power dissipation should be kept constant for the various percentages of air. The results of a constant power dissipation while adding air is shown later in this chapter.

In all of the treatments discussed before, plasma power dissipation seems to be a leading factor. This might be because a higher power can result in a higher electron density and thus radical density which increases the bactericidal effect. It is probably not due to an increase of temperature, as figures 5.7 and 5.8 show that the gas temperature is approximately 30°C in the case of the plate electrode and approximately 45°C for the ring electrode at comparable plasma dissipated powers.

The effect of plasma treatment on the fluid itself is investigated further. The bacteria are treated in both LB and PBS, spun in a centrifuge, after which the fluid is replaced within 5

Treated in	Fluid replaced with	Deactivation	Highest deactivated concentration
PBS	-	✓	$1 \cdot 10^6$
PBS	PBS	✓	$1 \cdot 10^6$
PBS	LB	✗	-
LB	-	✓	$3 \cdot 10^4$
LB	LB	✗	-

Table 6.1: Results of fluid effect tests. In all cases the bacteria are present during treatment. Fluid is not replaced if the second column reads '-'. ✓means deactivation, ✗means no deactivation. Replacement of fluid is performed within 5 minutes after treatment

minutes with new LB or PBS fluid. The results of these treatments are summarized in table 6.1. As expected, incubation of bacteria in PBS does not yield significant growth due to lack of nutrients, while treating in both PBS and LB and replacing the solution with LB results in growth at all initial bacteria concentrations. The fact that replacing the fluid in which the bacteria were treated with culture medium results in growth in all cases, provides a clue that while the bacteria are definitely deactivated by treatment in PBS and LB (possibly due to a change in the liquid medium), they are not killed. To check this a dilution of some of the treated wells is plated on agar plates, which resulted in growth in even the lowest concentrations. This shows that the plasma is clearly influencing the LB, rather than killing bacteria, making it unsuitable for bacterial growth.

As both LB and PBS have an intrinsic buffer capacity (discussed in more detail in sections 5.7 and 7.6), additional treatments were performed in which both PBS and LB were artificially acidified by adding HCl to a value of 4.0. This value was chosen because treating saline solution for the same length of time results in approximately this value, as is shown in figure 5.20a. To check if the bacteria are killed in stead of deactivated, after treatment new LB is added to facilitate bacterial growth. The results of these treatments are shown in table 6.2. The effect of acidity is clearly seen, as where treatment in LB leads to no deactivation after adding new LB, acidified LB does show permanent deactivation. It has to be noted that a pH value of 4.0 alone is not low enough to kill the bacteria, as shown in the last row. As a result the bactericidal effect has to be a combination of both low pH and other induced plasma effects.

Treatments of bacteria in saline while adding various percentages of air to the argon gas flow are performed at three different distances and the results are shown in figure 6.6. After treatment LB is added to make sure any remaining bacteria have the chance to multiply. Adding 1% of air seems to result in a slightly more efficient bactericidal effect; 10^7 in stead of 10^6 CFU/ml are killed. A more pronounced influence of distance to the liquid surface can be seen; when the plasma treatment distance is 1 mm less, the bactericidal effect can be as much as 2 orders of magnitude higher. This figure does however again illustrate the importance of buffer capacity on the bactericidal effect; the highest killed concentration is almost 10^7, almost an order of magnitude higher than the deactivation shown in table 6.1, where buffered solutions were used. Also in this case the bacteria are actually killed rather than denied the chance to multiply, as any residual bacteria are provided with the nutrients to multiply.

To exclude effects of any other chemical components already present in the liquid, treatments were also performed in distilled water. The effect of a 1.5 slm ring electrode argon plasma for various concentrations of air at a constant plasma power dissipation is shown in figure 6.7. After treatment LB was added to facilitate bacterial growth. Although adding 1 or 2% of air seems to increase the bactericidal effect, the change is minimal. This is comparable to results shown in figure 6.6.

Treated in	Fluid added	Deactivation
LB (pH 4.0)	LB	✓
LB	LB (pH 4.0)	✓
LB	LB	✗
PBS	LB	✗
PBS (pH 4.0)	LB	✓
Saline	LB	✓
-	LB (pH 4.0)	✗

Table 6.2: Results of fluid effect tests. In all cases the bacteria are present during treatment. The initial bacterial concentration is $9.75 \cdot 10^5$ CFU/ml. Bacteria are not treated if the first column reads '-'. ✓means deactivation, ✗means no deactivation. Fluid is added within 5 minutes after treatment

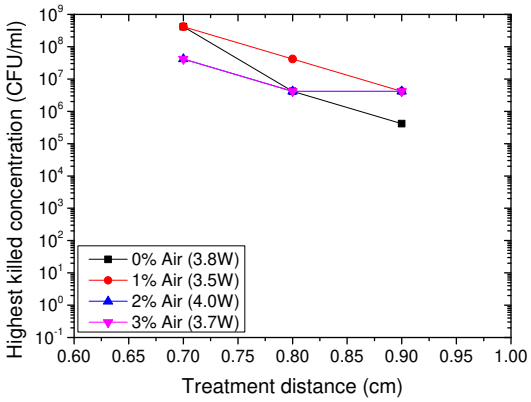

Figure 6.6: Highest killed bacterial concentration in saline for various concentrations of added air and various distances using a 1.5 slm ring electrode argon plasma for a duration of 1 minute.

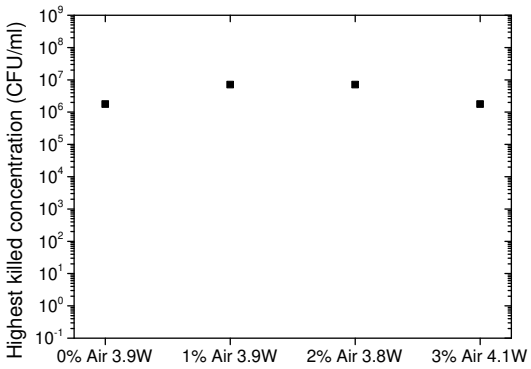

Figure 6.7: Highest killed bacterial concentration in distilled water for various concentrations of added air using a 1.5 slm ring electrode argon plasma for a duration of 1 minute at a constant power dissipation.

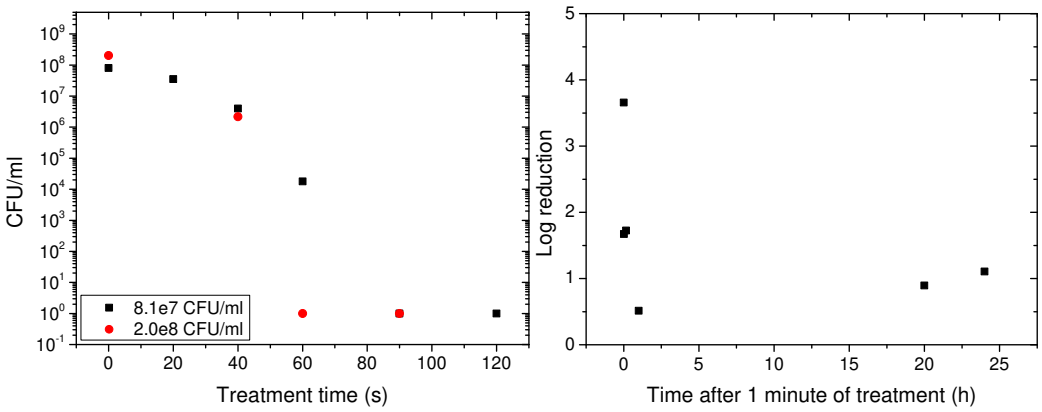

(a) (b)

Figure 6.8: Surviving bacterial density in distilled water as a function of treatment time (left) and log reduction of adding bacteria between 0 to 24 hours after a 1 minute treatment of distilled water (right). In the latter case the bacteria are suspended in the solution for 1 minute. In both cases a 1.3 W and 1.5 slm ring electrode argon plasma is used for the treatment.

After initial experiments using the optical density measurement method as presented in this section, a more accurate investigation of the effects of plasma treatment is shown in the next section, where serial dilution concentration measurements are used to determine the amount of viable bacteria in a plasma treated sample.

6.1.3 Treatments quantified by agar plating

The results in this section are acquired by treating bacteria in 96-well plates and using serial dilution and plating on agar plates to determine the amount of CFU/ml present after treatment. The advantage of this method compared to optical density measurements is that this is a direct measurement of the bacteria present in the liquid after treatment, making it a more accurate method. Also the optical density measurement has the added disadvantage that the concentration in each serially diluted well is (purposefully) different, making the various wells less comparable. In the results presented in this section, the reduction in bacterial density is determined directly. As a result only one well is treated for each setting, eliminating the effects of different initial bacterial concentrations as was the case in the previous section. This section will show that there is a clear dependency of the bactericidal effect on the initial bacterial concentration. If no residual bacteria are found after treatment, the graphs indicate 1 CFU/ml due to the logarithmic vertical axis.

In figure 6.8a the bacterial density as a function of treatment time of bacteria treated in distilled water is shown. The density of colony forming units decreases as a function of time, until the density is below the detection limit. The log reduction of the bacterial density as a function of time duration between treatment of the fluid and adding of bacteria is shown in figure 6.8b. In this case the fluid is treated for 1 minute and the bacteria are suspended in the solution for 1 minute. A strong dependency is seen in bactericidal efficacy and time between treatment of liquid and addition of bacteria. The two latest measurement points were obtained using a new batch of cultured bacteria of which the initial concentration was lower. This explains the apparent increased effect after approximately 20 hours, which in comparable concentrations is not expected to occur.

The effect of adding air to the plasma at constant plasma power dissipation while treating distilled water containing bacteria is shown in figure 6.9. While the power dissipation is not

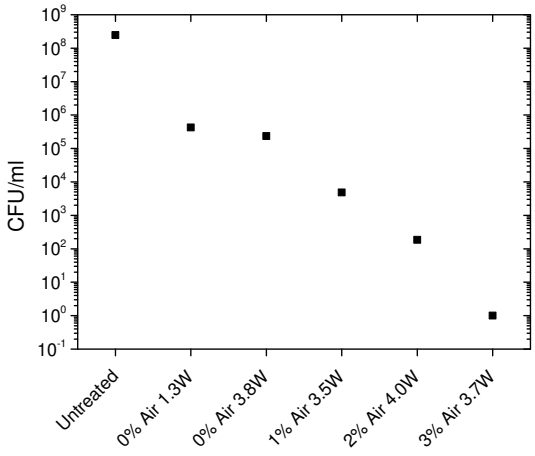

Figure 6.9: Surviving bacterial density in distilled water for various concentrations of added air using a 1.5 slm ring electrode argon plasma for a treatment duration of 1 minute.

exactly the same for each percentage of air, a clear trend can still be observed: adding air leads to an increase in bactericidal effect. This seems to contradict the findings shown previously in figure 6.7, the reasons of which are not exactly clear. However, the method described in this section is expected to be more reliable because of the direct measurement of CFU/ml.

For saline, PBS and LB, the results of argon plasma treatment are shown in figure 6.10a, 6.10b and 6.10c respectively. Various initial bacterial concentrations are shown, which illustrates the importance of bacterial concentration on treatment effectiveness. Higher concentrations lead to less effective treatments. For saline the pH level was artificially raised to a value of 8 by adding NaOH while for PBS and LB the value was lowered to 4 by adding HCl. As expected raising the pH leads to less kill whereas lowering it leads to more kill.

6.2 Staphylococcus aureus

The effects of plasma treatment on staphylococcus aureus as mentioned before has been less extensively investigated in this work. To be able to make a quantitative comparison between Pseudomonas aeruginosa and Staphylococcus aureus, a treatment of a patient isolate (named 4D4) in saline is performed. The results of the bactericidal effect on this bacterium is compared to the previously shown PAO1 Pseudomonas bacteria treatments in figure 6.11. Because the initial concentrations are not equal, Pseudomonas treatments with both higher and lower initial concentrations are shown. It is seen that the bactericidal effect on both species is comparable, showing similar deactivation curves. It is therefore concluded that plasma conditions which efficiently kill Pseudomonas aeruginosa are also likely to be efficient at killing Staphylococcus aureus.

6.3 Effect of plasma treatment on human cells

This section will show the results of treatments performed on keratinocytes and fibroblasts using similar settings as used in bacterial treatment. Both the released cell content and cell viability is determined.

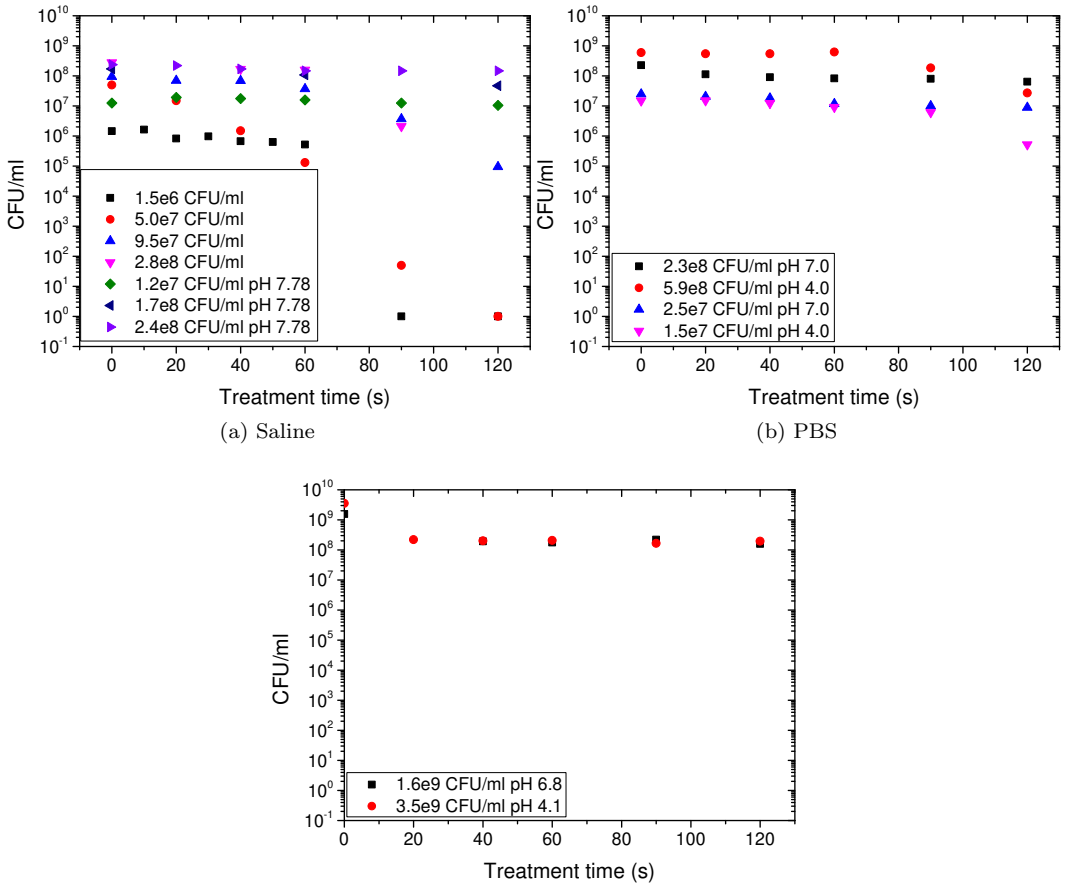

(a) Saline

(b) PBS

(c) LB

Figure 6.10: Surviving bacterial density as a function of treatment time for various initial bacterial concentrations (indicated in legend) and artificially influenced initial pH levels (if applicable) using a 1.5 slm ring electrode argon plasma at a plasma power dissipation of 1.3 W.

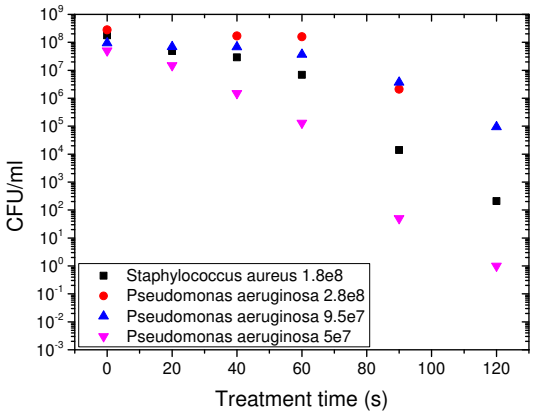

Figure 6.11: Surviving bacterial density in saline of Pseudomonas aeruginosa and staphylococcus aureus for various initial bacterial concentrations using a 1.5 slm ring electrode argon plasma at 1.3 W of plasma dissipated power. The initial bacterial concentrations are shown in the legend. Various Pseudomonas results are shown as the initial concentrations are not exactly equal.

6.3.1 Keratinocytes

Keratinocyte cultures in 96-well plates were treated with an argon plasma in both keratinocyte-conditioned medium (KCM) and saline. Afterwards the LDH release was determined and for another set of treatments the cell viability was measured.

Figure 6.12a shows the fraction of LDH release as a function of treatment time for two different treatment distances and two different duty cycles for keratinocytes treated in KCM solution. The measurement point at t=0 s indicates an untreated control sample. For treatment times up to 120 seconds the change in LDH release is minimal. Longer treatment times result in a significantly higher release of LDH. As KCM is buffered, this result is to be expected, and is in line with the effects of plasma on bacteria in buffered solutions, as shown in figures 6.10b and 6.10c. As a check the treatments were performed in saline, after which the LDH release was measured, the results of which are shown in figure 6.12b. Contrary to the expected result, the LDH release decreases as a function of time. Apparently either LDH is converted by the plasma into components which are not detected by this method or the used dye is influenced by the chemistry induced in the liquid. Both reducing in stead of increasing the measured LDH levels.

To exclude the possibility of a change of the LDH in the solution, cell viability measurements were performed using the same conditions. The cells were treated for various treatment durations, after which KCM was added after 1 minute or 120 minutes. After overnight incubation the cell viability was determined. The measurements are normalized using measurement values of treatments where only a gas flow was applied for the same amount of time. The results as a function of treatment time are shown in figure 6.13. A 1 minute exposure to the plasma treated saline results in little effect, whereas a 2 hour exposure shows a clear reduction of cell viability. As a 2 hour exposure to the plasma treated liquid is not necessary to achieve a bactericidal effect, simultaneous exposure of bacteria and cells to plasma treated liquids for short periods of time may result in being able to effectively kill bacteria while minimizing the damage inflicted on cells.

6.3.2 Fibroblasts

Preliminary cell viability measurements were also performed on plasma treated fibroblasts. For the results to be comparable to the treatment of bacteria and keratinocytes in unbuffered solutions, the treatments were performed in saline, one minute after which the saline is

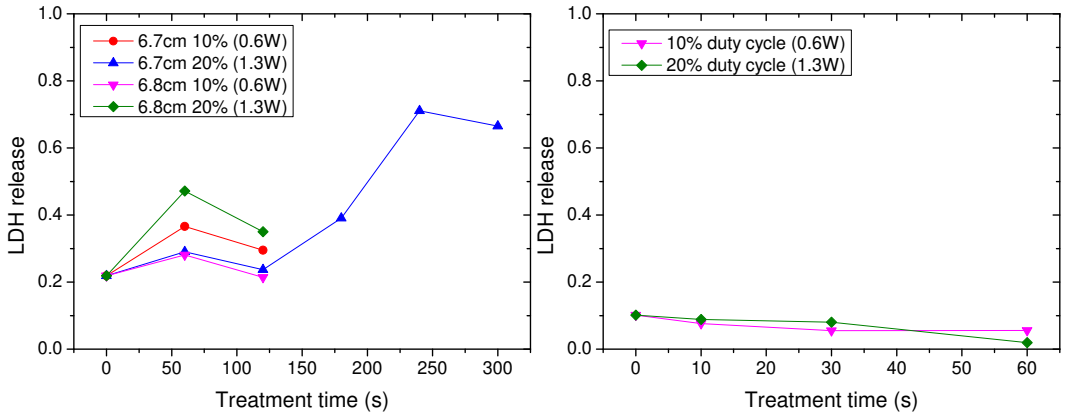

(a) KCM (b) Saline

Figure 6.12: Fraction of LDH release compared to total LDH content of keratinocytes treated with a 1.5 slm ring electrode argon plasma in KCM and saline for various duty cycles and distances.

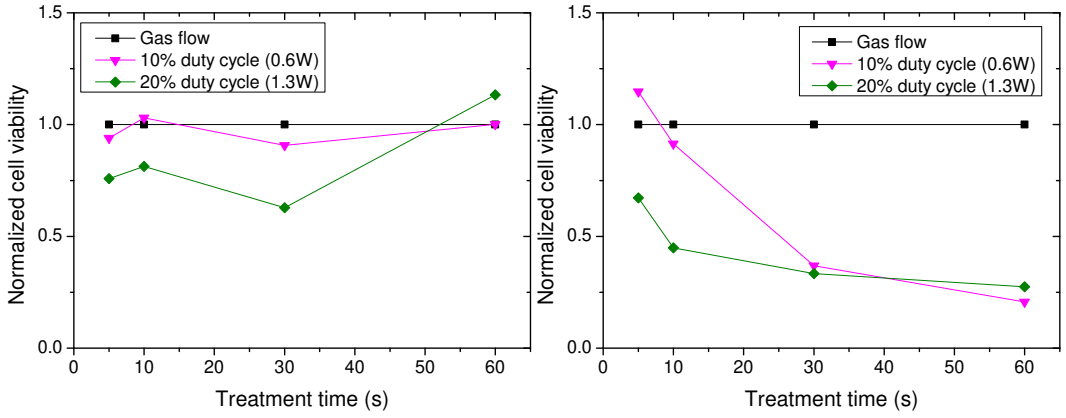

(a) KCM added after 1 minute (b) KCM added after 120 minutes

Figure 6.13: Treatment of keratinocytes in saline for two duty cycles after which KCM is added after approximately 1 minute and 120 minutes. Results obtained using a 1.5 slm ring electrode argon plasma at a distance of 6.8 cm. The values are normalized to the effects of only the gas flow.

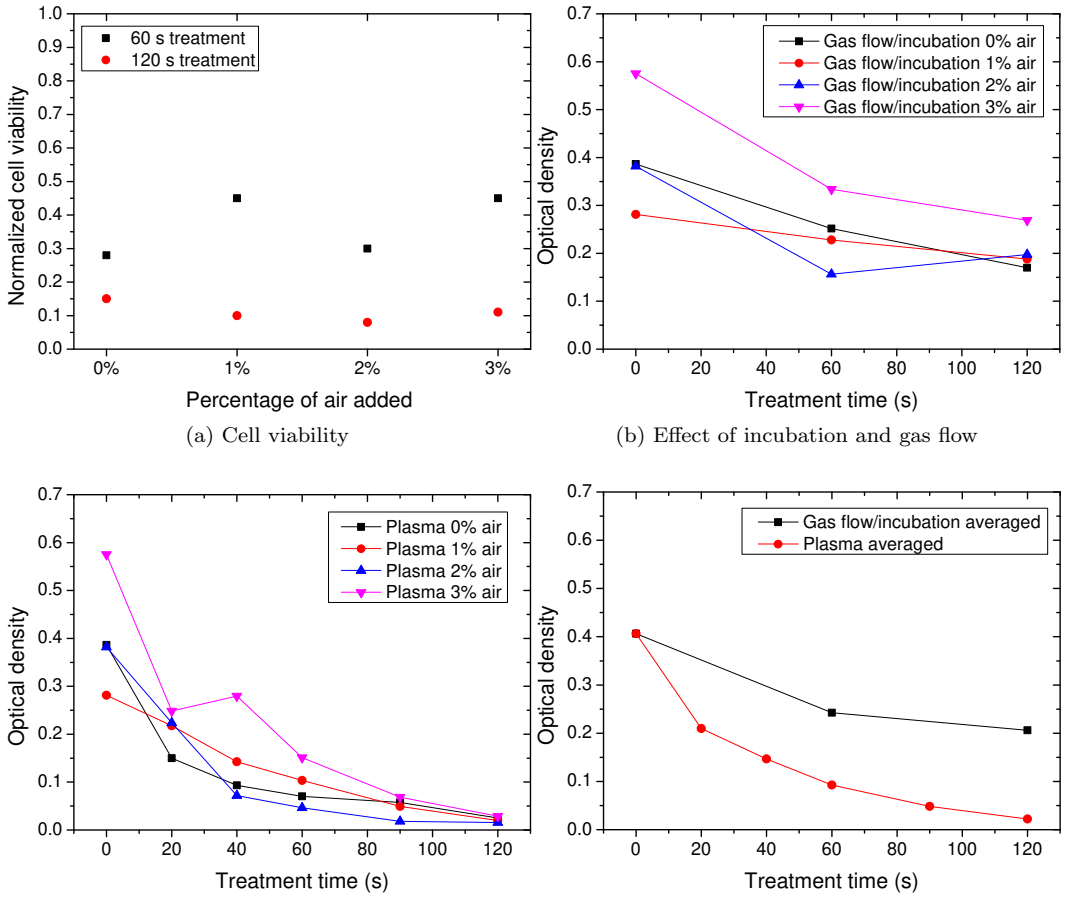

(a) Cell viability

(b) Effect of incubation and gas flow

(c) Effect of plasma treatment, incubation and gas flow

(d) Averaged effects of plasma treatment and gas flow/incubation

Figure 6.14: Treatment of fibroblasts in saline for different percentages of added air at a constant power dissipation of approximately 3.8 W. Cell viability in (A) is normalized to the effects of only the gas flow. Measurements were performed two days after plasma treatment.

replaced by FBM (Fibroblast Basal Medium). As the fibroblasts show a decrease in cell viability after one day due to the incubation in saline alone, the measurements are performed two days after treatment, in an attempt to isolate the effects of plasma treatment.

The results of these measurements are shown in figure 6.13. The cell viability as a function of added air percentage for two different treatment times is shown in figure 6.14a. The values are normalized to the effects of gas flow and incubation alone. A clear decrease is seen in cell viability as a result of plasma treatment, the decrease being more prominent for a longer treatment time. There is no clear difference visible between the various percentages of air added.

Gas flow and incubation in saline alone also has a detrimental effect on cells, which is shown in figure 6.14b. The effect of plasma treatment however is a larger reduction in cell viability as is seen in figure 6.14c. As the treatment effects do not show a significant dependence on added air percentage, the averages of all different percentages of added air of the gas flow alone (figure 6.14b) and the plasma treatment (figure 6.14c) are displayed in figure 6.14d. A clear exponential trend is seen. These latter three figures all show optical density values rather than cell viability.

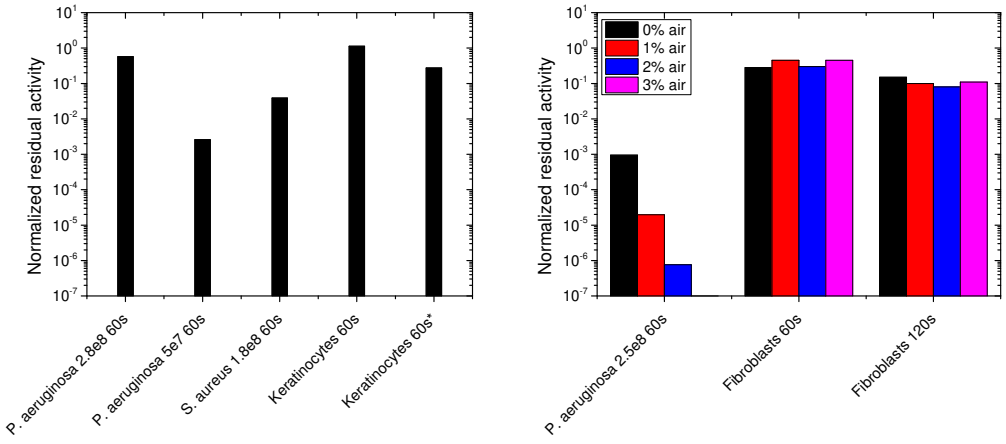

(a) 1.3 W

(b) ∼3.8 W

Figure 6.15: Comparison of treatment effects on bacteria and human cells. Vertical axis shows fraction of cells alive after treatment. An asterisk in (a) indicates submersion of the cells for 120 minutes in stead of 1 minute in the treated liquid. In (b) the bacterial treatments showed no residual bacteria using 3% of added air. All treatments are performed in saline, except Pseudomonas aeruginosa in (b), which is treated in distilled water. The starting concentrations in CFU/ml of the bacteria are shown on the horizontal axis.

6.4 Treatment summary

In order to achieve a better view of the effect of plasma treatment on cells and bacteria, this section summarizes some of the results of the previous sections to allow for a comparison between the treatment of human cells and bacteria. All of the shown treatments are performed in saline, unless stated otherwise.

Figure 6.15a shows a comparison of both types of bacteria and keratinocytes, where a plasma power dissipation of 1.3 W was used. The vertical axis shows a normalized residual activity, which is defined as the fraction of viable cells or bacteria present after treatment compared to the initial amount. An asterisk in the horizontal axis of this figure means that the keratinocytes were submersed for 120 minutes. Other cells were submersed for 1 minute. As seen before, the reduction in bacterial density is highly dependent on the initial concentration. Also, the susceptibility of keratinocytes to the treatment increases when they are submersed in the treated liquid for longer periods of time.

The effects of adding air using a higher power (3.8 W) on Pseudomonas aeruginosa and fibroblasts are shown in figure 6.15b. The bacterial treatments are in this case performed in distilled water. A much larger reduction in bacterial density is achieved at these higher powers. However, also the fibroblasts suffer from these treatments. Especially long (120 s) treatment times result in a large decrease in viable cells.

In general it seems that while bacteria are completely killed shortly after treatment, cells can survive being in the treated medium for a longer time. As a result, a treatment in liquid can kill bacteria and preserve the human cells if the exposure to the treated solution is short enough. This does however indicate possible different inactivation mechanisms or rates.

These graphs show that the set of treatments is far from complete, so while these treatments provide an initial insight into the effects of plasma treatment on both human cells and bacteria, additional treatments have to be performed to be able to adequately compare and analyze the results as well as to determine the statistical significance.

Chapter 7

Discussion: analysis of inactivation mechanisms

This chapter will discuss the connections between the diagnostics results and the biological treatment results in order to deduce mechanisms of bacterial inactivation and which constituents of the plasma are responsible for these effects. By doing this, an assessment is made of the contributions of the individual components such as gas temperature, ions, radicals, UV, electric fields and gas flow. The measurements of the ultraviolet flux generated by the plasma source is compared to exposure limits of human skin and eyes, and the absorption of UV by solutions is estimated. The effect of the resulting UV-flux is compared to UV sterilization data in literature. Fluid chemistry calculations are performed and compared with measured concentrations of nitrite and nitrate and a comparison is made between the experimentally measured and the calculated production of hydrogen peroxide. The lasting bactericidal effect of plasma treated solutions is discussed, and suggestions of possible chemical bacterial inactivation pathways are discussed. The results are compared to previous research on the effects of the individual components.

7.1 Effect of heat

The gas temperature of the various plasma conditions varies with plasma dissipated power and is also dependent on the addition of air. Figure 5.8 shows that in the case of a 1.4 W 1.5 slm argon plasma generated using the ring electrode has a temperature of approximately 60°C close to the tip of the plasma plume, which rapidly decreases as a function of distance. At approximately 8 mm, the most used distance for biological sample treatments in this work, the gas temperature is between 40 and 45°C. When using a higher power dissipation of approximately 3.7 W, the gas temperature increases to a value of approximately 230°C inside the plasma jet as seen in figure 5.10. Adding air at constant power slightly reduces the gas temperature to a value of approximately 180°C. While these gas temperatures are substantially higher than in the case of 1.4 W of plasma dissipated power, these temperatures are measured within the plasma jet. As a result, the gas temperatures in the effluent are expected to be significantly lower.

The optimal growth temperature for Pseudomonas aeruginosa is 37 °C, but it will still replicate at a temperature as high as 45 °C[72] and a temperature of approximately 60°C for a duration of 30 minutes is required to result in significant thermal kill[73]. As the gas temperature at 1.4 W is not even high enough to stop the growth of bacteria and the treatment time is always approximately 1 minute, the gas temperature of the used plasma conditions is not expected to contribute to the bactericidal effects of plasma treatment. Additionally, the temperature of the solution containing bacteria is at room temperature at the start of the treatment. As such the solution would have to be significantly heated for

any thermal effects to occur. As a minimum estimate, the energy needed to heat 100 µl of water from room temperature to 60°C is

$$Q = c \cdot m \cdot \Delta T = 4181.3 \cdot 10^{-4} \cdot 40 \approx 16.8\text{J}, \tag{7.1}$$

which over a course of 60 seconds leads to a minimum power dissipated in the water of approximately 0.3 W. However, this is assuming no heat is lost from the liquid over time due to conduction and evaporation, and even then the length of time in which the water is at this temperature is not nearly long enough to result in a significant reduction of bacterial density.

A more compelling argument to discard the temperature as being of influence on the bactericidal effect is the fact that the efficacy in buffered solutions (figures 6.10b and 6.10c) is orders of magnitude lower than in non-buffered solutions, indicating a dominant chemical effect. Because of the above mentioned reasons, the increase in temperature as a result of plasma treatment is assumed to be of no significant influence.

7.2 Effect of ions

As stated before, the distance between the tip of the plasma plume and the liquid surface is typically approximately 8 mm. Figures 5.16b and 5.17b show that there is a limited flux of ions reaching a distance of approximately 5 mm from the tip of the plasma plume, consisting only of clusters. These clustered ions are mostly comprised of H_2O^+, H_3O^+, H_2O^- and HO_2^-. However, as stated before, the $H_2O(H_2O)_n$ clusters are expected to be an artifact of the measurement method and in reality they are expected to form $H_3O(H_2O)_n$. As a result, the most dominant expected reaction of these ions when reaching the liquid surface is [13]

$$M^+ + H_2O \rightarrow M + H_2O^+, \tag{7.2}$$

where M^+ is an arbitrary ion. As such, any influence of incoming flux of positive ions is expected to be expressed in induced fluid chemistry rather than any direct effect on bacteria or cells present in the liquid.

Negative ions on the other hand show a more complicated behavior, which is not completely understood. There are however indications that negative ions have a propensity to adsorb at the surface of the liquid rather than penetrate into the bulk and absorb, due to a significant dipole moment due to the oriented molecules in the top water layer[74]. Because of the adsorption, negative ions are not expected to react directly with bacteria or cells present in the liquid.

More importantly, Hofmann et al.[49] measured an electron density of approximately 10^{20}m^{-3} (∼10 ppm) inside the plasma plume. When taking into account recombination the actual density of ions at the liquid surface is significantly (several orders of magnitude) lower. Radical densities are expected to be much higher, as further discussed in section 7.6.

7.3 Electric field effects

The effect of the electric fields generated by the plasma treatment on cells in the liquid has been reviewed before by Hülsheger et al.[75]. The survival rate of a bacterium as a result of electric fields was described by

$$\hat{s} = \left(\frac{t}{t_c}\right)^{-(E-E_c)/k}, \tag{7.3}$$

where $\hat{s}$ is the relative survival rate, E_c is the threshold value of field strength in kV/cm, t_c is the threshold value of treatment time in seconds and k is an additional factor. For Pseudomonas aeruginosa, the values of field strength, treatment time and the additional

factor are approximately 6 kV/cm, 35 µs and 6.3 respectively. For Staphylococcus aureus they were found to be 13 kV/cm, 58 µs and 2.6 respectively. Any influence of the electric fields should also be approximately similar in any of the treated liquids. However, as was the case for the influence of temperature, electric fields can not account for the difference in bactericidal effect between buffered and non-buffered solutions. Also, the generated electric fields at the treatment location are expected to be significantly lower than the threshold values and no effect of only electric fields on bacteria was observed in this work.

7.4 Gas flow effects

Gas flow alone is found to be harmless against bacteria suspended in solution, and may only pose a problem for human cells when the flow is such that any liquid on top of the cells is forced aside. In that case the cells will be influenced by dehydration. As long as the flow is lower than this value however, gas flow alone shows no significant influence.

As a result of the discussion above, the observed bactericidal effects of plasma treatment are not attributed to either gas temperature, direct cell-ion interaction, induced electric fields or gas flow. The possible bactericidal effects of UV and the influence of ions and radicals on fluid chemistry are discussed in the remainder of this chapter.

7.5 Effect of UV exposure

This section will provide a discussion on the possible effects of the measured absolute UV-fluxes on human tissue and cells as well as bacteria. An estimation of the absorbance of UV by the culture medium or salt solution is provided and guidelines on UV exposure of human skin and eyes are discussed.

The absorbance of a solution is defined as

$$A = ad = -\log\left(\frac{I}{I_0}\right), \tag{7.4}$$

where a is the attenuation coefficient in cm^{-1}, d is the length of the optical path through the medium in cm, I is the transmitted intensity and I_0 is the incident intensity. As a result, the ratio of incident and transmitted intensity is given by

$$\frac{I}{I_0} = 10^{-ad}. \tag{7.5}$$

Figure 7.1 shows the absorbance of saline as a function of wavelength for various concentrations of NaCl. Normal saline contains approximately 0.15 molL^{-1} of NaCl. As the absorbance in this case is measured over an optical path length of 1cm, the absorbance is equal to the attenuation coefficient. The main part of the absorption is present around 200nm, whereas the measured spectra of UV emitted by the plasma jet introduced in section 5.3 show that the lowest wavelength with a significant intensity is approximately 210 nm. This means that absorption of the plasma generated UV by the column of solution in the wells is negligible, as $a \approx 0.01$ at a wavelength of 210 nm and as a result $\frac{I}{I_0} = 10^{-0.01} \approx 0.98$. However, as the absolute UV-flux has only been measured starting from 200 nm and the absorbance is seen to go down below this value, VUV has to be considered as well.

The possibility of VUV emission by a plasma jet and its bactericidal effects were investigated by Brandenburg et al.[77]. In a 20 W, 20 slm argon jet without adding air, the second continuum of the argon excimer[1] (Ar_2^*) at 126 nm is found to be the dominant element in VUV emission. When adding air, the VUV emission is dominated by nitrogen and oxygen emission. By using filters that either transmit only UV and both VUV and UV,

[1]Excimers are molecules with a short lifetime (in the order of nanoseconds) of which at least one of the atoms is in an excited state. Often these atoms would not bond while being in the ground state.

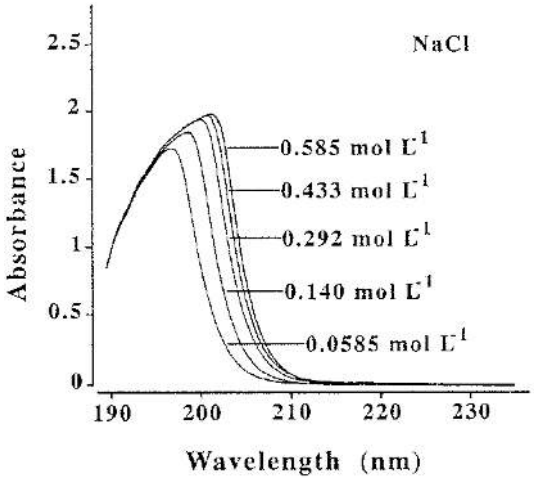

Figure 7.1: Absorbance as a function of wavelength for NaCl solutions measured over a distance of 1cm[76]. Normal saline contains approximately 0.15 molL^{-}1 of NaCl.

the difference in bactericidal efficacy was determined to be negligible. It has to be noted that the treatments were performed on polyethylene strips rather than in a liquid medium. Additionally, VUV with a wavelength smaller than 180 nm is completely absorbed by liquid layers which are thicker than 100 μm[78]. As such, in the treatments discussed in this work, any effect of VUV on bactericidal efficacy is due to the production of chemicals in the absorption region and the resulting effect on the fluid chemistry.

Previous research into the bactericidal effect of UV sterilization by gas discharge lamps shows that a 1 log reduction in bacterial density is achieved after 40 seconds of treatment in the case of Pseudomonas aeruginosa and 54 seconds of treatment for Staphylococcus aureus using a low-pressure mercury lamp with an irradiance of 1 W/m^2 on an initial population of 10^6 CFU/ml[79]. In this case the bacteria are treated in 2- or 15-ml amounts of suspension in which a 10 mm diameter opening was exposed to the UV radiation. Low pressure mercury lamps mainly emit at a wavelength of approximately 254 nm (UVC) and are often used as bactericidal lamps as it is know that the absorption cross-section of DNA is known to be high at this wavelength[80].

Fernández et al.[81] investigated the effects of UVA on Pseudomonas aeruginosa using a black light lamp, which has the highest emission at 365 nm with an irradiance of 44 W/m^2. The bacteria were treated in glass chambers with an internal diameter of 4.6 cm. The irradiation resulted in a 1 log reduction after approximately 20 minutes, and a 3 log reduction after 60 minutes. While the bacterial concentration is not stated in the paper, the provided optical density values indicate a concentration of approximately 10^8 CFU/ml.

Soloshenko et al.[82] made a comparison of water decontamination efficiency by using various UV sources such as a cold hollow cathode discharge and low- and medium-pressure mercury lamps. The used bacterium was Escherichia coli. Their results show that bactericidal efficacy of UV is not only dependent on the absorption by DNA but that it also depends on the shape of the radiation spectrum.

The above mentioned low-pressure mercury lamp used a UV-flux of 1W/m^2 at approximately 254 nm. The maximum emission of the plasma jet used in this work in the range of 249 to 259 nm is found in the case of a plate electrode argon plasma (figure 5.14) to be approximately two orders of magnitude lower. Using the ring electrode, the secondary electrode used for treatment of cells and bacteria, the emission in this range is even lower. Because of this the bactericidal effects of UV due to a change of the DNA in cells is not expected to be influential.

According to the ICNIRP guidelines for UV exposure[83], the exposure of the skin and

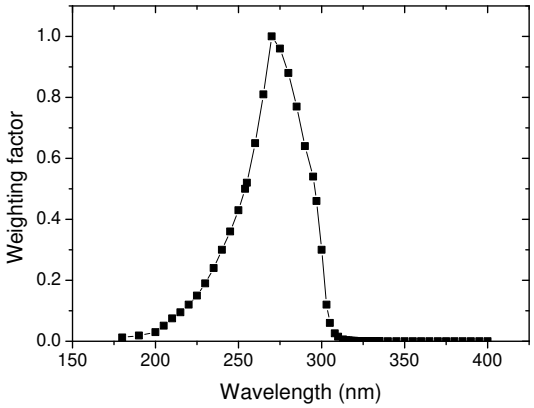

Figure 7.2: Weighting factor as a function of wavelength for UV exposure of skin and eyes[83].

eyes should not exceed 30 Jm^{-2} within an eight hour period. This total energy is weighted according to a weighting factor which is dependent on the wavelength, a graph of which is shown in figure 7.2. The weighting factor is normalized at 270 nm. The exposure limit is set at this value to prevent "sunburn", also called erythema, and limit long-term damage to the skin even for people that normally burn easily. The 30 Jm^{-2} can be applied over various durations, for example 0.001 Wm^{-2} over an eight hour period or 300 Wm^{-2} over a period of 0.1 s. For pulsed exposure, the duration should not be less than 1 µs per pulse for the limit to be valid. For the plasma source presented in this work, which can be pulsed at 20 kHz, this means that the minimum duty cycle for the UV limit to be valid is 2%. As the minimum duty cycle used in this report is 10%, the set limit is valid.

The ICNIRP weighted irradiances are shown in appendix A. The weighted spectra produce a weighted irradiance of approximately 0.03 $\mathrm{W/m}^2$ for situations with the highest UV-fluxes (plate electrode using argon as a carrier gas). As a result the total daily treatment time allowed according to ICNIRP UV-flux guidelines is approximately 20 minutes. As the treatment durations used in this work are typically an order of magnitude less than that, UV production is not expected to pose a problem in clinical practice with this specific plasma jet.

While the bactericidal effect of the produced UV-flux can not be completely excluded, the measured irradiances and the length of the treatment times are expected to be too low to lead to a significant effect. Furthermore, any effect of VUV should be expressed in an induced fluid chemistry.

7.6 Fluid chemistry effects

This section discusses the influence of an influx of radicals on the chemistry in the bulk of the liquid in an attempt to gain insight into the mechanisms of for example nitrite, nitrate and hydrogen peroxide generation as well as to find estimates of chemical species densities possibly responsible for bactericidal effects.

The fluid chemistry induced by the flux of ozone, nitric oxide and hydroxyl radicals impacting the surface of the liquid is calculated as a function of time. This is done by solving a system of 30 coupled differential equations of the form

$$\frac{d\,[A]}{dt} = k_{BC}\,[B]\,[C] - k_{AD}\,[A]\,[D] - ... + ..., \tag{7.6}$$

where $[A]$, $[B]$, $[C]$ and $[D]$ are arbitrary particle concentrations in M and k_{BC} and k_{AD} are second order rate constants for the components mentioned in the subscript in $\mathrm{M}^{-1}\mathrm{s}^{-1}$. A positive term indicates a production of the species $[A]$ whereas a negative term indicates

a destruction of the species. Aside from second order reactions, also first and third order reactions occur, in which case the reaction rate constants are also of first and third order, having units of s^{-1} and $M^{-2}s^{-1}$ respectively.

The used reactions and their respective reaction rates are shown in table 7.1 and are taken from the NDRL/NIST Solution Kinetics Database[84]. The relevant reactions of the components present in and produced by the system are selected to form a self-consistent system of reactions. The starting concentrations of H^+, OH^-, O_2 and Cl^- are taken to be approximately 10^{-7}, 10^{-7}, $3{\cdot}10^{-4}$ and $6{\cdot}10^{-6}$ M respectively. The starting values of OH^- and H^+ are chosen because an initial pH of 7.0 is assumed. The concentration of oxygen in the water is estimated by Henry's law[2]. Nitrogen (either N or N_2) is not a part of the calculations as it is not found to contribute to any reactions. The initial nitrite and nitrate concentrations are defined to be approximately 0.01 and 0.005 mM respectively, as these were the measured concentrations of untreated samples in section 5.5. Finally a nonzero concentration of chloride is used because the (supposedly) distilled water used for the ion chromatography measurements still contained this concentration of chloride, as mentioned in section 5.5. While Na^+ will also be present in the water in similar concentrations, there are no applicable reactions of Na^+ in water in these calculations and as such it is not included. A constant flux of O_3, NO and OH originating from the plasma is assumed, the values of which are determined by using an optimization algorithm to find values at which the end concentrations of nitrate and nitrite correspond to the values found in the experiments shown in figure 5.18c, namely $1 \cdot 10^{-4}$ M of nitrate and $8 \cdot 10^{-6}$ M of nitrite after 60 seconds of treatment using a 1.3W ring electrode plasma. The externally induced production term in the bulk of the liquid of O_3, NO and OH required to achieve the experimentally measured nitrate and nitrite concentrations are found to be approximately $2.9{\cdot}10^{-6}$, $44.5{\cdot}10^{-6}$ and $10.4{\cdot}10^{-6}$ M/s respectively.

Roeselová et al. [85] used molecular dynamics simulations to investigate the interactions of hydroxyl radicals at the air-water interface. A water slab of 30x30x100 Å containing 864 water molecules was used and a single OH radical was placed 15 Å above the surface of the water. A total of 250 trajectories were calculated using initial velocities calculated from the Maxwell-Boltzmann distribution at 300 K. Of these 250 simulations, 81 radicals were absorbed in the bulk whereas 142 radicals were adsorbed at the air-water interface. The rest of the trajectories were either scattered, desorbed or deflected. In the fluid chemistry calculations shown in this work, all of the adsorbed OH radicals are assumed to react to form H_2O_2, leading to a constant production of hydrogen peroxide. As this flux of radicals is treated separately, the requirement on the OH flux more than doubles. While other molecular dynamics simulations[86, 87] show that the propensity to adsorb rather than absorb is also applicable to ozone (10 molecules adsorbed for every molecule absorbed), this effect is not included in the calculations as reaction (5) has a reaction rate which is almost two orders of magnitude lower than reaction (4) and the production term of O_3 is an order of magnitude smaller, as shown before.

Assuming a 1.5 slm ($2.5{\cdot}10^{-5}$ m^3/s) flow, $6.022{\cdot}10^{23}$ particles per mol (Avogadro constant) and a liquid volume of 100 µl an estimation can be made of the minimum required radical density in the gas phase to achieve the bulk chemistry effects assuming an even distribution of radicals in the gas flow. For example for ozone:

$$n_{O_3} = \frac{6.022 \cdot 10^{23} \cdot 100 \cdot 10^{-6} \cdot 2.9 \cdot 10^{-6}}{2.5 \cdot 10^{-5}} \approx 7 \cdot 10^{18} \mathrm{m}^{-3}. \tag{7.7}$$

Similarly for NO and OH the values are $1{\cdot}10^{20}\mathrm{m}^{-3}$ and $3{\cdot}10^{19}\mathrm{m}^{-3}$ respectively. In ppm, the values are approximately 0.3 ppm of ozone, 4 ppm of NO and 1.3 ppm of OH. As the concentration of OH is the concentration required to achieve the bulk chemistry (thus absorbed molecules), the actual required density will be approximately 3.5 ppm due to adsorption.

[2] $p = k_H c$, where p is the partial pressure, k_H is the Henry constant and c is the concentration. For oxygen in water $k_H \approx 769$ atm·M^{-1}.

Reuter et al.[88] measured an ozone concentration of approximately 10 ppm using a commercial argon jet (*kINPen*), while Pipa et al.[89] measured a nitric oxide concentration of approximately 2 ppm using a custom argon jet. OH concentrations have been measured using the *kINPen* to be approximately 1 to 10 ppm, depending on water content and position in the plasma by Mensink[90]. These measurement results show that while the calculated concentration of NO is quite high compared to measurements, the calculated concentrations of OH and O_3 corresponds nicely when taking into account the adsorption effect.

Figure 7.3a shows the concentration in M of various chemical species in the treated water as a function of treatment time on a double log scale. The treatment is limited to 60 seconds to simulate the most used treatment conditions of previous chapters. The behavior of the various concentrations after stopping the plasma treatment is shown in figure 7.3b. A clear distinction is seen between species that act as an intermediate such as O^{2-}, O^-, OH, O_3, HO_2 and NO and stable species such as NO_2^-, NO_3^- and H_2O_2.

As an additional check on the calculated values, the concentrations of H_2O_2, nitrite and nitrate for various treatment durations are calculated and compared to the measured values introduced in section 5.5 and 5.6. The resulting graphs are shown in figure 7.4. The calculated concentration of nitrate as a function of time corresponds quite well to the almost linear measured behavior. Nitrite calculations on the other hand, while showing somewhat different values, do nicely show the observed trend. Also the maximum concentration of nitrite, calculated to be after approximately 20 seconds of treatment, is in good agreement with the measurements. Hydrogen peroxide calculations show a nice agreement for the first 30 seconds of treatment, after which the measured values are significantly higher. The concentration of H_2O_2 is calculated to be 0.3 mM after 60 seconds of treatment. Section 5.6 shows that the measured H_2O_2 concentration after 60 seconds is approximately 0.6 mM, making the calculated value reasonably consistent with the experiments. The main difference is the quadratic behavior of the hydrogen peroxide concentration, probably due to an increase in water concentration over time leading to an increased production of OH, as explained in section 5.6. In the calculations on the other hand, a constant production of OH is assumed. The first order components in both fits shown in figure 7.4b are comparable however, being $1.44 \cdot 10^{-3}$ mMs^{-1} in the measurements and $5.13 \cdot 10^{-3}$ mMs^{-1} in the calculations. The discrepancies between measurements and calculations of NO_2^- and NO_3^- might be because of slightly different reaction rates or smaller reaction rates which are not included in the calculations. Although there are differences between the measurements and the calculations, these graphs provide an indication that the calculated fluid chemistry is accurate and yields correct order of magnitude concentrations.

The pH level after treatment is 3.7 while the measured value shown in figure 5.20 is approximately 4.1 for distilled water. The reason for this discrepancy might be the fact that in the calculations the pH of the solution has no effect on the reaction rates apart from reactions in which H^+ is a reactant. As a result for example a simultaneous increase of OH^- and H^+ is possible in these calculations.

It is interesting to note that the above assumed surface production of hydrogen peroxide by recombination of OH radicals adsorbed at the water-air interface is essential to achieve the measured concentrations. When this surface production term is not included in the calculations, a hydrogen peroxide concentration of approximately $3.8{\cdot}10^{-8}$ mM is calculated, an underestimation of almost seven orders of magnitude. Aside from surface production of H_2O_2, formation of hydrogen peroxide in the gas phase (by reactions of OH with itself) can also result in an extra production term. However, a significant flux of OH still has to reach the bulk of the liquid to induce the chemistry observed in treatments. Because of this, surface production of OH is still an important factor.

In the remainder of this section the possible (unstable) bactericidal components and their concentrations and consecutive reactions are reviewed. At the end of the section the concentrations required to achieve bactericidal effects found in literature are summarized in table 7.2.

Reaction number	Reaction	Reaction rate ($M^{-1}s^{-1}$)
1	$OH + NO \rightarrow NO_2^- + H^+$	$1 \cdot 10^{10}$
2	$OH + NO_2^- \rightarrow OH^- + NO_2$	$1 \cdot 10^{10}$
3	$O_3 + NO_2^- \rightarrow O_2 + NO_3^-$	$2.5 \cdot 10^5$
4	$OH + OH \rightarrow H_2O_2$	$5 \cdot 10^9$
5	$OH + O_3 \rightarrow O_2 + HO_2$	$1 \cdot 10^8$
6	$OH + HO_2 \rightarrow O_2 + H_2O$	$7.5 \cdot 10^9$
7	$HO_2 + HO_2 \rightarrow O_2 + H_2O_2$	$1 \cdot 10^6$
8	$HO_2 + NO \rightarrow HO_2NO$	$3.2 \cdot 10^9$
9	$OH + OH^- \rightarrow H_2O + O^-$	$1.3 \cdot 10^{10}$
10	$NO_2^- + O^- \rightarrow OH^- + NO_2$	$3 \cdot 10^8$
11	$NO_2 + NO \rightarrow N_2O_3$	$1.1 \cdot 10^9$
12	$NO + NO + O_2 \rightarrow NO_2 + NO_2$	$2.3 \cdot 10^{6*}$
13	$OH + Cl^- \rightarrow ClOH^-$	$3.5 \cdot 10^9$
14	$ClOH^- + Cl^- \rightarrow OH^- + Cl_2^-$	$1 \cdot 10^4$
15	$Cl_2^- + Cl_2^- \rightarrow Cl_3^- + Cl^-$	$4 \cdot 10^9$
16	$OH^- + Cl_2^- \rightarrow ClOH^- + Cl^-$	$4.5 \cdot 10^7$
17	$NO_2^- + Cl_2^- \rightarrow Cl^- + Cl^- + NO_2$	$2.5 \cdot 10^8$
18	$H_2O + NO_2 + NO \rightarrow HNO_2 + HNO_2$	$2 \cdot 10^8$
19	$H_2O + NO_2 + NO_2 \rightarrow NO_2^- + NO_3^- + H^+ + H^+$	$0.5 \cdot 10^8$
20	$H_2O + NO_2 + NO_2 \rightarrow HNO_2 + NO_3^- + H^+$	$1.5 \cdot 10^8$
21	$H_2O_2 + OH \rightarrow H_2O + O_2^-$	$2.7 \cdot 10^7$
22	$O_2^- + NO \rightarrow ONO_2^-$	$5 \cdot 10^9$
23	$O_2^- + O_3 \rightarrow O_2 + O_3^-$	$1.6 \cdot 10^9$
24	$O_3^- + H^+ \rightarrow HO_3$	$5.2 \cdot 10^{10}$
25	$O_3^- + H^+ \rightarrow O_2 + OH$	$9 \cdot 10^{10}$
26	$O_3^- + OH \rightarrow HO_2 + O_2^-$	$8.5 \cdot 10^9$
27	$O^- + O_3^- \rightarrow O_4^{2-}$	$7 \cdot 10^8$
28	$O_3^- \rightarrow O_2 + O^-$	$5 \cdot 10^{3**}$
29	$O^- + O_3^- \rightarrow O_2^- + O_2^-$	$7 \cdot 10^8$
30	$H_2O + HO_2 + O_2^- \rightarrow O_2 + H_2O_2 + OH^-$	$9.7 \cdot 10^7$

Table 7.1: Reactions and reaction rates used in fluid chemistry calculations. *: Third order reaction rate, ($M^{-2}s^{-1}$). **: First order reaction rate, (s^{-1}). Reactions and reaction rates are taken from [84].

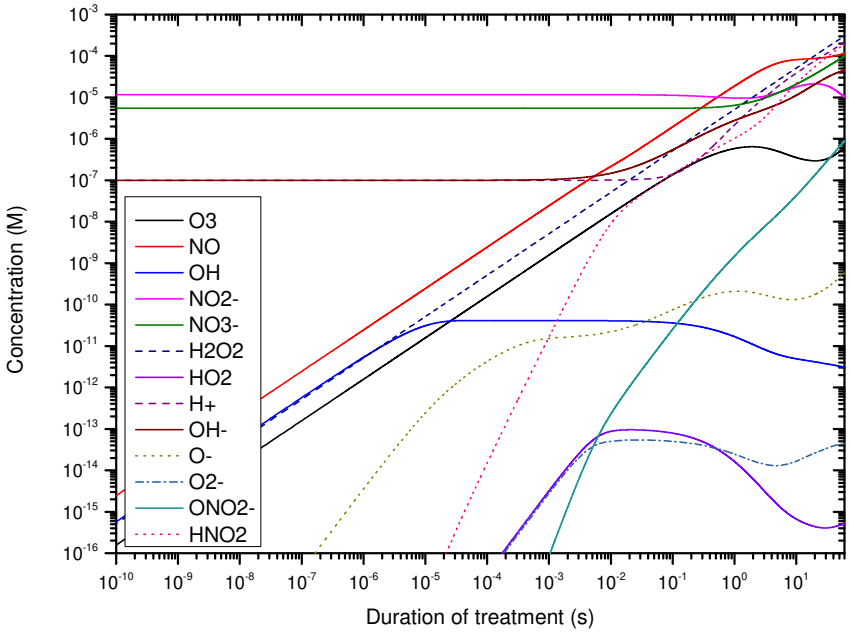

(a) During plasma treatment

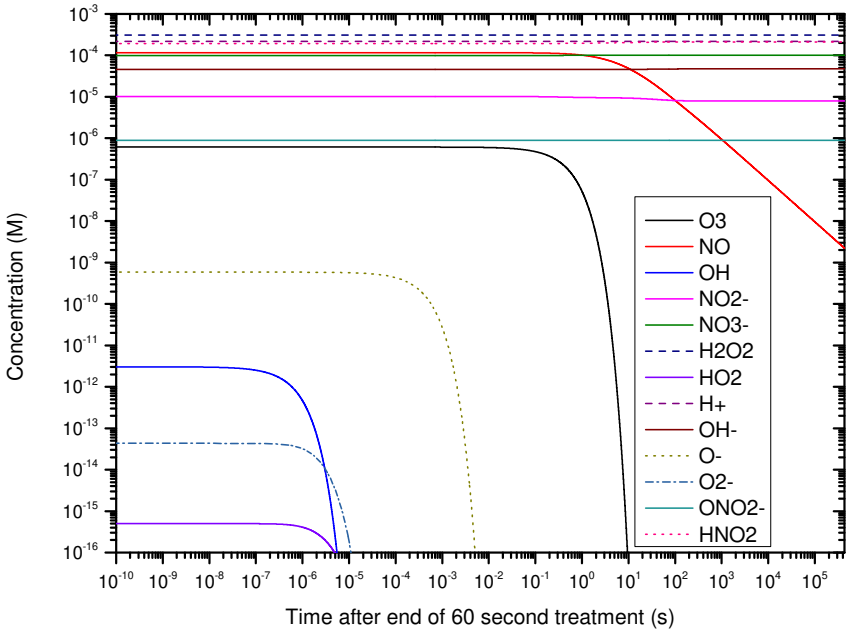

(b) After 60 second plasma treatment

Figure 7.3: Calculated concentrations of various chemical species in water as a function of treatment time and as a function of elapsed time after applying a 60 second plasma treatment.

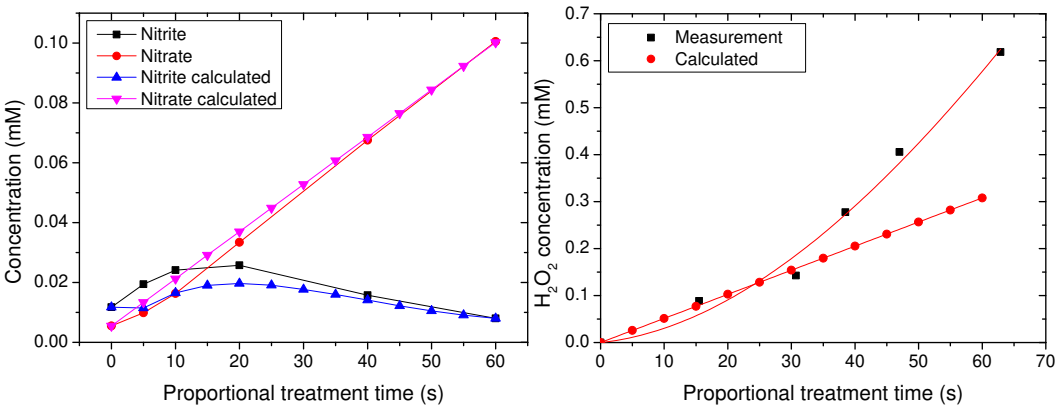

(a) Nitrite and nitrate (b) H_2O_2

Figure 7.4: Comparison between calculations and measurements of H_2O_2, nitrite and nitrate concentrations as a function of treatment time. In the hydrogen peroxide figure, a third order fit of the function $[H_2O_2](t) = -4.68 \cdot 10^{-7}t^3 + 0.165 \cdot 10^{-3}t^2 + 1.44 \cdot 10^{-3}t$ mM is shown in red for the measurement data and a linear fit of $[H_2O_2](t) = 5.13 \cdot 10^{-3}t$ mM is shown in red for the calculated data. Both of the fitted functions have a fixed intercept at a concentration of 0 mM.

7.6.1 Peroxynitrous acid

Peroxynitrite ($ONOO^-$) manifests as being a stable species in the chemistry calculations while in reality this is not the case. This is because $ONOO^-$ is converted into peroxynitrous acid by the pH dependent reaction

$$ONOO^- + H^+ \rightleftarrows ONOOH, \tag{7.8}$$

a reaction which is dependent on pH level. The concentration of peroxynitrite as a function of time is given by[91]

$$\left[ONOO^-\right]_t = \left[ONOO^-\right]_0 e^{-kt}, \tag{7.9}$$

where $[ONOO^-]_t$ and $[ONOO^-]_0$ denote the concentration of peroxynitrite as a function of time and the initial concentration respectively. k is the pH and solvent dependent rate constant for the decomposition of peroxynitrite, which is approximately 0.64 s^{-1} at a pH of 7.4 and 4 s^{-1} at a pH of 5.0 where all peroxynitrite is converted into peroxynitrous acid. This results in the half-life of $ONOO^-$ being approximately 1 second in an environment with a pH of 7.4 and 0.2 seconds in a solution with a pH of 5. Because of this, the actual concentration of $ONOO^-$ in the solution after treatment is expected to be negligible, as all of it is converted into peroxynitrous acid, which decomposes via [92]

$$ONOOH \rightarrow f_1 (OH + NO_2) + (1 - f_1)\left(NO_3^- + H^+\right) \tag{7.10}$$

The value of f_1 is generally thought to be $\geq$0.1[93], whereas Coddington et al.[94] proposes the reaction

$$ONOOH \rightarrow f_2 (OH + NO_2) + (1 - f_2)(HNO_3) \tag{7.11}$$

where $f_2 = 0.29$ and is deduced from measurements of the formed oxidizing intermediate. The reason for low values of f is that the reaction products of the decomposition of ONOOH rapidly react with each other. Other possible reactions are [95]:

$$ONOOH \rightarrow NO_2^+ + OH^- \tag{7.12}$$

$$ONOOH \rightarrow NO^+ + OOH^- \tag{7.13}$$

$$\mathrm{ONOOH} \rightarrow {}^1\mathrm{O}_2 + \mathrm{HNO} \tag{7.14}$$

Producing among others OH^-, nitroxyl (HNO) and singlet oxygen $^1O_2$. The production of singlet oxygen by reaction 7.14 however is calculated to be at least 23 orders of magnitude lower than the production of OH and NO_2 in reaction 7.10[96].

The bactericidal effect of peroxynitrite and its conjugate acid peroxynitrous acid are known from literature to be significant. Peroxynitrite is particularly toxic to cells due to its ability to diffuse through several cell diameters and cell walls before reacting. It is also able to initiate lipid peroxidation, causing cell wall damage[91]. ONOOH is a strong oxidant which reacts with biological molecules through various mechanisms. It is most efficient at oxidizing zinc fingers, protein thiols and iron/sulfur centers and it produces products that are normally expected of OH reactions[97]. Zhu et al.[91] found that the bactericidal effect of peroxynitrite and peroxynitrous acid depends strongly on fluid pH level. A 4 log reduction of E. coli was achieved by adding 1 mM of $ONOO^-$ in a solution with a pH of approximately 7.5. At a pH lower than 7.0 however, a reduction of barely one order of magnitude was achieved. This can be explained by the fact that even though the neutral peroxynitrous acid has the ability to travel through cell membranes and enter cells, where the pH is around 7.0, the resulting $ONOO^-$ reacts rapidly with CO_2 present inside the cells via [98]

$$\mathrm{ONOO^-} + \mathrm{CO_2} \rightarrow \mathrm{ONOOCO_2^-}, \tag{7.15}$$

which has a lifetime of approximately 1μs and spontaneously decomposes:

$$\mathrm{ONOOCO_2^-} \rightarrow \mathrm{CO_3^-} + \mathrm{NO_2}. \tag{7.16}$$

However, 65% of these radicals recombine immediately forming nitrate and carbon dioxide, resulting in only 35% being able to react with other molecules.

It has to be noted that the calculated maximum concentration of $ONOO^-$ (or ONOOH, depending on pH level) is approximately 1μM. As a result, the production of these species might result in a slight bactericidal effect at the beginning of the plasma treatment when the pH is high enough, and an insignificant bactericidal effect at a pH below 7.0. Also, the need for a high pH seems to directly contradict the observed increase of bactericidal effect at low pH values as observed in this work.

Conflicting views seem to exist on the actual decomposition reactions of peroxynitrous acid. The reactions shown above give a representation of reactions commonly found in literature. As reaction rates of these reactions are not known or are pH dependent they are not included in the calculations.

7.6.2 Nitrous acid

Another seemingly stable component, HNO_2 or nitrous acid, in actuality decomposes when in contact with hydrogen peroxide [99]:

$$\mathrm{H_2O_2} + \mathrm{HNO_2} \rightarrow \mathrm{HNO_3} + \mathrm{H_2O}, \tag{7.17}$$

forming nitric acid. Alternatively, it can react as [100]

$$\mathrm{HNO_2} + \mathrm{H^+} \rightleftarrows \mathrm{NO^+} + \mathrm{H_2O} \tag{7.18}$$

$$\mathrm{NO^+} + \mathrm{H_2O_2} \rightarrow \mathrm{ONOOH} + \mathrm{H^+}(\mathrm{slow}) \tag{7.19}$$

Another possible reaction is [92]

$$2\mathrm{HNO_2} \rightleftarrows \mathrm{NO} + \mathrm{NO_2} + \mathrm{H_2O}, \tag{7.20}$$

where the forward rate is 13.4 $M^{-1}s^{-1}$[101] and the reverse rate is $1.1 \cdot 10^9$ $M^{-1}s^{-1}$. Note that the reverse rate is incorporated in the calculations, whereas the forward rate is not. After this reaction, nitrogen dioxide reacts via

$$2\mathrm{NO_2} + \mathrm{H_2O} \rightarrow \mathrm{H^+} + \mathrm{NO_3^-} + \mathrm{HNO_2}, \tag{7.21}$$

forming nitrate and nitrous acid. The result is a slight increase of nitrate concentration and a decrease of nitrous acid concentration over long periods of time. Due to the pH dependent reaction between HNO_2 and NO_2^-, a decrease in nitrous acid results in a similar reduction in nitrite at the same pH value. Because of the additional production of H^+ in reaction 7.21, the effect is even more pronounced as more of the nitrite in the solution is 'stored' as HNO_2. This explains the timescale and underlying mechanism of reduction in nitrite and increase in nitrate concentration after 5 days of storage, as shown in figure 5.18.

The generated NO_2 in reaction 7.10 can also be used to produce nitrous and nitric acid via [100]

$$2NO_2+H_2O \rightarrow HNO_3+HNO_2. \tag{7.22}$$

Alternatively, nitric acid is produced by the reaction [99]

$$OH + NO_2 \rightarrow HNO_3. \tag{7.23}$$

However, in an acidic environment, nitrite is protonated to form nitrous acid:

$$NO_2^- + H^+ \rightleftarrows HNO_2, \tag{7.24}$$

and it also forms due to the reaction of N_2O_3 with water (N_2O_3 is another unstable species) via

$$H_2O+N_2O_3 \rightarrow 2HNO_2, \tag{7.25}$$

making the potential maximum concentration of nitrous acid approximately 1.3 mM when the calculated concentrations of HNO_2 and N_2O_3 and NO_2^- are added up (one N_2O_3 molecule resulting in two HNO_2 molecules).

Both nitric acid (HNO_3) and nitrous acid (HNO_2) have bactericidal properties. Nitrous acid is found to result in a 3 log reduction of E. coli at a concentration of 0.02 mM and a 7 log reduction at a concentration of 0.2 mM at a pH of 3.3[102]. Even though the exact pathways of the decomposition of nitrous acid are unclear, the found values provide an indication that the bactericidal effect of plasma treatment is partly related to the toxicity of nitrous acid. The fact that a decrease in pH results in higher values of nitrous acid and therefore an increased bactericidal effect also provides a possible explanation for the pH dependence found in treatment of bacteria in this work.

7.6.3 Hydrogen peroxide

H_2O_2 can be a bactericidal agent provided the concentrations are high enough. At lower concentrations it may inhibit growth if the concentration is higher than the so-called minimum inhibitory concentration (MIC) [103]. The minimum inhibitory and bactericidal concentration vary per bacterium, and the difference between the two might be small.

Another important aspect of H_2O_2 in contact with bacteria is that some bacteria are less susceptible to its effects when they were starved before treatment by being placed in a nutrition free solution (for example saline). Due to a decrease in cell metabolism, the bactericidal effect of hydrogen peroxide decreases. For Peptostreptococcus anaerobicus this effect is already visible after approximately 20 minutes of starvation[104].

7.6.4 Ozone

The bactericidal effects of ozone have been known for many years. When dissolved in a solution, it slowly decomposes to oxygen with a half-life of approximately 20 to 30 minutes in distilled water[105]. Ozone can react with and oxidize an organic compound either directly, or via a radical intermediate such as OH^-. In acidic solutions, O_3 is more stable than in alkali solutions. As a result, the dominant deactivation mechanism in acidic solutions is direct interaction of the molecule with cells. An added advantage of low liquid pH is the increase in solubility of ozone. The concentration of O_3 in water in an equilibrium situation

is approximately 1.3 times higher at a pH of 4.0 than at a pH of 7.0[106]. However, as the concentration of ozone in the solution decreases rapidly after approximately 0.1 s after stopping plasma treatment because it reacts with nitrite, the effect of ozone does not explain any residual bactericidal efficacy after plasma treatment.

7.6.5 Superoxide

Previous research has shown indications of the influence of $O2^-$ on bactericidal efficacy[107, 108, 109]. It reacts as

$$HO_2 \rightleftarrows H^+ + O_2^-, \tag{7.26}$$

depending on pH. The reaction thought to be responsible for its toxic effect is the so-called Haber-Weiss reaction [110]

$$O_2^- + H_2O_2 \rightarrow OH + OH^- + O_2, \tag{7.27}$$

which forms OH and is thought to release oxygen in its singlet state in some cases[111]. However, normally the Haber-Weiss reaction does not occur without a catalyst such as Fe^{3+}. It is suggested however that the process can still take place on the cell surface, which also allows for the resulting radicals to react with the cells before they decompose[112].

While quantification of the concentrations needed to achieve bactericidal effect is difficult, superoxide is not assumed to be a contributing factor in the treatments shown in this work because of the low concentrations (HO_2 and O_2^- together constitute approximately 10^{-13} M) and the tendency to form HO_2 in stead of superoxide at low pH levels. Also, most cells contain superoxide dismutases[3], resulting in a conversion to oxygen and hydrogen peroxide. So while its neutral molecule HO_2 has the ability to penetrate cell membranes, it is rapidly converted by these superoxide dismutases[113].

As mentioned before, the maximum expected concentrations and the concentrations at which the individual components are bactericidal is shown in table 7.2.

7.6.6 Hypochlorous acid

Another possible inactivation mechanism can be of importance especially in saline or PBS solutions, namely hypochlorous acid production via [127]

$$H_2O_2 + H^+ + Cl^- \rightarrow HOCl + H_2O \tag{7.28}$$

$$HOCl \rightleftarrows H^+ + OCl^- \tag{7.29}$$

HOCl and OCl^- are commonly called free chlorine and are highly bactericidal. HOCl is dominant in a pH range of 3.5 to 5.5, OCl^- predominates above a pH of 8 and in between the two exist in various proportions[128]. Another possible production term is electrolysis using the chloride ions in the solution. An example of the bactericidal effect of among others chlorine on PAO1 is shown in figure 7.5. The log reduction in the concentration of bacteria is shown as a function of CT (concentration times treatment time). However, as similar bactericidal effects in distilled water and saline are shown in this work and the concentration of chloride did not change as a function of treatment time in the ion chromatography measurements, this is not expected to be a dominant contribution. Also, electrolysis is not expected as the plasma is not in contact with the liquid during treatment.

7.6.7 Buffered solutions

The above calculations assume a non-buffered solution. A buffer in a solution has the ability to bind H^+ ions reversibly through the reaction

$$\text{Buffer} + H^+ \rightleftarrows \text{HBuffer}. \tag{7.30}$$

[3]Enzymes that catalyze the dismutation of superoxide.

Species	Maximum expected concentration (mM)	Concentration at which bactericidal (mM)	References
$ONOO^-$	0.009 (at high pH)	0.01 (pH 8.4) - 0.250 (pH 7.0)	[91, 114]
ONOOH	Unstable, can form NO_2 and OH (at low pH)		
HNO_2	1.2 (at low pH)	0.2 (pH 3.3) - 30 (pH 5.0)	[92, 102]
H_2O_2	0.3 (calculated) 0.7 (measured)	60 - 83 0.15 (pH 5.0) - 28, MIC	[115, 116] [117, 118, 119, 103]
O_3	0.0006	0.0046 to 0.1	[120, 116, 121, 122, 105, 123]
O_2^-	10^{-10} (at high pH) Can form OH and OH^- on cell surface	1 (order of magnitude estimation)	[110]
HO_2	10^{-10} (at low pH)	Rapidly converted by superoxide dismutases	[113]
OH	$4{\cdot}10^{-8}$ (maximum in bulk during treatment)	0.05	[124]
NO	0.1 Approximately 4 ppm in gas phase	40-200 ppm in gas phase	[125, 126]

Table 7.2: Concentrations of various chemical species found in calculations and measurements and their respective concentrations needed to achieve bactericidal effects in literature. All values are given in mM and are not specific for Pseudomonas aeruginosa or Staphylococcus aureus but are provided as an order of magnitude impression of the bactericidal effect of the individual components. MIC denotes the minimum inhibitory concentration, meaning the minimum concentration that will inhibit visible overnight growth of the bacterium.

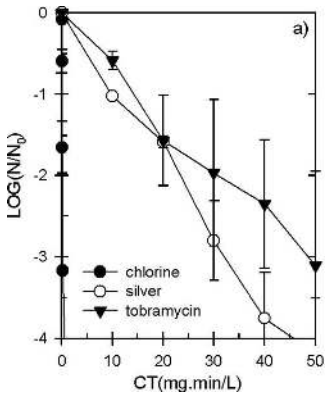

Figure 7.5: Effect of chlorine, silver and tobramycin on PAO1. For the chlorine data points, the results for 1 mg/liter and 10 mg/liter were averaged. Log reduction of bacterial concentration as a function of concentration times treatment time[129].

In the human body, an example of a buffer system is the bicarbonate buffer system, which consists of a weak acid H_2CO_3 and a bicarbonate salt, for example $NaHCO_3$. The weak acid is produced in the body by the reaction of CO_2 with H_2O using carbonic anhydrase[4] as a catalyst:

$$CO_2 + H_2O \rightleftarrows H_2CO_3. \tag{7.31}$$

H_2CO_3 in turn ionizes weakly and thereby produces low concentrations of H^+ and HCO_3^-:

$$H_2CO_3 \rightleftarrows H^+ + HCO_3^-, \tag{7.32}$$

However, the reverse reaction is dominant in this case. The bicarbonate salt ionizes almost completely and thereby forms HCO_3^- and Na^+,

$$NaHCO_3 \rightleftarrows Na^+ + HCO_3^-. \tag{7.33}$$

While this reaction is reversible, the reaction balance greatly favors the formation of ions. The complete system becomes

$$CO_2 + H_2O \rightleftarrows H^+ + H_2CO_3 \rightleftarrows H^+ + HCO_3^- + Na^+ \tag{7.34}$$

If a strong acid such as HCl is added, the increased level of H^+ is buffered by the HCO_3^- by

$$\uparrow H^+ + HCO_3^- \rightarrow H_2CO_3 \rightarrow CO_2 + H_2O, \tag{7.35}$$

resulting in a decrease in H^+ and an increase in CO_2 levels in the body. The excess of CO_2 is eliminated by the respiration system. Conversely, if a base such as NaOH is introduced:

$$NaOH + H_2CO_3 \rightarrow NaHCO_3 + H_2O, \tag{7.36}$$

in which the strong base NaOH is replaced by a weak base $NaHCO_3$.

The capacity of a solution to act as a buffer depends on the ratio of concentrations of the weak acid (H_2CO_3) and HCO_3^-:

$$\left[H^+\right] = K\frac{\left[H_2CO_3\right]}{\left[HCO_3^-\right]}, \tag{7.37}$$

where K is the dissociation constant which is also written in log form:

$$pK = -\log K. \tag{7.38}$$

[4]Carbonic anhydrases are a family of enzymes dedicated to the catalysis of reaction 7.31 to help maintain acid-base balance in the human body.

In other words, K defines the ratio of the concentration of the acid and its dissociated ions. As a result, the pH of a solution is given by

$$\mathrm{pH} = \mathrm{pK} + \log \frac{\left[\mathrm{HCO_3^-}\right]}{\left[\mathrm{H_2CO_3}\right]}. \tag{7.39}$$

In this reaction, pK=6.1. When a strong base is introduced, the result is a decrease in concentration of H_2CO_3, which in turn causes a slightly higher pH value, whereas introducing an acid results in a slightly lower pH. However, both these effects are mitigated by the presence of the buffer components. If the ration of the concentrations of the buffer components is unity, the pH level is equal to the pK level. In this region, the buffer solution has the highest buffer capacity: adding an acid or a base results in only a slight pH change. However, when large amounts of acids or bases are added, the buffer capacity will at some point be depleted and a rapid change of pH will occur.

Another example of a pH buffer in the human body is the phosphate buffer system. The most important components in this system are $H_2PO_4^-$ and HPO_4^{2-}. When a strong acid such as HCl is introduced, it is converted to a weak acid by

$$\mathrm{HCl} + \mathrm{Na_2HPO_4} \rightarrow \mathrm{NaH_2PO_4}{+}\mathrm{NaCl}, \tag{7.40}$$

where NaH_2PO_4 is the resulting weak acid. If however a strong base such as OH is added, it will be converted to the weak base $Na_2HPO_4{+}H_2O$ by

$$\mathrm{NaOH} + \mathrm{NaH_2PO_4} \rightarrow \mathrm{Na_2HPO_4}{+}\mathrm{H_2O}. \tag{7.41}$$

This mechanism is comparable to the buffer mechanism in PBS, the difference is that KH_2PO_4 is used in stead of NaH_2PO_4.

The buffer capacity of a solution is defined as

$$\beta(\mathrm{pH}) = \frac{\mathrm{dn}}{\mathrm{dpH}}, \tag{7.42}$$

in units of $\mathrm{mEqL^{-1}pH^{-1}}$. d$n$ denotes an infinitesimal amount of added base. For elements with a valence of one this corresponds to $\mathrm{mmolL^{-1}}$. β is a function of the pH of the solution and is at a maximum if pH=pK. The buffer behavior of three different solutions used in this report are shown in figure 7.6a. The horizontal axis shows the pH value whereas the vertical axis shows the amount of added acid in $\mathrm{mEq\ ml^{-1}}$. As is shown in section 6.1.3, plasma treatment of bacteria is less effective in buffered solutions. In a practical situation, a wound might be covered with wound fluid. This fluid, when optically clear, mostly consists of blood plasma. The buffer behavior of various blood constituents is shown in figure 7.6b. It shows that blood plasma exhibits a higher tolerance for added acid and therefore has an increased buffer capacity compared to PBS and NaAc solutions. For blood and blood plasma, the values of β are approximately 39 $\mathrm{mEqL^{-1}pH^{-1}}$ and 16 $\mathrm{mEqL^{-1}pH^{-1}}$ respectively at a pH of approximately 7. As a comparison, the buffer capacities at a pH of 7 of PBS, 9.4 mM NaAc and 150 mM NaAc are 6.6, 1.9 and 0.1 $\mathrm{mEqL^{-1}pH^{-1}}$ respectively.

More information on the acid-base balance in the human body can be found in for example McNamara and Worthley[131, 132] or Guyton and Hall[133].

Because of the pH stabilizing behavior of buffer solutions, the plasma induced chemistry in these solutions is different. Aside from possible extra chemical reactions occurring due to the added components, the lack of pH change results in higher concentrations of peroxynitrite and superoxide, but lower concentrations of nitrous acid. Also the decomposition of peroxynitrous acid at low pH values results in an increase of NO_2 and OH, which is less common at higher pH values. The growth inhibitory effect of hydrogen peroxide is also expected to be less at higher pH values[119]. Finally, as stated before the solubility of ozone decreases at higher pH, leading to a lower concentration in the bulk. While there might be added effects because of other chemical interactions with the buffer constituents, these effects are not expected to have a large influence as similar bactericidal effects (or lack thereof) were found using different buffer solutions.

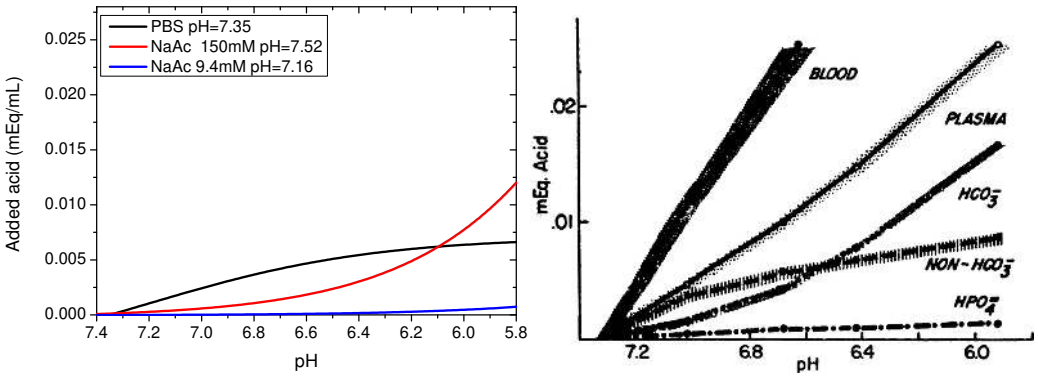

(a) PBS, NaAc

(b) Blood components, 1ml[130]

Figure 7.6: Comparison of the buffer behavior of blood, blood plasma and the used buffer solutions NaAc and PBS.

7.6.8 "Fluid effect"

Another property of plasma treated solutions is their observed bactericidal efficacy even after treatment of solutions. The effect is most dominantly seen in figure 6.8b. As the bactericidal effect decreases quite rapidly after treatment, the difference is caused by the decomposition of non stable species formed during plasma treatment.

The lasting bactericidal effect of plasma treated solutions has previously been studied by among others Naïtali et al.[134]. They used a gliding arc discharge (Glidarc) to treat 20 ml of sterile distilled water for 5 minutes. The result was dubbed 'plasma activated water' (PAW). The water had a pH of approximately 3.0, contained H_2O_2 as well as nitrate and nitrites and it was used to treat the Hafnia alvei bacterium. The effects of the PAW were compared to among others acidified water (with a pH of 3.0, attained by adding HCl), acidified H_2O_2, acidified NO_2^-, acidified NO_3^- and combinations thereof. A solution containing all these elements was closest to the bactericidal effect of 'plasma activated water', but the plasma treated water still seems more effective. A reason for this effect could be related to the fact that because NO_2^- is changed into its neutral form at low pH, the measured concentration of nitrite might not accurately display the actual concentration in the liquid of HNO_2 and NO_2^-. Also, due to the lack of other transient components induced by the plasma might limit symbiotic effects.

Oehmigen et al.[135] also looked at the effects of acidification and modification of the fluid constituents. A high voltage pulsed sinusoidal wave indirect surface DBD with a time averaged plasma power dissipation of approximately 16W was used on solutions containing Staphylococcus aureus and Escherichia coli with concentrations of up to 10^8CFU/ml. A pH decrease as a function of treatment time was detected, the pH of an NaCl solution was observed to decrease from a pH of approximately 7.5 to as low as 2.5 after 30 minutes of treatment of 1.5 ml of solution. Nitrate, nitrite and hydrogen peroxide concentrations were measured as a function of treatment time. All three of these increase as the treatment progresses, the nitrite concentration however initially increases but decreases again after approximately 10 minutes, as also observed in this work. The longest treatment resulted in concentrations of approximately 0.03, 1.8 and 0.6 mM of respectively nitrite, nitrate and hydrogen peroxide. The nitrate concentrations are significantly higher than shown in this work whereas the hydrogen peroxide concentrations are comparable. All these effects are however very dependent on the amount of fluid being treated. These findings seem consistent with those reported by Traylor et al.[136].

This lasting effect is always less effective than direct treatment of bacteria in solution, the differences of which can be ascribed to the lack of transient species in the first case. Also,

other components are unstable over time as described in this section. Finally the bacteria do not experience the pH change in the liquid during treatment, and its associated shift in reaction equilibria. This provides an explanation for both the lasting bactericidal effect and why it diminishes over time.

Chapter 8

Conclusions and recommendations for future research

This chapter will discuss the conclusions that are drawn from the measurements, treatments and calculations. It also provides a set of ideas for future research. It has to be noted that these conclusions are valid for treatments of bacteria and cells in solution. Treatment efficacy of bacteria on surfaces is governed by different inactivation mechanisms than bacteria in liquid, such as for example sputtering and therefore the two are not comparable.

In summary, an atmospheric pressure plasma jet was investigated using diagnostics of power, gas temperature, UV-flux, ion production, as well as induced liquid chemistry. Treatments of the bacteria Pseudomonas aeruginosa, Staphylococcus aureus and the human cells fibroblasts and keratinocytes were performed and the effects on deactivation of bacteria and cell viability were presented. Calculations of the time-dependent fluid chemistry were presented and analyzed and the possible bactericidal effects of various individual chemical components were investigated.

8.1 Conclusions

- Gas temperature and UV-fluxes do not pose a hazard to the human skin, potentially allowing treatments of up to 20 minutes per day with the plasma jet described in this work. As all of the treatments in this work assume a non-touching plasma plume, the effects of direct plasma contact with the skin are not considered.

- The effects of heat, ion- and UV-fluxes, electric fields, and gas flow do not have a prominent direct effect on bacteria inactivation in the treatments performed in this work. Any influence of these components is therefore due to their influence on the liquid chemistry.

- Plasma treatment leads to a pH decrease in non buffered solutions. Acidity of the treated solutions has a significant influence on bactericidal effect; buffered solutions are therefore incomparable to non-buffered solutions. The pH level determines the equilibria of various active chemical species such as peroxynitrite/peroxynitrous acid and nitrous acid but also the solubility of ozone which are shown to be able to play a key role in bacterial inactivation.

- The concentrations of the individual active components (as shown in table 7.2) such as $ONOO^-$, HNO_2 and H_2O_2 are by themselves not sufficient to reach the achieved

bactericidal effect of plasma treatment. A symbiotic effect of some or all of the components is suspected and necessary to explain the strong bactericidal effect of plasma treated solutions.

- Reactive nitrogen species rather than reactive oxygen species play an important role in bacterial inactivation. Exceptions are H_2O_2 and possible local production of OH.
- Keratinocytes and fibroblasts seem less susceptible to plasma treatment than bacteria. For long treatment durations or long incubation in plasma treated solution however, a significant fraction (more than half) of all cells present still die due to plasma treatment. Additionally, fibroblasts seem sensitive to being placed in saline, resulting in a temporarily lowered cell viability due to this incubation alone. Naturally this is a side effect of the in vitro treatments performed.
- In buffered solutions, plasma treatment can lead to inactivation (i.e. no growth) rather than kill. Significant kill in buffered solutions was not observed until depletion of the buffer capacity.
- Plasma treatment can influence growth media and biological detection methods such as LDH release. This is important to consider when choosing biological or chemical diagnostic methods.
- Conditions and liquid media are found which are bactericidal but at the same time preserve a significant fraction of the human cells. However, it should be noted that conditions that are highly bactericidal are also generally detrimental to cell growth, especially after long exposure to the treated liquid.

8.2 Recommendations

- A more extensive characterization of the plasma jet using the mass spectrometry setup should be performed, in which also the neutral particle and radical fluxes are quantified.
- As the observed effects seem fluid chemistry related, an attempt could be made to artificially recreate a solution which contains the observed components. Care has to be taken however in the pH dependency of certain components.
- Additional diagnostics for liquid phase chemistry should be found to further compare the calculations with measurements.
- More treatments of keratinocytes and fibroblasts should be performed with multiple treatments per condition to allow for a sufficient level of statistical analysis and certainty of treatment effects. While this is also true for bacteria, the spread in results obtained in the treatment of cells is much larger, which is in part because of the higher sensitivity of the cells to many external factors but also due to the significantly lower number of cells in any given treatment.
- The effects of plasma on a combination of bacteria and human cells should be performed in a way that simulates an actual wound, for example by using a collagen gel substrate, possibly in combination with wound fluid or (diluted) blood plasma.

Acknowledgements

First and foremost I would like to thank my supervisors Sven, Bouke and Peter for their valuable input on physics and microbiology, as well as for the many informative discussions on either topic and more challenging: both topics combined. Their expert guidance greatly improved the quality of this work.

I would also like to thank Chris for his help with the hydrogen peroxide concentration measurements and Hans Dalderop from the group TPM for performing the ion chromatography measurements. These measurements proved to be an important contribution to the analysis of other measurement results and the validation of the fluid chemistry calculations. Ronny, thanks for your help with performing the initial calibrations and measurements of the mass spectrometer.

Of course I would like to thank our technicians Loek and Ab, without whom the mass spectrometer would certainly not have been finished in time. Huib, for his help in everything related to RF and Evert for his computer related support.

In particular I would like to thank my office mates Rob, Peter, Rogier, Thomas and Kim for providing the necessary distraction from work every now and then but also for providing the opportunity to bounce off ideas. You have been great colleagues.

Finally I would like to thank Gerrit for drawing my attention to this subject and all of the other EPG-colleagues for providing a pleasant working environment, for the countless discussions during lunch time (usually not physics related) and the great atmosphere in general.

Bibliography

[1] E E Tredget, H A Shankowsky, R Rennie, R E Burrell, and S Logsetty. Pseudomonas infections in the thermally injured patient. *Burns*, 30(1):3–26, February 2004.

[2] A T McManus, W F McManus, A D Mason, A R Aitcheson, and B A Pruitt. Microbial colonization in a new intensive care burn unit. *Archives of Surgery*, 120(February):217–223, 1985.

[3] M G Kong, G Kroesen, G Morfill, T Nosenko, T Shimizu, J van Dijk, and J L Zimmermann. Plasma medicine: an introductory review. *New Journal of Physics*, 11(11):115012, November 2009.

[4] J. Heinlin, G. Morfill, M. Landthaler, W. Stolz, G. Isbary, J. L. Zimmermann, T. Shimizu, and S. Karrer. Plasma medicine: possible applications in dermatology. *Journal der Deutschen Dermatologischen Gesellschaft = Journal of the German Society of Dermatology : JDDG*, 8(12):968–76, December 2010.

[5] U. Schnabel, T. Maucher, J. Köhnlein, W. Volkwein, R. Niquet, I. Trick, M. Stieber, M. Müller, H-P. Werner, J. Ehlbeck, C. Oehr, and K-D. Weltmann. Multicentre Trials for Decontamination of Fine-Lumen PTFE Tubes Loaded with Bacterial Endospores by Low and Atmospheric Pressure Plasma. *Plasma Processes and Polymers*, 9(1):37–47, January 2012.

[6] B. Yang, J. Chen, Q. Yu, H. Li, M. Lin, A. Mustapha, L. Hong, and Y. Wang. Oral bacterial deactivation using a low-temperature atmospheric argon plasma brush. *Journal of dentistry*, 39(1):48–56, January 2011.

[7] G B McCombs and M L Darby. New discoveries and directions for medical, dental and dental hygiene research: low temperature atmospheric pressure plasma. *International journal of dental hygiene*, 8(1):10–5, February 2010.

[8] G. Fridman, M. Peddinghaus, M. Balasubramanian, H. Ayan, A. Fridman, A. Gutsol, and A. Brooks. Blood Coagulation and Living Tissue Sterilization by Floating-Electrode Dielectric Barrier Discharge in Air. *Plasma Chemistry and Plasma Processing*, 26(4):425–442, June 2006.

[9] G E Morfill, M G Kong, and J L Zimmermann. Focus on Plasma Medicine. *New Journal of Physics*, 11(11):115011, November 2009.

[10] L.F. Gaunt, C.B. Beggs, and G.E. Georghiou. Bactericidal Action of the Reactive Species Produced by Gas-Discharge Nonthermal Plasma at Atmospheric Pressure: A Review. *IEEE Transactions on Plasma Science*, 34(4):1257–1269, August 2006.

[11] K.-D. Weltmann, E. Kindel, R. Brandenburg, C. Meyer, R. Bussiahn, C. Wilke, and T. von Woedtke. Atmospheric Pressure Plasma Jet for Medical Therapy: Plasma Parameters and Risk Estimation. *Contributions to Plasma Physics*, 49(9):631–640, November 2009.

[12] H Y Cho, A E Yousef, and S K Sastry. Kinetics of inactivation of Bacillus subtilis spores by continuous or intermittent ohmic and conventional heating. *Biotechnology and bioengineering*, 62(3):368–72, February 1999.

[13] A. Fridman. *Plasma Chemistry*. Cambridge University Press, 2008.

[14] T von Woedtke, A Kramer, and K-d. Weltmann. Plasma Sterilization: What are the Conditions to Meet this Claim? *Plasma Processes and Polymers*, 5(6):534–539, August 2008.

[15] T. von Woedtke and A. Kramer. The limits of sterility assurance. *GMS Krankenhaushygiene interdisziplinär*, 3(3):Doc19, January 2008.

[16] S Kalghatgi, D Dobrynin, G Fridman, M Cooper, G Nagaraj, L Peddinghaus, M Balasubramanian, K Barbee, A Brooks, V Vasilets, A Gutsol, A Fridman, and G Friedman. Applications of non thermal atmospheric pressure plasma in medicine. In *Plasma Assisted Decontamination of Biological and Chemical Agents*, pages 173–181. 2008.

[17] M. A. Lieberman and A. J. Lichtenberg. *Principles of Plasma Discharges and Materials Processing*. 2005.

[18] J. Park, I. Henins, H. W. Herrmann, and G. S. Selwyn. Gas breakdown in an atmospheric pressure radio-frequency capacitive plasma source. *Journal of Applied Physics*, 89(1):15, 2001.

[19] ICNIRP. *ICNIRP Guidelines for limiting exposure to time-varying electric, magnetic and electromagnetic fields*. 1998.

[20] M. Moravej, X. Yang, G. R. Nowling, J. P. Chang, R. F. Hicks, and S. E. Babayan. Physics of high-pressure helium and argon radio-frequency plasmas. *Journal of Applied Physics*, 96(12):7011, 2004.

[21] H W Lee, G Y Park, Y S Seo, Y H Im, S B Shim, and H J Lee. Modelling of atmospheric pressure plasmas for biomedical applications. *Journal of Physics D: Applied Physics*, 44(5):053001, February 2011.

[22] E Stoffels, I E Kieft, R E J Sladek, L J M Van Den Bedem, E P Van Der Laan, and M Steinbuch. Plasma needle for in vivo medical treatment: recent developments and perspectives. *Plasma Sources Science and Technology*, 15(4):S169–S180, November 2006.

[23] J. L. Walsh and M. G. Kong. Contrasting characteristics of linear-field and cross-field atmospheric plasma jets. *Applied Physics Letters*, 93(11):111501, 2008.

[24] J L Walsh and M G Kong. Linear-field and cross-field cold atmospheric plasma jets. In *ISPC19*, pages 1–4, 2009.

[25] T. Burns, S. Breathnach, N. Cox, and C. Griffiths, editors. *Rook's Textbook of Dermatology*. Blackwell Publishing Ltd., 8th edition, 2010.

[26] J J Grzesiak and M D Pierschbacher. Shifts in the concentrations of magnesium and calcium in early porcine and rat wound fluids activate the cell migratory response. *The Journal of clinical investigation*, 95(1):227–33, January 1995.

[27] C. M. Illingworth and A.T. Barker. Measurement of electrical currents emerging during the regeneration of amputated finger tips in children. *Clin. Phys. Physiol. Meas.*, 1(1):87–89, 1980.

[28] K S Fang, B Farboud, R Nuccitelli, and R R Isseroff. Migration of human keratinocytes in electric fields requires growth factors and extracellular calcium. *The Journal of investigative dermatology*, 111(5):751–6, November 1998.

[29] Y. Sarret, D. T. Woodley, K. Grigsby, K. Wynn, and E. J. O'Keefe. Human keratinocyte locomotion: the effect of selected cytokines. *The Journal of investigative dermatology*, 98(1):12–16, 1992.

[30] L Mori, A Bellini, Martin A Stacey, M Schmidt, and S Mattoli. Fibrocytes contribute to the myofibroblast population in wounded skin and originate from the bone marrow. *Experimental cell research*, 304(1):81–90, March 2005.

[31] A. J. Singer and R. A. F. Clark. Cutaneous Wound Healing. *The New England Journal of Medicine*, 341(10):738–746, 1999.

[32] P Shakespeare. Burn wound healing and skin substitutes. *Burns : journal of the International Society for Burn Injuries*, 27(5):517–22, August 2001.

[33] D. Church, S. Elsayed, O. Reid, B. Winston, and R. Lindsay. Burn Wound Infections. *Clinical Microbiology Reviews*, 19(2):403–434, 2006.

[34] J Weber and A McManus. Infection control in burn patients. *Burns : journal of the International Society for Burn Injuries*, 30(8):A16–24, December 2004.

[35] E. C. Loebl, J. A. Marvin, E. L. Heck, W. Curreri, and C. R. Baxter. The Use of Quantitative Monitoring Biopsy Cultures in Bacteriologic of Burn Patients. *Journal of Surgical Research*, 16:1–5, 1974.

[36] M Ip, S L Lui, V K M Poon, I Lung, and A Burd. Antimicrobial activities of silver dressings: an in vitro comparison. *Journal of medical microbiology*, 55(Pt 1):59–63, January 2006.

[37] Y. Carmeli, N. Troillet, G. M. Eliopoulos, and M. H. Samore. Emergence of Antibiotic-Resistant Pseudomonas aeruginosa : Comparison of Risks Associated with Different Antipseudomonal Agents. *Antimicrobial agents and chemotherapy*, 43(6):1379–1382, 1999.

[38] J.G. Black. *Microbiology - Principles and Explorations*. Wiley, 2008.

[39] S A Ermolaeva, A F Varfolomeev, M Y Chernukha, D S Yurov, M M Vasiliev, A A Kaminskaya, M M Moisenovich, J M Romanova, A N Murashev, I I Selezneva, T Shimizu, E V Sysolyatina, I A Shaginyan, O F Petrov, E I Mayevsky, Vl Fortov, G E Morfill, Boris S Naroditsky, and A L Gintsburg. Bactericidal effects of non-thermal argon plasma in vitro, in biofilms and in the animal model of infected wounds. *Journal of medical microbiology*, 60(Pt 1):75–83, January 2011.

[40] C K Stover, X.Q. Pham, A L Erwin, S D Mizoguchi, P Warrener, M J Hickey, W O Hufnagle, and D J Kowalik. Complete genome sequence of Pseudomonas aeruginosa PAO1, an opportunistic pathogen. *Nature*, 406(6799):959–64, August 2000.

[41] L. Yang, J. Chen, and J. Gao. Low temperature argon plasma sterilization effect on Pseudomonas aeruginosa and its mechanisms. *Journal of Electrostatics*, 67:646–651, 2009.

[42] R Matthes, S Bekeschus, C Bender, I Koban, N-O. Hübner, and A. Kramer. Pilot-study on the influence of carrier gas and plasma application (open resp . delimited) modifications on physical plasma and its antimicrobial effect against Pseudomonas aeruginosa and Staphylococcus aureus. *GMS Krankenhaushygiene Interdisziplinär*, 7(1):1–7, 2012.

[43] G. Daeschlein, T. von Woedtke, E. Kindel, R. Brandenburg, K-D. Weltmann, and M. Jünger. Antibacterial Activity of an Atmospheric Pressure Plasma Jet Against Relevant Wound Pathogens in vitro on a Simulated Wound Environment. *Plasma Processes and Polymers*, 7(3-4):224–230, March 2010.

[44] M. Laroussi, I. Alexeff, and W. L. Kang. Biological Decontamination by Nonthermal Plasmas. *IEEE TRANSACTIONS ON PLASMA SCIENCE*, 28(1):184–188, 2000.

[45] N. Abramzon, J.C. Joaquin, J. Bray, and G. Brelles-mari no. Biofilm Destruction by RF High-Pressure Cold Plasma Jet. *IEEE Transactions on plasma science*, 34(4):1304–1309, 2006.

[46] K-Y. Lee, B. Joo Park, D. Hee Lee, I-S. Lee, S. O. Hyun, K-H. Chung, and J-C. Park. Sterilization of Escherichia coli and MRSA using microwave-induced argon plasma at atmospheric pressure. *Surface and Coatings Technology*, 193(1-3):35–38, April 2005.

[47] J J Cotter, P Maguire, F Soberon, S Daniels, J P O'Gara, and E Casey. Disinfection of meticillin-resistant Staphylococcus aureus and Staphylococcus epidermidis biofilms using a remote non-thermal gas plasma. *The Journal of hospital infection*, 78(3):204–7, July 2011.

[48] R. S. Tipa and G. M. W. Kroesen. Plasma-Stimulated Wound Healing. *IEEE Transactions on Plasma Science*, 39(11):2978–2979, November 2011.

[49] S Hofmann, A F H van Gessel, T Verreycken, and P Bruggeman. Power dissipation, gas temperatures and electron densities of cold atmospheric pressure helium and argon RF plasma jets. *Plasma Sources Science and Technology*, 20(6):065010, December 2011.

[50] A Fantom. *Radio frequency & microwave power measurement*. The Institution of Engineering and Technology, 1990.

[51] P. Bruggeman, D. C. Schram, M. G. Kong, and C. Leys. Is the Rotational Temperature of OH(A-X) for Discharges in and in Contact with Liquids a Good Diagnostic for Determining the Gas Temperature? *Plasma Processes and Polymers*, 6(11):751–762, November 2009.

[52] P. Bruggeman, F. Iza, P. Guns, D. Lauwers, M.G. Kong, Y.A. Aranda-Gonzalvo, C. Leys, and D. C. Schram. Electronic quenching of OH(A) by water in atmospheric pressure plasmas and its influence on the gas temperature determination by OH(A-X) emission. *Plasma Sources Science and Technology*, 19(1):015016, February 2010.

[53] K. Downard. *Mass Spectrometry - A Foundation Course*. Royal Society of Chemistry, 2004.

[54] E. de Hoffmann and V. Stroobant. *Mass spectrometry - Principles and Applications*. Wiley-Interscience, 2001.

[55] M. Mathieu. Mémoire sur Le Mouvement Vibratoire dune Membrane de forme Elliptique. *Journal de Mathématiques Pures et Appliquées*, pages 137–203, 1868.

[56] M. Barber, D.B. Gordon, and M.D. Woods. Theoretical Studies of Ion Trajectories in Quadrupole Systems. *Rapid communications in mass spectrometry*, 4(10):442–446, 1990.

[57] D. R. Miller. Free Jet Sources. In Giacinto Scoles, David Bassi, Udo Buck, and Laine D.C., editors, *Atomic and Molecular Beam Methods: Volume 1*, pages 14–53. 1988.

[58] J. Weiss. *Handbook of Ion Chromatography*. Wiley-VCH, 2004.

[59] R. F. Pupo Nogueira, M. C. Oliveira, and W. C. Paterlini. Simple and fast spectrophotometric determination of H(2)O(2) in photo-Fenton reactions using metavanadate. *Talanta*, 66(1):86–91, March 2005.

[60] P R Twentyman and M Luscombe. A study of some variables in a tetrazolium dye (MTT) based assay for cell growth and chemosensitivity. *British journal of cancer*, 56(3):279–85, September 1987.

[61] T F Slater, B Sawyer, and U Strauli. Studies on succinate-tetrazolium reductase systems III. Points of coupling of four different tetrazolium salts. *Biochim. Biophys. Acta*, 77:383–393, 1963.

[62] A. Yanguas-Gil, K. Focke, J. Benedikt, and A. von Keudell. Optical and electrical characterization of an atmospheric pressure microplasma jet for ArCH4 and ArC2H2 mixtures. *Journal of Applied Physics*, 101(10):103307, 2007.

[63] J. Benedikt, S. Hofmann, N. Knake, H. Böttner, R. Reuter, a. von Keudell, and V. Schulz-von der Gathen. Phase resolved optical emission spectroscopy of coaxial microplasma jet operated with He and Ar. *The European Physical Journal D*, 60(3):539–546, September 2010.

[64] K. Focke. *Reaktionschemie in einem Mikroplasmajet, Master's thesis.* Ruhr-Universität Bochum, 2007.

[65] F. Kannari, A. Suda, M. Obara, and T. Fujioka. Theoretical Simulation of Electron-Beam-Excited Xenon-Chloride (XeCl) Lasers. *IEEE Journal of Quantum Electronics*, 19(10):1587–1600, 1983.

[66] R. Derai, S. Fenistein, M. Gerard-Ain, T.R. Govers, R. Marx, G. Mauclaire, C.Z. Profous, and C. Sourisseau. Thermal-energy charge transfer of Ar+ with H2O: Internal and kinetic energy of the product H2O+. *Chemical Physics*, 44:65–71, 1979.

[67] I.A. Kossyi, A. Yu Kostinsky, A.A. Matveyev, and V.P. Silakov. Kinetic scheme of the non-equilibrium discharge in nitrogen-oxygen mixtures. *Plasma Sources Science and Technology*, 1:207–220, 1992.

[68] R. Dorai and M J Kushner. Repetitively pulsed plasma remediation of NO x in soot laden exhaust using dielectric barrier discharges. *Journal of Physics D: Applied Physics*, 35(22):2954–2968, November 2002.

[69] P. Bruggeman, F. Iza, D. Lauwers, and Y. A. Gonzalvo. Mass spectrometry study of positive and negative ions in a capacitively coupled atmospheric pressure RF excited glow discharge in Hewater mixtures. *Journal of Physics D: Applied Physics*, 43(1):012003, January 2010.

[70] A N Hayhurst and Kittelson D B. The Positive and Negative Ions in Oxy-acetylene Flames. *Combustion and Flame*, 31:37–51, 1978.

[71] P. Bruggeman, G. Cunge, and N. Sadeghi. Absolute OH density measurements by broadband UV absorption in diffuse atmospheric-pressure HeH 2 O RF glow discharges. *Plasma Sources Science and Technology*, 21(3):035019, June 2012.

[72] A M Kropinski, V Lewis, and D Berry. Effect of growth temperature on the lipids, outer membrane proteins, and lipopolysaccharides of Pseudomonas aeruginosa PAO. *Journal of bacteriology*, 169(5):1960–6, May 1987.

[73] A. Tsuji, Y. Kaneko, K. Takahashi, M. Ogawa, and S. Goto. The effects of temperature and pH on the growth of eight enteric and nine glucose non-fermenting species of gram-negative rods. *Microbiol. Immunol.*, 26:15–24, 1982.

[74] R. R. Netz. Water and ions at interfaces. *Current Opinion in Colloid & Interface Science*, 9(1-2):192–197, August 2004.

[75] H Hülsheger, J Potel, and E G Niemann. Electric field effects on bacteria and yeast cells. *Radiation and environmental biophysics*, 22(2):149–62, January 1983.

[76] V. Di Noto and M. Mecozzi. Determination of Seawater Salinity by Ultraviolet Spectroscopic Measurements. *Applied Spectroscopy*, 51(9):1294–1302, 1997.

[77] R. Brandenburg, H. Lange, T. Von Woedtke, M. Stieber, E. Kindel, J. Ehlbeck, and K-d. Weltmann. Antimicrobial Effects of UV and VUV Radiation of Nonthermal Plasma Jets. *IEEE Transactions on plasma science*, 37(6):877–883, 2009.

[78] T. von Woedtke, H. Lange, and K-D Weltmann. Antimicrobial activity of plasma-generated VUV radiation and its complete absorption by thin liquid layers. *ICOPS*, 2012.

[79] R.L. Abshire and H. Dunton. Resistance of Selected Strains of Pseudomonas aeruginosa to Low-Intensity Ultraviolet Radiation. *Applied and environmental microbiology*, 41(6):1419–1423, 1981.

[80] W Sontag and K F Weigezahn. Absorption of DNA in the region of vacuum-uv (3-25 eV). *Radiation and environmental biophysics*, 12(3):169–74, October 1975.

[81] R.O. Fernández and R.A. Pizarro. Pseudomonas aeruginosa UV-A-induced lethal effect : influence of salts , nutritional stress and pyocyanine. *J. Photochem. and Photobiol. B: Biol.*, 50:59–65, 1999.

[82] I.A. Soloshenko, V.Y. Bazhenov, V.a. Khomich, V.V. Tsiolko, and N.G. Potapchenko. Comparative Research of Efficiency of Water Decontamination by UV Radiation of Cold Hollow Cathode Discharge Plasma Versus That of Low- and Medium-Pressure Mercury Lamps. *IEEE Transactions on Plasma Science*, 34(4):1365–1369, August 2006.

[83] ICNIRP. *ICNIRP Guidelines on limits of exposure to ultraviolet radiation of wavelength between 100 nm and 400 nm.* 2004.

[84] NDRL/NIST. Solution Kinetics Database kinetics.nist.gov/solution/.

[85] M Roeselová, J Vieceli, L X Dang, B C Garrett, and D J Tobias. Hydroxyl radical at the air-water interface. *Journal of the American Chemical Society*, 126(50):16308–9, December 2004.

[86] J Vieceli, M Roeselova, N Potter, L X Dang, B C Garrett, and D J Tobias. Molecular dynamics simulations of atmospheric oxidants at the air-water interface: solvation and accommodation of OH and O3. *The journal of physical chemistry. B*, 109(33):15876–92, August 2005.

[87] R. Vacha, P. Slavicek, M. Mucha, J. Finlayson-Pitts, and P. Jungwirth. Adsorption of Atmospherically Relevant Gases at the Air / Water Interface : Free Energy Profiles of Aqueous Solvation of N2, O2, O3, OH, H2O, HO2 and H2O2. *J. Phys. Chem. A*, 108(52):11573–11579, 2004.

[88] S Reuter, J Winter, S Iseni, S Peters, a Schmidt-Bleker, M Dünnbier, J Schäfer, R Foest, and K-D Weltmann. Detection of ozone in a MHz argon plasma bullet jet. *Plasma Sources Science and Technology*, 21(3):034015, June 2012.

[89] A V Pipa, T Bindemann, R Foest, E Kindel, J Röpcke, and K-D Weltmann. Absolute production rate measurements of nitric oxide by an atmospheric pressure plasma jet (APPJ). *Journal of Physics D: Applied Physics*, 41(19):194011, October 2008.

[90] R. Mensink. *OH production in a cold atmospheric pressure plasma jet in the context of tooth whitening, Master's thesis.* Eindhoven University of Technology, 2012.

[91] L Zhu, C Gunn, and J S Beckman. Bactericidal activity of peroxynitrite. *Archives of biochemistry and biophysics*, 298(2):452–7, November 1992.

[92] S J Klebanoff. Reactive nitrogen intermediates and antimicrobial activity: role of nitrite. *Free radical biology & medicine*, 14(4):351–60, April 1993.

[93] O V Gerasimov and S V Lymar. The Yield of Hydroxyl Radical from the Decomposition of Peroxynitrous Acid. *Inorg. Chem*, 38:4317–4321, 1999.

[94] J. W. Coddington, J. K. Hurst, and S. V. Lymar. Hydroxyl Radical Formation during Peroxynitrous Acid Decomposition. *J. Am. Chem. Soc*, 121:2438–2443, 1999.

[95] S. L. Kohnen, A. A. Mouithys-Mickalad, G. P. Deby-Dupont, C. M.T. Deby, P. Hans, M. L. Lamy, and A. F. Noels. Investigation of the reaction of peroxynitrite with propofol at acid pH: Predominant production of oxidized, nitrated, and halogenated derivatives. *Nitric Oxide*, 8(3):170–181, May 2003.

[96] G Merényi, J Lind, G Czapski, and S Goldstein. The decomposition of peroxynitrite does not yield nitroxyl anion and singlet oxygen. *Proceedings of the National Academy of Sciences of the United States of America*, 97(15):8216–8, July 2000.

[97] J S Beckman and W H Koppenol. Nitric oxide, superoxide, and peroxynitrite: the good, the bad, and ugly. *The American journal of physiology*, 271(5 Pt 1):C1424–37, November 1996.

[98] B Alvarez and R Radi. Peroxynitrite reactivity with amino acids and proteins. *Amino acids*, 25(3-4):295–311, December 2003.

[99] E. Halfpenny and P.L. Robinson. Pernitrous acid.The Reaction between Hydrogen Peroxide and Nitrous Acid, and the Properties of an Intermediate Product. *Journal of the Chemical Society*, pages 928–938, 1952.

[100] L. R. Mahoney. Evidence for the Formation of Hydroxyl Radicals in the Isomerization of Pernitrous Acid to Nitric Acid in Aqueous Solution. *Journal of the*, 92(17):5262–5263, 1970.

[101] J-Y. Park and Y-n. Lee. Solubility and decomposition kinetics of nitrous acid in aqueous solution. *J. Phys. Chem*, 92:6294–6302, 1988.

[102] J Xu, X Xu, and W Verstraete. The bactericidal effect and chemical reactions of acidified nitrite under conditions simulating the stomach. *The Society for Applied Microbiology*, 90:523–529, 2001.

[103] B. Pietersen, V.S. Brozel, and T.E. Cloete. Response of Pseudomonas aeruginosa PAO following exposure to hydrogen peroxide. *Water SA*, 22(3):239–244, 1996.

[104] G K Nyberg and J Carlsson. Metabolic Inhibition of Peptostreptococcus anaerobius Decreases the Bactericidal Effect of Hydrogen Peroxide. *Antimicrobial agents and chemotherapy*, 20(6):726–730, 1981.

[105] M.A. Khadre, A.E. Yousef, and Kom J.-G. Microbiological Aspects of Ozone Applications in Food : A Review. *Journal of food science*, 66(9):1242–1252, 2001.

[106] R. Battino, T.R. Rettich, and T. Tominaga. The Solubility of Oxygen and Ozone in Liquids. *J. Phys. Chem. Ref. Data*, 12(2):163–178, 1983.

[107] S. Ikawa, K. Kitano, and S. Hamaguchi. Effects of pH on Bacterial Inactivation in Aqueous Solutions due to Low-Temperature Atmospheric Pressure Plasma Application. *Plasma Processes and Polymers*, 7(1):33–42, January 2010.

[108] A.Y. Kim and D.W. Thayer. Radiation-induced cell lethality of Salmonella typhimurium ATCC 14028: Cooperative effect of hydroxyl radical and oxygen. *Radiat. Res.*, 144:36–42, 1995.

[109] A. Tani, Y. Ono, S. Fukui, S. Ikawa, and K. Kitano. Free radicals induced in aqueous solution by non-contact atmospheric-pressure cold plasma. *Applied Physics Letters*, 100(25):254103, 2012.

[110] J J van Hemmen and W J A Meuling. Inactivation of Escherichia coli by Superoxide Dismutation Products and Their Dismutation Products. *Archives of biochemistry and biophysics*, 182:743–748, 1977.

[111] E. D. Kellogg and I. Fridovich. Superoxide, Hydrogen Peroxide, and Singlet Oxygen in Lipid Peroxidation by a Xanthine Oxidase System. *The Journal of Biological Chemistry*, 250(22):8812–8817, 1975.

[112] H.P. Misra and I. Fridovich. Superoxide Dismutase and the Oxygen Enhancement of Radiation Lethality. *Archives of biochemistry and biophysics*, 176:577–581, 1976.

[113] S. S. Korshunov and J. A. Imlay. A potential role for periplasmic superoxide dismutase in blocking the penetration of external superoxide into the cytosol of Gram-negative bacteria. *Molecular Microbiology*, 43:95–106, 2002.

[114] M. Tecder-Unal, F. Can, M. Demirbilek, G. Karabay, H. Tufan, and H. Arslan. The bactericidal and morphological effects of peroxynitrite on Helicobacter pylori. *Helicobacter*, 13(1):42–8, February 2008.

[115] C D Pericone, K Overweg, W M Peter, J N Weiser, P W M Hermans, and J N Weister. Inhibitory and Bactericidal Effects of Hydrogen Peroxide Production by Streptococcus pneumoniae on Other Inhabitants of the Upper Respiratory Tract Inhibitory and Bactericidal Effects of Hydrogen Peroxide Production by Streptococcus pneumoniae on Other In. *Infection and Immunity*, 68(7):3990–3997, 2000.

[116] S Burgassi, I Zanardi, V Travagli, E Montomoli, and V Bocci. How much ozone bactericidal activity is compromised by plasma components? *Journal of applied microbiology*, 106(5):1715–21, May 2009.

[117] P G Mazzola, A F Jozala, L C D L Novaes, P Moriel, and T C Penna. Minimal inhibitory concentration (MIC) determination of disinfectant and/or sterilizing agents. *Brazilian Journal of Pharmaceutical Sciences*, 45(2):241–248, June 2009.

[118] G. DeQueiroz. *A new broad spectrum disinfectant suitable for the food industry.* PhD thesis, Louisiana State University, 2004.

[119] M G Baldry. The bactericidal, fungicidal and sporicidal properties of hydrogen peroxide and peracetic acid. *The Journal of applied bacteriology*, 54(3):417–23, June 1983.

[120] S. Farooq and S. Akhlaque. Comparative response of mixed cultures of bacteria and virus to ozonation. *Water Research*, 17(7):809–812, 1983.

[121] F. Zuma, J. Lin, and S. B. Jonnalagadda. Kinetics of inactivation of Pseudomonas aeruginosa in aqueous solutions by ozone aeration. *Journal of Environmental Science and Health, Part A*, 44(10):929–935, August 2009.

[122] J.-G. Kim and A.E. Yousef. Inactivation Kinetics of Foodborne Spoilage and Pathogenic Bacteria by Ozone. *Journal of food science*, 65(3):521–528, 2000.

[123] I Lezcano, R P Rey, Ch Baluja, and E Sánchez. Ozone Inactivation of Pseudomonas aeruginosa , Escherichia coli , Shigella sonnei and Salmonella typhimurium in Water. *Ozone science and Engineering1*, 21:292–300, 1999.

[124] H Ikai, K Nakamura, M Shirato, T Kanno, A Iwasawa, K Sasaki, Y Niwano, and M Kohno. Photolysis of hydrogen peroxide, an effective disinfection system via hydroxyl radical formation. *Antimicrobial agents and chemotherapy*, 54(12):5086–91, December 2010.

[125] C Miller, B McMullin, A Ghaffari, A Stenzler, N Pick, D Roscoe, A Ghahary, J Road, and Y Av-Gay. Gaseous nitric oxide bactericidal activity retained during intermittent high-dose short duration exposure. *Nitric oxide : biology and chemistry / official journal of the Nitric Oxide Society*, 20(1):16–23, February 2009.

[126] K E Webert, J Vanderzwan, M Duggan, J A Scott, D G Mccormack, J F Lewis, and S Mehta. Effects of inhaled nitric oxide in a rat model of Pseudomonas aeruginosa pneumonia. *Crit Care Med*, 28(7):2397–2405, 2000.

[127] J P Eiserich, C E Cross, A D Jones, B Halliwell, and A Van Der Vliet. Formation of Nitrating and Chlorinating Species by Reaction of Nitrite with Hypochlorous Acid. *The Journal of Biological Chemistry*, 271(32):19199–19208, 1996.

[128] M. LeChevallier and A. U. Kwok-Keung. Inactivation (disinfection) processes. In L. Fewtrell and J. Bartram, editors, *Water Treatment and Pathogen Control: Process Efficiency in Achieving Safe Drinking Water*, pages 41–65. IWA Publishing, London, UK, 2004.

[129] J. Kim, B. Pitts, P. S Stewart, A. Camper, and J. Yoon. Comparison of the antimicrobial effects of chlorine, silver ion, and tobramycin on biofilm. *Antimicrobial agents and chemotherapy*, 52(4):1446–53, April 2008.

[130] G Ellison, J V Straumfjord, and J P Hummel. Buffer capacities of human blood and plasma. *Clinical chemistry*, 4(6):452–61, December 1958.

[131] J McNamara and L I Worthley. Acid-base balance: part I. Physiology. *Critical care and resuscitation : journal of the Australasian Academy of Critical Care Medicine*, 3(3):181–7, September 2001.

[132] J McNamara and L I Worthley. Acid-base balance: part II. Pathophysiology. *Critical care and resuscitation : journal of the Australasian Academy of Critical Care Medicine*, 3(3):188–201, September 2001.

[133] Arthur C. Guyton and John E. Hall. Regulation of Acid-Base Balance. In *Textbook of Medical Physiology*, chapter 30, pages 383–401. Saunders, 11th edition, 2005.

[134] M. Naïtali, G. Kamgang-Youbi, J-M. Herry, M-N. Bellon-Fontaine, and J-L. Brisset. Combined effects of long-living chemical species during microbial inactivation using atmospheric plasma-treated water. *Applied and environmental microbiology*, 76(22):7662–4, November 2010.

[135] K. Oehmigen, M. Hähnel, R. Brandenburg, Ch. Wilke, K.-D. Weltmann, and Th. von Woedtke. The Role of Acidification for Antimicrobial Activity of Atmospheric Pressure Plasma in Liquids. *Plasma Processes and Polymers*, 7(3-4):250–257, March 2010.

[136] M J Traylor, M J Pavlovich, S Karim, P Hait, Y Sakiyama, D S Clark, and D B Graves. Long-term antibacterial efficacy of air plasma-activated water. *Journal of Physics D: Applied Physics*, 44(47):472001, November 2011.

Appendix A

ICNIRP weighted UV-flux measurements

This appendix shows the irradiances of the various conditions as shown in section 5.3 corrected using the ICNIRP guidelines for UV exposure discussed in section 7.5.

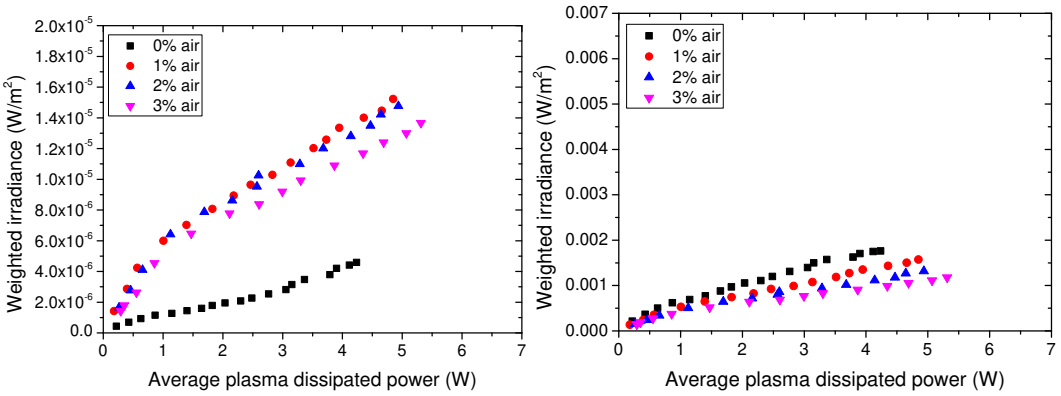

(a) UVA

(b) UVB

(c) UVC (200-280nm)

Figure A.1: Weighted UVA, UVB and UVC irradiance as a function of average plasma dissipated power for various percentages of added air for 1.5slm argon using the ring electrode at a 20% duty cycle.

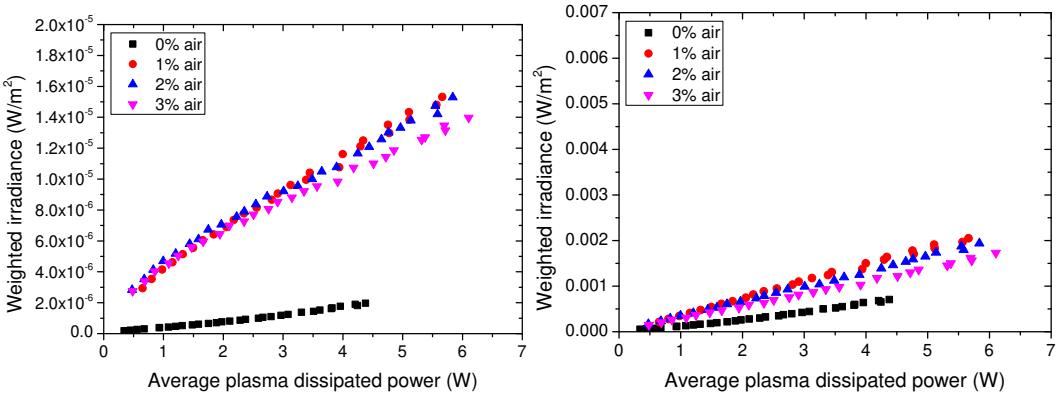

(a) UVA

(b) UVB

(c) UVC (200-280nm)

Figure A.2: Weighted UVA, UVB and UVC irradiance as a function of average plasma dissipated power for various percentages of added air for 1.5slm helium using the ring electrode at a 20% duty cycle.

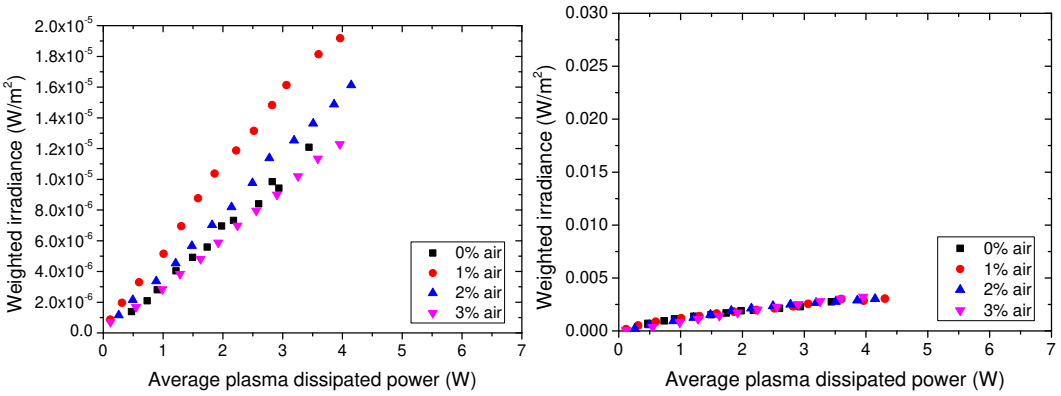

(a) UVA

(b) UVB

(c) UVC (200-280nm)

Figure A.3: Weighted UVA, UVB and UVC irradiance as a function of average plasma dissipated power for various percentages of added air for 1.5slm argon using the plate electrode at a 100% duty cycle.

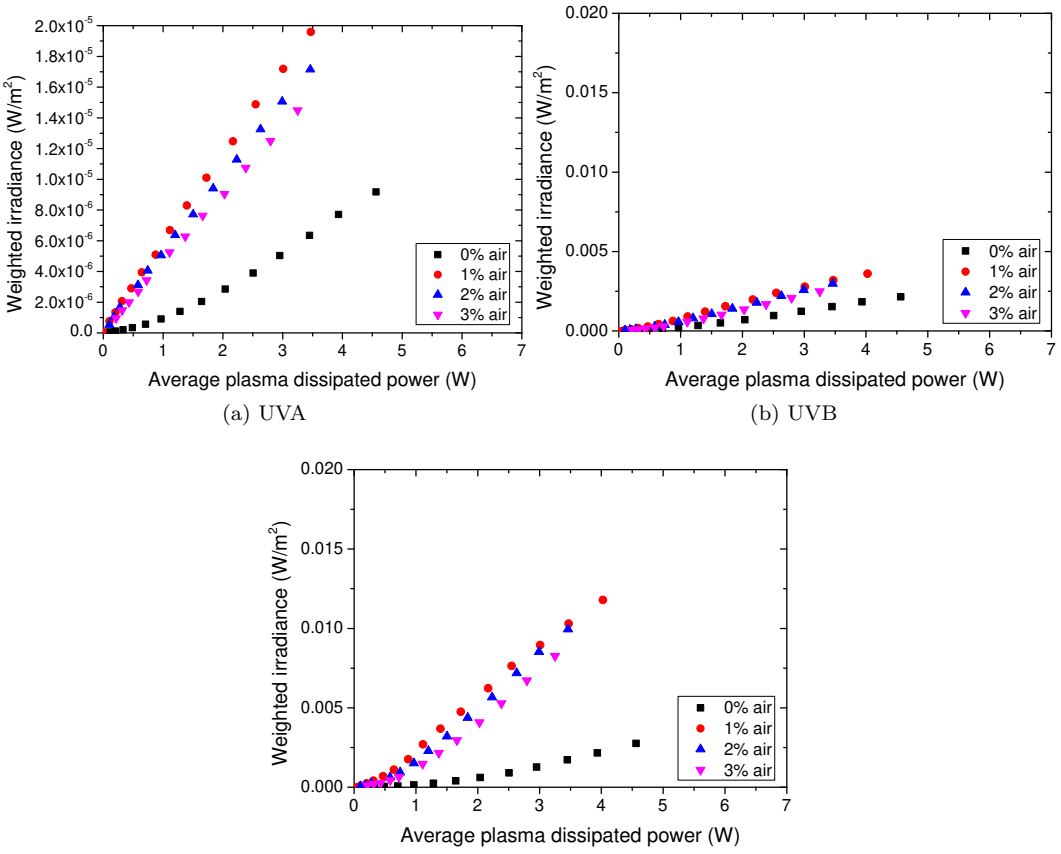

(a) UVA

(b) UVB

(c) UVC (200-280nm)

Figure A.4: Weighted UVA, UVB and UVC irradiance as a function of average plasma dissipated power for various percentages of added air for 1.5slm helium using the plate electrode at a 100% duty cycle.